Davide Ricci

Direct imaging, photometry and spectroscopy of gravitationally lensed quasars

PhD Thesis in Sciences
Department of Astrophysics, Geophysics and Oceanography - Faculty of Sciences
University of Liège, Belgium
February 10, 2012

Supervisors: Prof. Jean Surdej, Dr. Hervé Le Coroller
Jury: Prof. Serge Habraken (president), Dr. Jean Manfroid, Prof. Maarten Baes, Prof. Philippe Bendjoya, Dr. Martin Dominik

Davide Ricci
AGO – Astrophysics, Geophysics and Oceanography Department
AEOS-EASO – Extragalactic Astrophysics and Space Observations team
ULG – University of Liège

E-mail:
ricci@astro.ulg.ac.be

Support:
This research was supported by a fellowship from FRIA (Fonds pour la Recherche dans l'Industrie et l'Agriculture) and ARC (Action de Recherche Concertée) – Communauté Française de Belgique – Académie Wallonie-Europe. Several stages for a total of six months were effectuated at the OHP (Observatoire de Haute Provence), France.

Technical informations:
This work was typeset with LaTeX using the ArsClassica package. The package was modified to use the Ubuntu Font Family as serif font for titles and labels. The figures were composed with Inkscape, a free software vector graphics editor licensed under the GNU General Public License. The graphics were generated with the open source software gnuplot. The RGB colors used were #888888 for gray, #fb8b00 for orange, #990066 for purple and #6699cc for light blue.

The titlepage reproduces the quadruply imaged quasar HE0435–1223 composed by Andrii Elyiv after superposing the best seeing frames observed in the i filter with the 1.54m Danish telescope (ESO–La Silla Observatory).

Contents

List of Figures

List of Tables

Abstract

The content of the present PhD thesis entitled *"Direct imaging, photometry and spectroscopy of gravitationally lensed quasars"* is divided in two parts: a first part relative to new instrumental concepts for future observational studies of gravitationally lensed quasars, and an observational part concerning the results obtained on some of these particularly remarkable objects using existing facilities.

Concerning the first part, we present a way to optically simulate gravitational lens effects using a particular kind of optical lenses. Gravitational lens effects are due to the presence of a massive object which deforms space in accordance with General Relativity. If a distant observer is located very close to the line joining the background source (cf. a quasar) and the intervening massive object (cf. a lensing galaxy), the former may be able to see multiple images of the background source. As we will show, particular optical lenses can reproduce this effect. Such optical instruments can be used either to simulate in laboratory gravitational lens effects, or to invert and correct observed lensed images in order to restore the image of the real background source.

We derive the shapes of refractive and reflective surfaces corresponding to different lens models, and the shapes corresponding to an external shear. We suggest to design an instrument involving such optical surfaces. This instrument could be specifically designed for particular gravitational lens systems for which we know the mass distribution of the deflector. Other designs could involve adaptive optics devices which dynamically adapt their shape to provide the inversion of the gravitational lens effects.

Pairing this instrument with a coronagraph, it is possible to mask the central part of the light of the background quasar and enhance its faint surrounding (cf. host galaxy, faint companions, ...).

To reach this goal, we propose a new concept of coronagraphic device with an adaptive hologram. The performances of this innovative device are studied by means of a large number of numerical simulations, and we quantify the improvement of this concept with respect to the traditional methods also in the framework of a practical implementation.

The second part of this thesis is focused on telescope observations of remarkable gravitationally lensed quasars. We carried on photometric multi-band telescope observations over several epochs of the multiply imaged quasars HE0435–1223 and UM673, and we studied their color and flux variations.

HE0435–1223 is a quadruply imaged quasar formed by an intervening elliptical galaxy. Our monitoring, carried on over two years, put in evidence a significant flux decrease and a significant reddening of all the four lensed components, and we attribute such changes to an intrinsic variation of the quasar. Moreover, the brightest component is probably also affected by microlensing.

We observed the doubly imaged quasar UM673 during four years, and our data reduction shows, as for the case of HE0435–1223, interesting results in terms of flux and color variations.

Then, in the framework of spectroscopic observations of the gravitationally lensed quasar RXJ1131-1231, we present an original and new data reduction technique that we adopted to face the peculiar spectra produced by a bent slit, built to include in a single image several lensed components. Finally, we show the first preliminary results of this gravitational lens system obtained in the light of the [OIII] emission line region.

Résumé

Le contenu de cette thèse de doctorat intitulée *"Imagerie directe, photométrie et spectroscopie de quasars sujets à des effets de lentille gravitationnelle"* est composé d'une partie consacrée au développement de nouveaux instruments pour de futures observations de quasars sujets à des effets de lentille gravitationnelle, et en une seconde partie observationnelle relative aux résultats obtenus pour plusieurs de ces objets au moyen d'infrastructures existantes.

Dans la première partie nous présentons une technique optique pour simuler (avec une lentille ou un miroir) des effets de lentille gravitationnelle. De tels effets sont dus à la présence d'un objet massif, dont la masse déforme l'espace en accord avec la Relativité Générale. Si un observateur distant est situé très près de la ligne liant la source d'arrière plan (par exemple un quasar) et l'objet massif interposé (par exemple une galaxie déflectrice), l'observateur peut être capable de voir des images multiples de la source d'arrière plan. Notre dispositif optique peut être utilisé soit pour simuler au laboratoire ces effets, soit pour les inverser et pour corriger les images observées sujettes à des effets de la lentille afin de restituer l'image de la vraie source d'arrière plan.

Nous déterminons les formes des surfaces réfractives et réfléchissantes correspondant à différents modèles de lentille, et la forme correspondante aux effets de distorsion due à un champ gravitationnel extérieur, qu'on appelle aussi cisaillement extérieur. Nous suggérons de développer un instrument basé sur ces surfaces optiques.

L'instrument peut être spécifiquement conçu pour des systèmes de lentilles gravitationnelles dont la distribution de masse du déflecteur est connue. D'autres solutions peuvent impliquer l'adoption de systèmes d'optique adaptative qui adaptent dynamiquement leur forme pour corriger les effets de lentille gravitationnelle.

En couplant ce dispositif avec un coronographe, il est possible de masquer la partie centrale de la lumière du quasar d'arrière plan et de mettre en évidence son environement peu lumineux (galaxie hôte, compagnons, . . .).

Pour atteindre ce but, nous proposons un nouveau concept de coronographe avec hologramme adaptatif. Les performances de cet instrument innovant sont étudiées au moyen d'un grand

nombre de simulations numériques.

La deuxième partie de la thèse se focalise sur des observations obtenues au moyen de divers télescopes pour certains quasars brillants sujets à des effets de lentille gravitationnelle. Nous avons mené personnellement les observations photométriques, dans plusieurs bandes passantes et à plusieurs époques, des quasars multiples HE0435–1223 et UM673, et nous étudions leurs variations en flux et en couleur.

HE0435–1223 est un quasar quadruple produit par une galaxie elliptique. Nos observations conduites pendant une période de 2 ans ont permis de mettre en évidence une diminution significative du flux et aussi un rougissement de chacune des quatre composantes du mirage gravitationnel. Nous attribuons ces changements à des variations intrinsèques du quasar. En plus, la composante la plus brillante est probablement affectée par un effet microlentille.

Nous avons observé le quasar double UM673 pendant quatre ans, et notre réduction et analyse des données montrent, de la même manière que pour le cas de HE0435–1223, des résultats intéressants en termes de variations de flux et de couleur.

Finalement, dans le cadre des observations spectroscopiques du quasar sujet aux effets de lentille gravitationnelle RXJ1131-1231, nous présentons une technique innovante de réduction des données que nous avons développée pour extraire les spectres formés par une fente courbée, permettant d'inclure trois des quatre composantes du mirage gravitationnel. Ensuite, nous montrons les premiers résultats concernant l'étude de la région émettant les raies de [OIII].

Sommario

Il contenuto della presente tesi di dottorato intitolata *"Immagine diretta, fotometria e spettroscopia di quasar soggetti all'effetto lente gravitazionale"* è diviso in una parte relativa allo sviluppo di nuovi strumenti per i futuri studi osservativi dei quasar soggetti all'effetto lente gravitazionale, ed una parte osservativa relativa ai risultati ottenuti su diversi oggetti di questo tipo, utilizzando le infrastrutture esistenti.

Nella prima parte viene presentata una tecnica per simulare l'effetto lente gravitazionale dovuto alla presenza di un oggetto massiccio, la cui massa deforma lo spazio in accordo con la teoria della Relatività Generale. Se un osservatore lontano è posizionato nei pressi della linea che congiunge una sorgente luminosa sullo sfondo (ad esempio un quasar) ed un oggetto massiccio intermedio (una galassia deflettrice), l'osservatore è in grado di osservare immagini multiple della sorgente sullo sfondo. Tale dispositivo ottico può essere usato sia per simulare questo effetto in laboratorio, sia per invertire e correggere le immagini osservate soggette all'effetto lente, così da restituire la vera immagine della sorgente sullo sfondo.

Vengono ricavate le forme delle superfici rifrangenti e riflettenti corrispondenti a diversi modelli di lente, e la forma corrispondente alla distorsione indotta da un campo gravitazionale esterno (effetto che viene chiamato *external shear* in inglese e *cisaillement extérieur* in francese). Viene suggerito di realizzare uno strumento che coinvolga queste superfici ottiche. Tale strumento può essere specificatamente sviluppato per particolari sistemi di lente gravitazionale per i quali è conosciuta la distribuzione di massa del deflettore; altre soluzioni includono sistemi di ottica adattiva che modificano dinamicamente la loro forma per correggere l'effetto lente gravitazionale.

Accoppiando questo oggetto con un coronografo, è possibile mascherare la parte centrale della luce del quasar sullo sfondo, mettendo in evidenza i deboli e vicini dintorni (galassia ospite, galassie satelliti, ...), che sarebbero altrimenti invisibili per via del contrasto con la sorgente luminosa centrale.

Per raggiungere questo risultato, viene proposto un nuovo tipo di coronografo con ologramma adattivo.

Le prestazioni di questo strumento innovativo sono studiate per mezzo di un gran numero di simulazioni numeriche, e ven-

gono quantificati i miglioramenti rispetto ai dispositivi coronografici tradizionali.

La seconda parte della tesi si focalizza su osservazioni ottenute per mezzo di diversi telescopi per certi quasar brillanti soggetti all'effetto lente gravitazionale. Per diversi anni sono state realizzate osservazioni fotometriche dei quasar multipli HE0435–1223 ed UM673 con diversi filtri ottici, e sono state studiate le variazioni in flusso ed indice di colore.

HE0435–1223 è un esempio di quasar quadruplo deflesso da una galassia ellittica. Le nostre osservazioni, condotte per un periodo di due anni, hanno permesso di mettere in evidenza una diminuzione significativa del flusso così come un arrossamento di ognuna delle quattro le componenti del miraggio gravitazionale. Questi cambiamenti vengono attribuiti a delle variazioni intrinseche del quasar. Inoltre, la componente più brillante è probabilmente affetta da un effetto di microlente gravitazionale.

Il quasar doppio UM673 è stato invece osservato per quattro anni consecutivi, e la nostra riduzione e l'analisi dei dati mostrano, come per il caso di HE0435–1223, dei risultati interessanti in termini di variazioni in flusso ed indice di colore.

Infine, nell'ambito delle osservazioni spettroscopiche del quasar multiplo RXJ1131-1231, vengono presentati in primo luogo la tecnica innovativa di riduzione delle immagini, sviluppata per estrarre gli spettri formati da una fenditura curva che permette di includere contemporaneamente tre delle quattro componenti del miraggio gravitazionale; in seguito vengono mostrati i risultati relativi allo studio della regione delle righe in emissione di [OIII].

1 Introduction

Gravitationally lensed quasars are among the most spectacular objects that can be imaged with a telescope, and their study is of great interest in astrophysics and cosmology.

In this work, we present an overview of observational studies of selected multiply imaged quasars. In Chap. 2 we describe the theoretical shape, for different lens models, of refracting and reflecting optical surfaces capable to reproduce and eventually invert gravitational lensing effects, suggesting to design an instrument capable to restitute in real time the unlensed image of the real source, and we suggest to pair this instrument with a coronagraphic device in order to block the bright central source and explore the close faint features of the unlensed quasar.

Then, in Chap. 3, we propose as a coronagraph a new instrument based on the introduction of an adaptive hologram in the optical scheme, and we show that it is theoretically possible, thanks to this design, to improve the nulling power of the similarly available devices. Numerical simulations to validate this concept are successfully carried out in Chap. 4, under different conditions to prove the validity limits.

Observations of multiply imaged quasars are presented in Chap. 5, where are treated in detail the equipment and the photometric data reduction strategy. The objects, observed in different optical spectral bands during multiple epochs, are treated in detail in Chap. 6 for the quadruply imaged quasar HE0435−1223, and in Chap. 7 for the gravitationally lensed quasar UM673. In those chapters, observational results concerning flux and color variations are presented. In Chap. 8 we show preliminary results concerning the spectroscopic observations of the gravitationally lensed quasar RXJ1131-1231, obtained by means of an innovative observing technique and data reduction software. Finally, we resume the conclusions and propose future perspectives in Chap. 9.

In the following sections, a brief introduction of quasars and AGN, optical inversion techniques, coronagraphy, and observations is given.

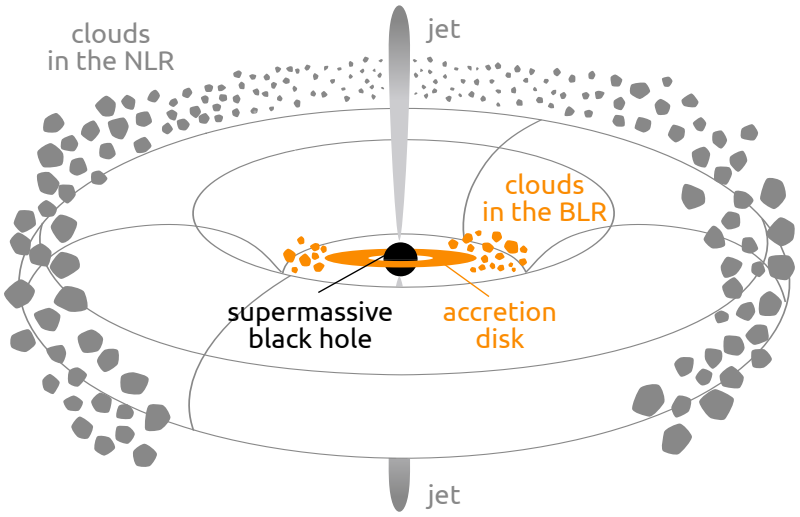

Figure 1: Schematic image representing the central region of an AGN.

1.1 The Unified Model of AGN

The discovery of the first quasars (quasi-stellar radio sources), and of QSOs (Quasi Stellar Objects) in general, took place in the 1960s. Since that date, astronomers have struggled to introduce some sort of order into the zoo of objects known as AGN (Active Galactic Nuclei).

AGN are very luminous compact objects located at the center of certain galaxies, called Active Galaxies due to that reason.

Supermassive black holes at the center of these galaxies are believed to be the cause of this excess of radiation via accretion (as opposed to quiescent black holes, such as the black hole placed at the center of the Milky Way).

Despite the fact that the classification of AGN is very wide and articulated, a unified model has been proposed [Krolik and Begelman, 1988]. According to this model, some differences in AGN features could be explained as a result of viewing angle.

In the unified model, two main types of AGN, broad-line (or type I) and narrow-line (type II) are postulated to be the same sort of objects, whose appearance depends on the viewer's line of sight and on the accretion rate [Trump et al., 2011].

The two types are so-named because of the characteristic emission lines observed in their spectra: type I AGN have very broad emission lines and a higher level of continuum emission, while in the type II AGN the broad-line signatures are missing, and instead they present very narrow emission lines and weaker continua.

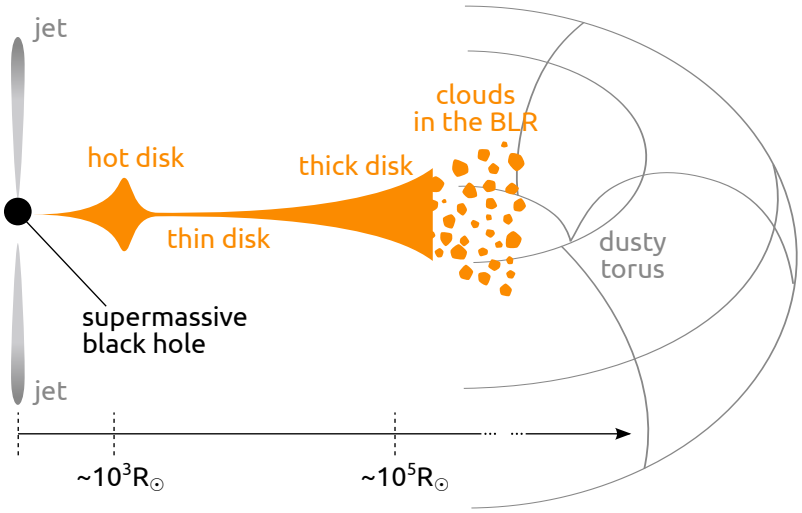

Figure 2: Zoom on the accretion disk of an AGN in a schematic view. Inspiration taken from Carroll and Ostlie [1996, Fig. 26.23].

The idea behind the unification model is that the central supermassive black hole is surrounded by an accretion disk emitting the typical continuum radiation (see Figs. 1 and 2). In the inner region of the accretion disk (within about $10^3 R_\odot$), the radiation pressure is larger than the gas pressure, resulting in a hot, thick disk, which probably accounts for the blue bump in the continuum of the spectrum. Then, up to a distance of $\approx 10^5 R_\odot$, we find a thin disk supported by the gas pressure. This thin disk becomes thicker as the distance increases. Above $\approx 10^5 R_\odot$, the disk breaks into small clouds. This region, called BLR (Broad-Line Region) is responsible for the BELs (Broad Emission Lines) observed in the spectrum of many AGN.

According to the unified model, an obscuring "dusty torus" of gas and dust, optically thick, surrounds the clouds in the BLR.

The NELs (Narrow Emission Lines) are created at a more distant radius outside the torus, in a colder zone called NLR (Narrow-Line Region). As well as the BLR, this region is broken in a distribution of many clouds, which can eventually be photoionized if far enough from the plane of the dusty torus [Carroll and Ostlie, 1996]. The NELs are narrower as the emitting material has lower speeds than in the BLR.

It is possible for the BELs to be hidden by the torus, depending on the angle at which the AGN is seen. The best evidence for this scenario comes from spectropolarimetry observations of some type II AGN [Antonucci, 1993].

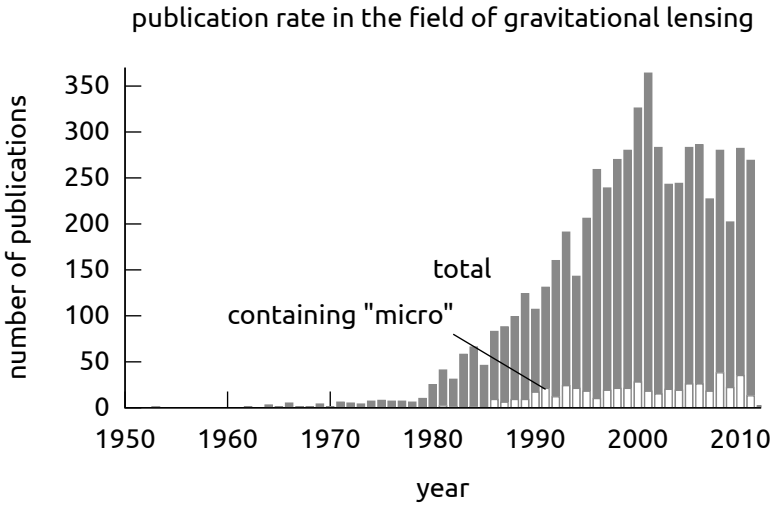

Figure 3: Annual publication rate of scientific papers related to gravitational lensing as a function of time, and fraction of them related to microlensing. Data collected from NASA ADS and updated to December 2011. The data were obtained researching in the title form, with boolean logic, the following string of key words: `(gravitational AND lens) OR (lens AND quasar) OR (image AND quasar) OR (weak AND lens) OR (micro AND lens) OR (microlens)`.

1.2 Gravitationally lensed quasars

According to Einstein's general theory of relativity (dated on 1912 and quoted by Renn et al. [1997]), electromagnetic waves can be bent by a gravitational field. Large mass concentrations such as far galaxies may then act as a sort of imperfect gravitational lenses, and create multiple and magnified images of a background source.

The images of distant objects placed at cosmological distances, like the images of quasars seen from the Earth, can then be affected by gravitational lensing effects, if the observer placed on Earth, the deflecting galaxy and the distant quasar are sufficiently well aligned.

After the discovery of the first gravitational lens system by Walsh et al. [1979], the scientific field of interest for gravitational lenses has grown until it has become a mature branch of astrophysics (see Fig. 3).

It is possible to use gravitational lensing as a cosmological and astrophysical tool, the most interesting applications being the determination of the Hubble parameter H_0, the mass of very distant lensing galaxies as well as the distribution of luminous

and dark matter in the Universe. It is also possible to determine the size and structure of distant quasars from observations of microlensing effects.

1.3 Inverting gravitational lens effects using an optical device

It is possible to retrieve the real source image of a gravitationally lensed quasar, taking full advantage of the magnifying power of the cosmic lens, via numerical lens inversion. This result has been achieved in the past using inverse ray tracing methods for several gravitational lens systems, such as RXJ1131-1231 (see Claeskens et al. [2006], based on a method proposed by Schramm and Kayser [1987]).

Another method to invert a multiply imaged source can be done with an ad hoc optical instrument, specifically designed for a particular source, and placed directly at the telescope [Surdej et al., 2010]. Compared to the numerical methods, this device should allow the direct imaging of fainter features and objects located close to the brighter lensed source.

Such devices could involve either refracting or reflecting surfaces shaped to correct the gravitational lens effects, and specifically adapted to the mass distribution model of the deflector.

1.4 Probing the inner circumnuclear regions around AGN using coronagraphy

A way to inspect the central regions of AGN, or in general to reveal the nature of the host galaxies of distant QSOs, is to use modern coronagraphic systems.

Coronagraphs are instruments capable to catch the central part of the light of a distant object, and then reveal much fainter nearby features. This device is an extension of the concept first proposed by Lyot [1939], which was capable to reveal the faint solar Corona by blocking the light of the Sun, as the Moon does during solar eclipses.

A pioneer study involving coronagraphic devices in the study of quasars and AGN was carried on by Tyson et al. [1982] on the close and bright quasar 3C 273. Afterwards, narrow-band filter observations were carried on by Morris et al. [1993] on the same quasar, using the HST (Hubble Space Telescope) coronagraph.

Specific devices coupled to an adaptive optics system were recently proposed [Tamura et al., 2000], and a deep study by Martel et al. [2003] was capable to provide the most detailed view of the morphology and colors of the host galaxy of 3C 273.

We suggest to use a new concept of coronagraphic device after having inversed the gravitational lens with the *ad hoc* optical instrument proposed in the previous section. This new device introduces an adaptive hologram in the optical scheme, and we present numerical simulations to demonstrate the gain of this device in terms of nulling depth with respect to traditional coronagraphs.

I

Theory, numerical simulations and instrumentation for direct imaging of gravitationally lensed quasars

2 Optical gravitational lens simulators

In this chapter we present the idea of an optical device aimed at inverting the gravitational lens effects caused by a massive deflector in presence of shear effects. We first deal with the mathematical expression of refracting and reflecting surfaces for the case of several centrosymmetric mass distribution models. We then introduce the effect of an external shear and we derive the expression of the corresponding optical surface. Then, we suggest to implement such a device in an instrument, with the aim to observe multiply imaged quasars analogically unlensed and reconstructed on the detector. Pairing this instrument with a coronagraph device could provide the nulling of the central zones of a bright quasar or a bright AGN and could allow the inspection of much fainter close features.

In Sect. 2.1 we present the basic concepts of gravitational lensing. In Sect. 2.2 we mathematically describe the shapes of the refracting and reflecting surfaces that could inverse the gravitational lens effects for the case of several mass distribution models (Sects. 2.3 and 2.4). Then we present an overview of laboratory simulations already carried on by our team (Sect. 2.5), and we study the effect of an external shear and the corresponding optical surface capable to reproduce or invert such an effect (Sect. 2.6). Finally, Sect. 2.7 introduces the concept of an instrument aimed at analogically invert such gravitational mirages.

2.1 Gravitational lensing

Under normal circumstances, the light of a distant source S travels following a straight path. An observer O sees a single image I of the source S, located exactly along the direction of the incoming light ray. As shown in Fig. 4a, the real position of the source S coincides in this case with that of the image I.

There are several and different situations in nature where a light ray, or an electromagnetic wave in general, does not propagate following a straight path, but instead follows a bent path. For example, the presence of a temperature gradient above the ground may induce deflections of light rays during their prop-

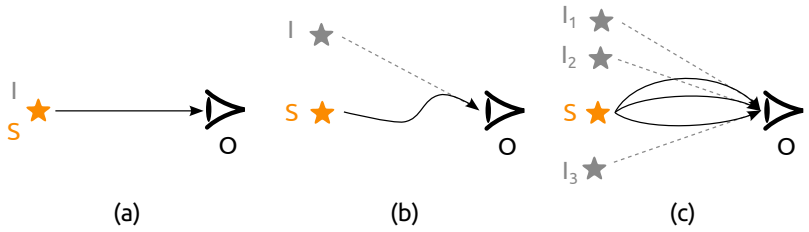

Figure 4: Different types of light ray propagation between a distant source S and an observer O. The observer O either sees (4a) a single, (4b) a slightly displaced or (4c) multiple images I_i of the background source S. Inspiration taken from Surdej et al. [2008].

agation. This is caused by the fact that temperature differences in the density of air induce a variation in the refraction index n: the light ray from S does not propagate straight, but instead follows the path that minimizes the travel time (Fermat Principle), and the image I is seen by the observer O as placed at a different position with respect to the source S, as in Fig. 4b. This is what is commonly called an atmospheric "mirage".

In other cases, the pattern of the temperature gradients is such that it is possible to have the formation of multiple images (for example the images I_1, I_2 and I_3 of the single source S shown in Fig. 4c). Note that the observer O always sees the corresponding images along the direction which is tangent to the incoming light ray.

Because of the difference in the length of the path between the multiple images, and of the light velocities $v = c/n$ where c stands for the speed of light in the vacuum, there will generally be a time delay between the arrival times at O of the signal oncoming from S. This delay, depending on n and also on the absolute distance between O and S, causes the fact that the multiple images $I_i = I_1, I_2$ and I_3 show at different times a same eventual increase or decrease in flux of the source S.

The deviation of the light rays may also be caused by a strong gravitational field. According to Einstein's general theory of relativity (dated on 1912 and quoted by Renn et al. [1997]), a gravitational field bends electromagnetic waves in much the same way as the atmospheric effect described above. Large mass concentrations in the Universe, such as stars and galaxies, can act as a sort of gravitational lens. In this case, that we call gravitational optics, it is possible to study the propagation of the rays of light attributing to the space a refraction index $n = (1 - 2U/c^2)$, where U represents the Newtonian gravitational potential.

In analogy with an atmospheric mirage, when light rays are curved by the gravitational field of a massive object located between a distant source and the observer, there may be, as a result, the formation of a gravitational mirage, that is also called multiple gravitationally lensed images or still a gravitational lens system.

Unlike most astrophysical discoveries made during the past century, the physics of gravitational lensing was understood well before that the first example of a multiply imaged source was found [Renn et al., 1997]. The existence of multiply imaged, distant sources had been predicted by Zwicky [1937], although the first case of a doubly imaged quasar was only reported by Walsh et al. [1979].

Einstein [1915] showed that a massive object curves the spacetime in its neighborhood and that any particle, massive or not (for example the photons), will move along the geodesics of this curved space. He found that a light ray passing at a distance (impact parameter) ξ from an object characterized by an axially symmetric mass distribution $M(\xi)$ (see Fig. 5a) will undergo a total deflection angle α, expressed in radian, by means of the relation

$$\alpha = \frac{4GM(\xi)}{c^2\xi} = \frac{2R_{sc}}{\xi}, \tag{2.1}$$

where G stands for the gravitational constant, and R_{sc} represents the Schwarzschild radius associated with the mass M, which is the distance from the center of an object such that the escape speed from its surface would be equal to the speed of light c. For an extended mass, it is easy to calculate the deflection angle by integrating the individual deflections due to all the mass elements constituting the lens.

Usually, the mass acting as the lens has a small size compared to the distances between the source, the observer and the deflector, then we do not take into account the thickness of this lens (thin lens approximation).

If the source S, an observer O (as O_1 in Fig. 5a) and an axially symmetric deflector D are perfectly aligned, then the observer will see the background source as a ring of light (the so-called Einstein ring) which angular radius Θ_E is proportional to the square root of the mass of the deflector [Refsdal and Surdej, 1994]:

$$\Theta_E = \sqrt{\frac{4GM(\xi)}{c^2}\frac{D_{DS}}{D_{OD}D_{OS}}}. \tag{2.2}$$

If the alignment between the source, the deflector and the observer is not perfect, then the ring breaks into several images.

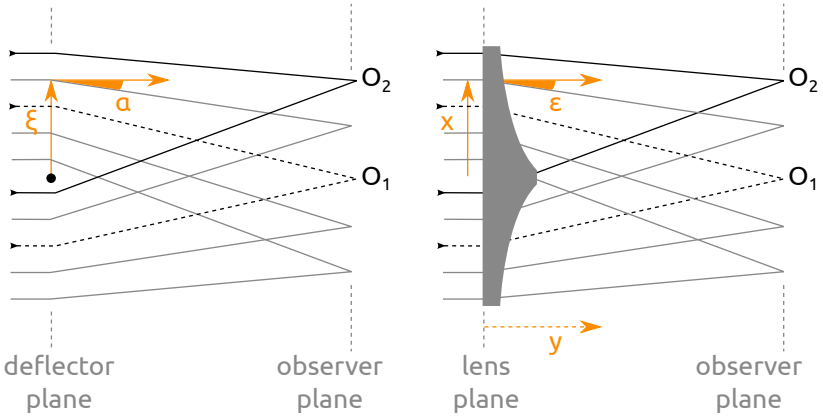

(a) Gravitational lensing (b) Optical lens experiment

Figure 5: Gravitational lens deflection of a beam of parallel light rays coming from a very distant source located at left (5a). In this case, the deflector is supposed to consist of a massive compact object represented by the black dot, and the light deflection angle α is given by Eq. (2.1). The observer O_2 always sees two lensed images of the distant source, except in the perfect symmetric case for which the observer O_1 sees a complete Einstein ring. At right (5b) is shown the shape of an optical lens that accounts for the same deviation of the beam of parallel light rays The optical lens looks like the foot of an inclined (at 90°) glass of wine. The observers at O_1 and O_2 in 5b see similar mirages as the corresponding observers in 5a. Inspiration taken from Surdej et al. [2008].

A sufficient condition for a gravitational lens to produce multiple images of a background source is simply that its surface mass density $\Sigma(\xi)$ exceeds the critical surface density Σ_c, which only depends on the relative angular distances D_{OD}, D_{OS} and D_{DS}, between the observer (O), the deflector (D) and the source (S) [Refsdal and Surdej, 1994, Claeskens and Surdej, 2002]:

$$\Sigma_c = \frac{c^2}{4\pi G}\frac{D_{OS}}{D_{OD}D_{DS}}. \tag{2.3}$$

2.2 Simulator with optical surfaces

Adopting a given mass distribution model, one can construct an optical device (a transparent lens or a reflecting surface) that deflects light rays accordingly (see Fig. 5b), thus enabling us to study very simply in the laboratory the lensing properties of

black holes, stars, quasars, galaxies, etc. as they exist in the Universe.

In principle, it should also be possible to activate an optical surface capable of restoring in real time, in the focal plane of the instrument, the unlensed image of the multiply imaged quasar being observed at the telescope. At the same time, such a system would take advantage from the magnification provided by the lensing galaxy, enabling us to study very distant objects with an improved angular resolution.

The surface of an eventual optical lens is determined in such a way that rays characterized by an impact parameter $x = \xi$ are being deflected by the angle $\varepsilon(x) = \alpha(\xi)$ (see Figs. 5a and 5b). The angle $\varepsilon(x)$ is of course directly related to the refraction properties of the lens (shape of its surface and value of the refraction index n).

If we would build an instrument based on a reflective surface instead of a refracting lens, we would have two choices: the normal reflection approach, whose results would be analogue to the case of the transparent lens; or the grazing reflection.

Following the Snell-Descartes law of refraction and the law of reflection, and in the approximation of small ε, we have that the refracted/reflected light ray angle r is

$$r = \frac{\varepsilon}{n-1} \tag{2.4}$$

for the case of refraction,

$$r = \frac{\varepsilon}{2} \tag{2.5}$$

for the case of normal reflection, and finally

$$r = \tan\left(\frac{\pi}{2} - \frac{\varepsilon}{2}\right) = -1/\tan\frac{\varepsilon}{2} = -\frac{2}{\varepsilon} \tag{2.6}$$

for the case of grazing reflection.

In the following sections, we describe the equations of these optical surfaces for several mass distribution models. The solutions are already known from the one dimensional approach [Surdej et al., 2010] as the models are centrosymmetric.

2.3 Light refraction and normal reflection

We propose to calculate the shape of the optical surfaces as a function of the two spatial coordinates x_i: x_1 and x_2.

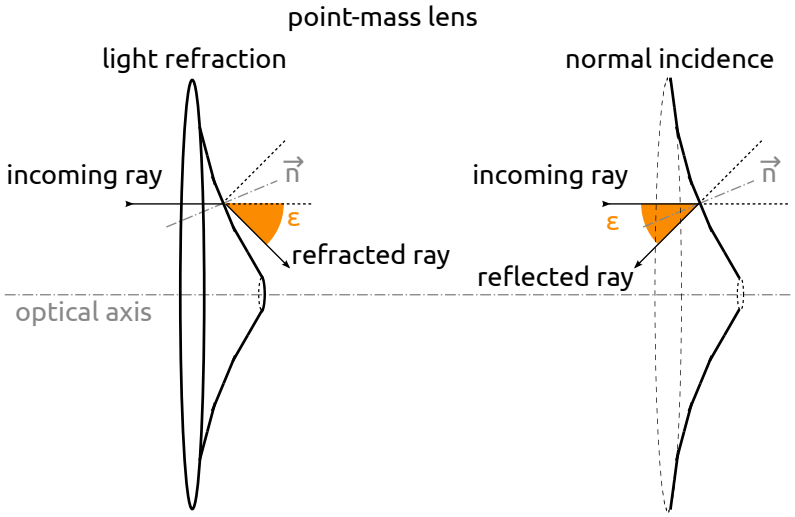

Figure 6: Example of surfaces representing light refraction and normal reflection for the case of a point-mass lens model. $\vec{n}$ represents the normal to the surface at a given reflection point.

We will note as $y = f(x_1, x_2)$ the shape of the surface; and for simplicity we will consider flat the other side of the lens for the case of light refraction (see Fig. 6) and we note with x_{1_0} and x_{2_0} the coordinates of the points located at the edge of the optical lenses.

The shape of the surface for the models that we will first consider here is rotationally symmetric, then a one dimensional approach is sufficient, and the results are already known. Anyway, the two dimensional approach will turn to be useful and necessary while calculating the contribution due to an external shear, which is not symmetric. A brief description of the one dimensional symmetric approach is given in Appendix A.

We have in general for each dimension that

$$\frac{\partial y}{\partial x_i} = -\frac{\varepsilon}{n-1} = \frac{-4G}{c^2(n-1)} \frac{x_i}{x} \frac{M(x)}{x} \tag{2.7}$$

in the case of light refraction, while for normal reflection case we have a similar expression:

$$\frac{\partial y}{\partial x_i} = -\frac{\varepsilon}{2} = \frac{-2G}{c^2} \frac{x_i}{x} \frac{M(x)}{x}, \tag{2.8}$$

with $x = \sqrt{x_1^2 + x_2^2}$ and for the approximation of small ε.

We calculate the shape of the surface by substituting in the previous equation the expression of $M(x)$ and then integrating. The solution is given separately for three different lens models:

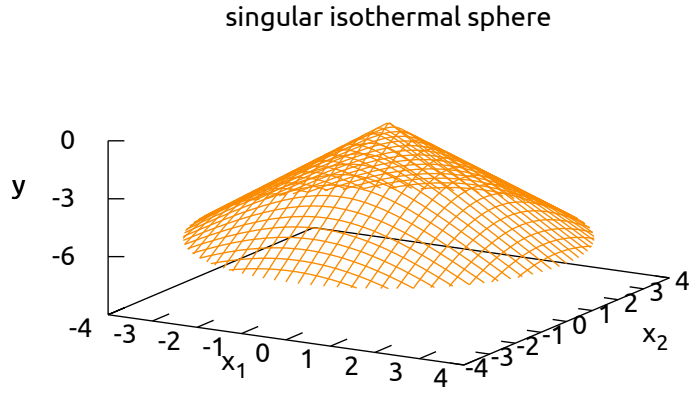

Figure 7: Shape of the surface corresponding to the SIS lens model calculated for the case of light refraction and normal reflection.

SIS (Singular Isothermal Sphere), PM (Point-Mass) lens and UD (Uniform Disk).

2.3.1 Singular isothermal sphere

For the SIS lens model, the spherical distribution of mass is such that it grows linearly with the impact parameter. In this case we have

$$M(x) = kx, \tag{2.9}$$

then, for the case of light refraction,

$$\begin{aligned} f(x_1, x_2) &= \int_{x_{i0}}^{x_i} \frac{-4Gk}{c^2(n-1)} \frac{x_i'}{\sqrt{x_1'+x_2'}} dx_i' \\ &= \frac{-4Gk}{c^2(n-1)} \left(\sqrt{x_1^2+x_2^2} - \sqrt{x_{10}^2+x_{20}^2} \right), \end{aligned} \tag{2.10}$$

while for normal reflection we find

$$\begin{aligned} f(x_1, x_2) &= \int_{x_{i0}}^{x_i} \frac{-2Gk}{c^2} \frac{x_i'}{\sqrt{x_1'+x_2'}} dx_i' \\ &= \frac{-2Gk}{c^2} \left(\sqrt{x_1^2+x_2^2} - \sqrt{x_{10}^2+x_{20}^2} \right). \end{aligned} \tag{2.11}$$

The calculated shape of the lens is conic, where the slope of the surface is given by the constant k. An example of this kind of surface is shown in Fig. 7.

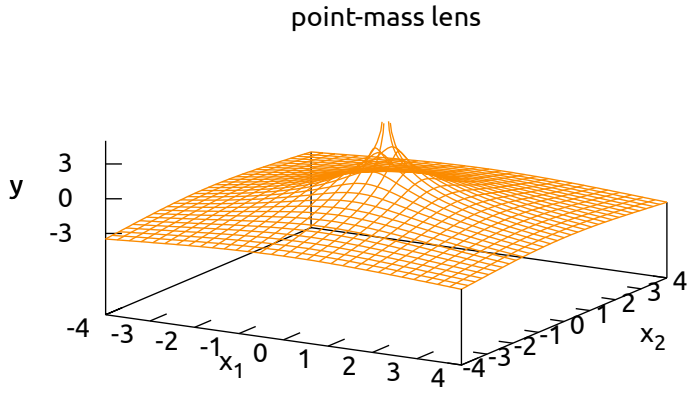

Figure 8: Shape of the surface corresponding to the PM lens model calculated for the case of light refraction and normal reflection.

2.3.2 Point-mass lens

For the PM lens model, the mass M is concentrated in one singular point (cf. the case of a black hole, or in general for compact lenses). In this case, the mass distribution does not depend on the impact parameter. We have

$$M(x) = M, \tag{2.12}$$

and then, for the case of light refraction,

$$\begin{aligned} f(x_1, x_2) &= \int_{x_{i0}}^{x_i} \frac{-4GM}{c^2(n-1)} \frac{x_i'}{x_1' + x_2'} dx_i' \\ &= \frac{-4GM}{c^2(n-1)} \ln\left(\frac{\sqrt{x_1^2 + x_2^2}}{\sqrt{x_{10}^2 + x_{20}^2}} \right). \end{aligned} \tag{2.13}$$

Concerning the case of normal reflection, we find

$$\begin{aligned} f(x_1, x_2) &= \int_{x_{i0}}^{x_i} \frac{-2GM}{c^2} \frac{x_i'}{x_1' + x_2'} dx_i' \\ &= \frac{-2GM}{c^2} \ln\left(\frac{\sqrt{x_1^2 + x_2^2}}{\sqrt{x_{10}^2 + x_{20}^2}} \right). \end{aligned} \tag{2.14}$$

For this model, we find that the optical lens is shaped like the foot of a wine glass. An example of this kind of surface is given in Fig. 8.

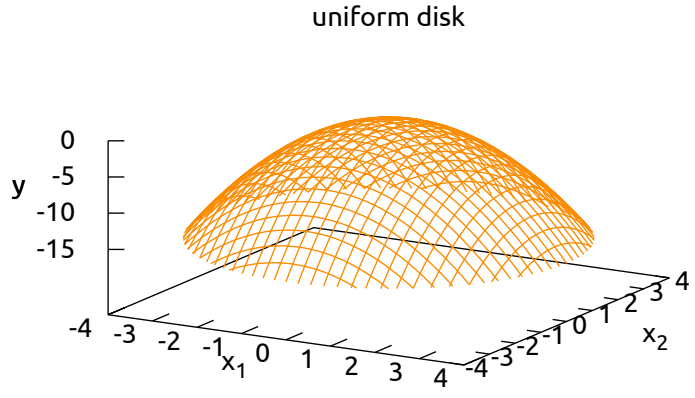

Figure 9: Shape of the surface corresponding to the UD lens model calculated for the case of light refraction and normal reflection.

2.3.3 Uniform disk

A uniform circular disk of matter acts as a perfect converging lens, making possible the convergence of all incoming light rays from a distant source into a single point, if the line-of-sight is perpendicular to the disk. We then assume that the surface mass density Σ_0 is constant for values of the impact parameter between x_{i0} and a given x_i:

$$M(x) = \pi\Sigma_0 x^2, \tag{2.15}$$

then, for the case of light refraction

$$\begin{aligned} f(x_1, x_2) &= \int_{x_{i0}}^{x_i} \frac{-4G\pi\Sigma_0}{c^2(n-1)} x_i' dx_i' \\ &= \frac{-2G\pi\Sigma_0}{c^2(n-1)} \left[(x_1^2 + x_2^2) - (x_{10}^2 + x_{20}^2)\right], \end{aligned} \tag{2.16}$$

and for the case of normal reflection

$$\begin{aligned} f(x_1, x_2) &= \int_{x_{i0}}^{x_i} \frac{-2G\pi\Sigma_0}{c^2} x_i' dx_i' \\ &= \frac{-G\pi\Sigma_0}{c^2} \left[(x_1^2 + x_2^2) - (x_{10}^2 + x_{20}^2)\right], \end{aligned} \tag{2.17}$$

so that the shape of this converging lens follows a parabolic law. An example of this kind of surface is shown in Fig. 9.

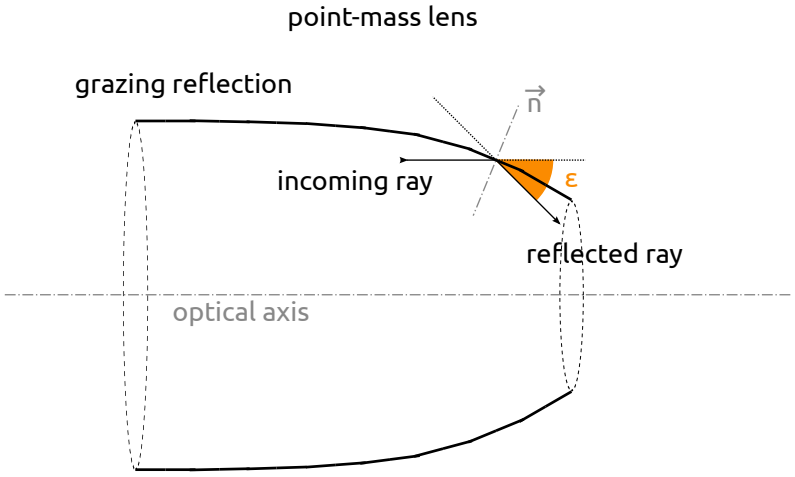

Figure 10: Example of a grazing reflection for the case of a point-mass lens model. $\vec{n}$ represents the normal to the surface at a given reflection point.

2.4 Grazing reflection

One can imagine another kind of reflective instrument to simulate or to inverse the effect of a gravitational lens: if the reflection of the light on the mirror is not normal but grazing (see Fig. 10), then the shape of the surface presented in Sect. 2.3 is different.

A practical implementation of these surfaces to simulate the gravitational lens effects, or to correct them, could involve off-axis optical elements, but the solutions are reported for completeness and to offer an alternative way to stack the several elements in the framework of the implementation of an instrument. Moreover, these solutions could be more useful for wavelengths different from the visible, as for example X-rays.

In this case we have that

$$\frac{\partial y}{\partial x_i} = \frac{2}{\varepsilon} = \frac{c^2}{2G}\frac{x_i}{x}\frac{x}{M(x)}, \tag{2.18}$$

and we find, for the same mass distribution models as those chosen for the cases of light refraction and normal reflection (SIS, PM and UD), the surfaces shown in Figs. 11, 12 and 13 and briefly mathematically described in the next subsections.

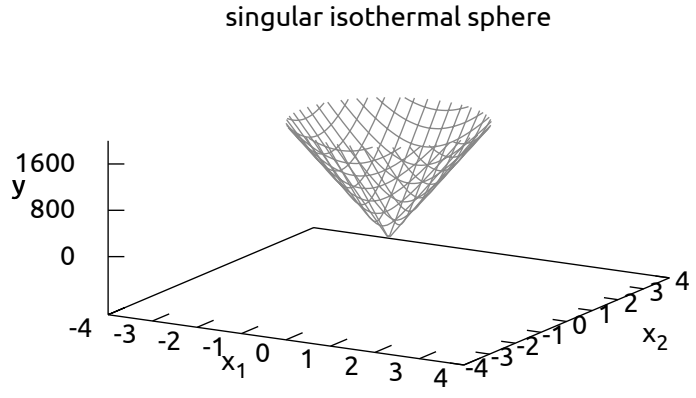

Figure 11: Shape of the surface corresponding to the SIS lens model calculated for the case of grazing reflection.

2.4.1 Singular isothermal sphere

We start again from the expression of a mass growing linearly with the parameter impact x:

$$M(x) = kx \tag{2.19}$$

then the equation of the surface is

$$\begin{aligned} f(x_1, x_2) &= \int_{x_{i0}}^{x_i} \frac{c^2}{2Gk} \frac{x_i'}{\sqrt{x_1'^2 + x_2'^2}} dx_i' \\ &= \frac{c^2}{2Gk} \left(\sqrt{x_1^2 + x_2^2} - \sqrt{x_{10}^2 + x_{20}^2} \right). \end{aligned} \tag{2.20}$$

The surface of a lens that reproduces or corrects this deflection in the case of grazing reflection is conical. The result is analogue to the one that we found for the case of normal reflection, with the exception that the slope of the cone is here very high.

The relation between the two slopes can be seen by comparing the constant in the two equations. In particular, the slope for grazing reflection is the inverse of the one calculated for normal reflection. As only a part of this cone should be considered (the light must continue its path as in Fig. 10), it is better to visualize this surface as a "conical ring".

An example of this kind of surface is shown in Fig. 11.

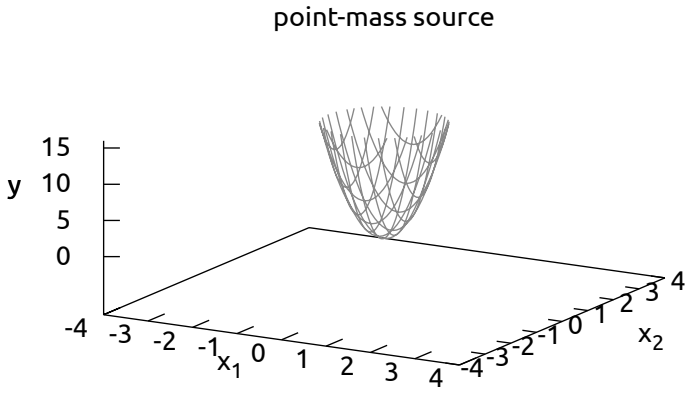

Figure 12: Shape of the surface corresponding to the PM lens model calculated for the case of grazing reflection.

2.4.2 Point-mass lens

For the case of a lens which is point-like, as for example a very compact object, we have again that the mass does not depend on the parameter impact x, then we start as in the case of normal reflection with

$$M(x) = M, \tag{2.21}$$

and we integrate the shape of the surface:

$$\begin{aligned} f(x_1, x_2) &= \int_{x_{i0}}^{x_i} \frac{c^2}{2GM} x_i' dx_i' \\ &= \frac{c^2}{4GM} \left[(x_1^2 + x_2^2) - (x_{10}^2 + x_{20}^2) \right]. \end{aligned} \tag{2.22}$$

Note that, as opposed to the case of the point-mass deflector where the surface was shaped like the foot of a wine glass, we obtain here a paraboloid instead of the logarithmic surface.

It is better to visualize this surface as a parabolic "ring" section, (see Fig. 10). In fact only the external part, where the reflection angle is grazing, is used.

An example of this kind of surface (not truncated into a ring) is shown in Fig. 12.

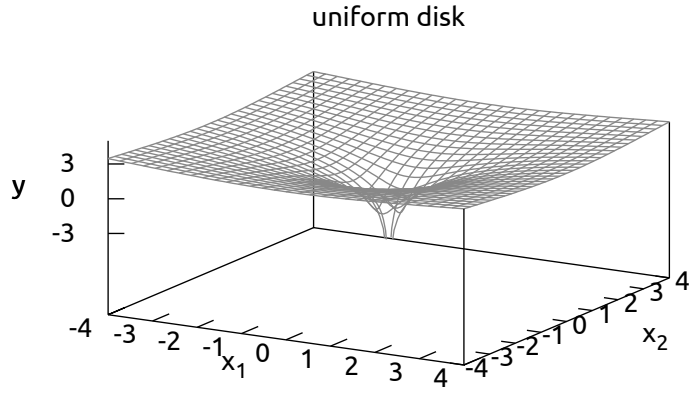

Figure 13: Shape of the surface corresponding to the UD lens model calculated for the case of grazing reflection.

2.4.3 Uniform disk

Finally, we start from the expression of the mass distribution of a Uniform Disk of matter

$$M(x) = \pi\Sigma_0 x^2, \tag{2.23}$$

and we obtain

$$\begin{aligned} f(x_1, x_2) &= \int_{x_{i0}}^{x_i} \frac{c^2}{2G\pi\Sigma_0} \frac{x_i'}{x_1' + x_2'} dx_i' \\ &= \frac{c^2}{2G\pi\Sigma_0} \ln\left(\frac{\sqrt{x_1^2 + x_2^2}}{\sqrt{x_{10}^2 + x_{20}^2}} \right), \end{aligned} \tag{2.24}$$

which is a surface that follows a logarithmic law, instead of the parabolic shape that we found in the case of normal reflection. As in the previous cases, only a "ring" of this surface should be considered.

An example of this kind of surface is shown in Fig. 13.

2.5 Laboratory simulations

For didactic purposes, an optical lens, shaped for the case of a point-mass lens, was manufactured, and several optical tests were performed by Surdej et al. [2008] in the framework of the

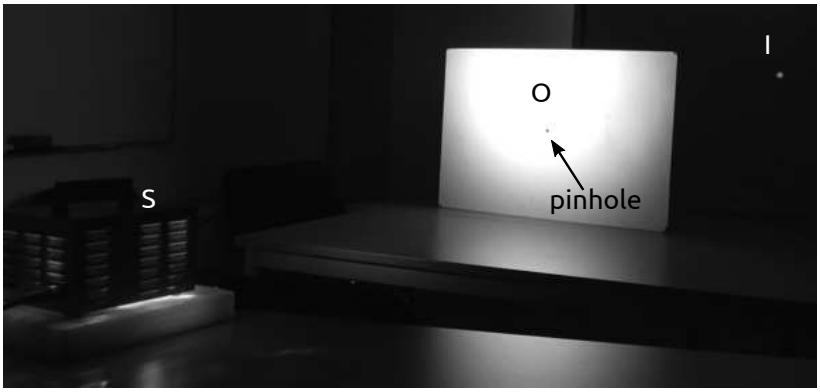

Figure 14: In the absence of a gravitational lens located along the light rays, the pinhole camera projects on the background screen a single image of the light source.

"optical gravitational lens experiment". The pictures of this section are elaborated from those of that paper.

In Fig 14 is presented a laboratory setup in the absence of a deflector. A compact light source S is located on the left. The large background screen is illuminated uniformly, and the observer O only sees the single image I of a distant quasar.

In order to simulate the formation of lensed images for the case of this point-mass deflector, the optical setup shown in Fig. 15 was used. The optical lens D bends the light rays like a point-mass deflector. On the other side of the lens, a white screen with a very small pinhole at its center, simulates the eye of an observer O or in general the aperture of a telescope. Beyond the white screen, the lensed image I of the lensed source is projected on another screen, opaque. In this case, the alignment between the source, the deflector and the observer (pinhole) is perfect, and the image I of the source, projected on the opaque screen, is an Einstein ring.

In the setup shown in Fig. 15, neither the pinhole screen nor the background one are any longer uniformly illuminated. A zoom of the observer and image screens is presented in Fig. 16a: the deflector redistributes the light in such a way that there is a maximum of light concentration along a bright focal line connecting the source and the lens. As the point-mass deflector acts as an imperfect lens, there is not a single focus: the bright spot near the pinhole is obtained from the intersection of this bright focal line with the pinhole screen.

If the pinhole lens is not perfectly placed on the bright spot (see Fig. 16b), the Einstein ring breaks in two lensed images with a typical angular separation equal to $2\Theta_E$.

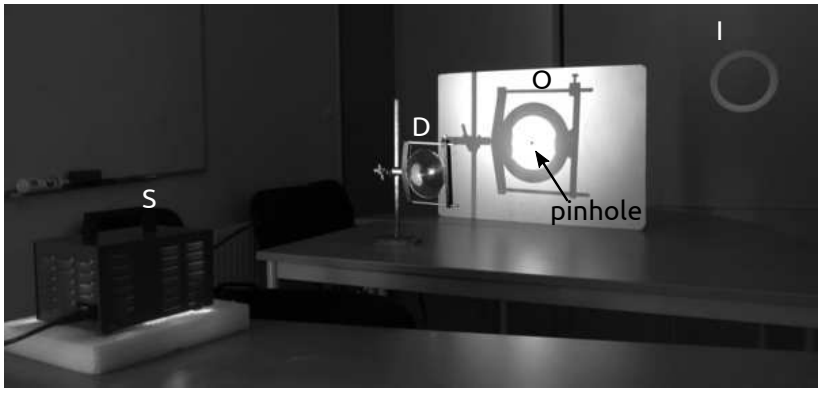

Figure 15: Setup of the gravitational lens experiment. The optical gravitational lens (black hole type deflector) has been set perpendicularly to, and centered on the line joining the pinhole and the light source (see the text for details).

2.6 External shear

Gravitational lens systems characterizable by symmetrical mass distributions must be very rare: usually either the deflector itself is not symmetric, or the presence of neighboring companions will naturally induce an asymmetry in the lens mass distribution. If these masses are far enough, their contribution can be considered as constant, and we refer to this effect as an external shear.

The deflection obtained from a symmetrical model (as for example an SIS model) with an external shear can be represented by the sum of an isotropic part $\alpha_{SIS}(x_1, x_2)$ and an anisotropic part $\alpha_{an}(x_1, x_2)$, and

$$\alpha(x_1, x_2) = \alpha_{SIS}(x_1, x_2) + \alpha_{an}(x_1, x_2), \tag{2.25}$$

where

$$\alpha_{an}(x_1, x_2) = \gamma \begin{pmatrix} x_1 \\ -x_2 \end{pmatrix} \tag{2.26}$$

and γ is the intensity of the shear. A complete explanation of this effect may be found in Claeskens [1999].

a didactic but incorrect way to show a shear-like effect is to tilt the optical lens

In the framework of the simulations of gravitational lenses using optical devices, Refsdal and Surdej [1994], Surdej et al. [2010] proposed to tilt with respect to the line connecting the source and the lens the optical lens (for example that one representing the PM model described in Sect. 2.3.2). The bright focal line along the optical axis that existed in the symmetric configuration, whose section is seen as a bright point on the pinhole screen

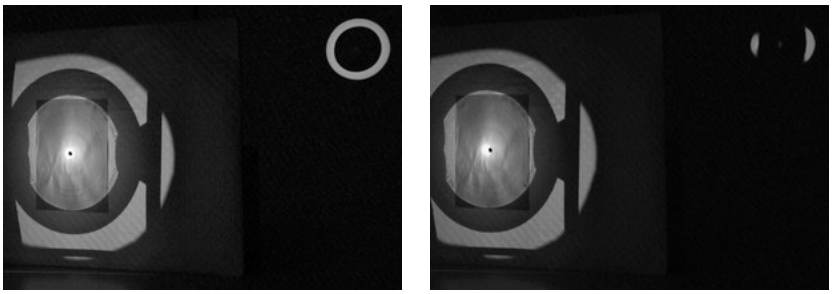

(a) The pinhole is on the symmetry axis, showing the Einstein ring on the background screen.

(b) As the pinhole is set slightly away from the symmetry axis, the Einstein ring breaks up in two lensed images.

Figure 16: The optical gravitational lens experiment corresponding to the case of a black hole deflector slightly on- and off-axis.

(see Figs. 16a and 16b) then breaks into a three-dimensional envelope, called the caustics. A section of this caustics is visible on the pinhole screen as a diamond-shaped curve with four folds and four cusps (see Figs. 17a and 17b).

why tilting the lens is not equivalent to introducing an external shear

Despite the tilt seems to reproduce very well the effect of an external shear, and it can be very useful for didactic demonstrations, it is not mathematically equivalent to the above-mentioned effect.

Jean Surdej and I proved this for the SIS lens model in the case of normal reflection, (see Sect. 2.3.1), that we know to be represented by a conical surface. Given the equation of the cone

$$x_1^2 + x_2^2 = k^2 y^2, \tag{2.27}$$

with

$$k = \tan\alpha = \frac{\sqrt{x_1^2 + x_2^2}}{y}, \tag{2.28}$$

we define

$$\frac{\partial y}{\partial x_i} = \frac{\partial}{\partial x_i}\frac{\sqrt{x_1^2 + x_2^2}}{k} = \frac{x_i}{k^2 y}, \tag{2.29}$$

so the coordinates of the two tangents to the surface on a generic point y are

$$\vec{t}_{x_1} = \left(1,\ 0,\ \frac{x_1}{k^2 y}\right) \tag{2.30}$$

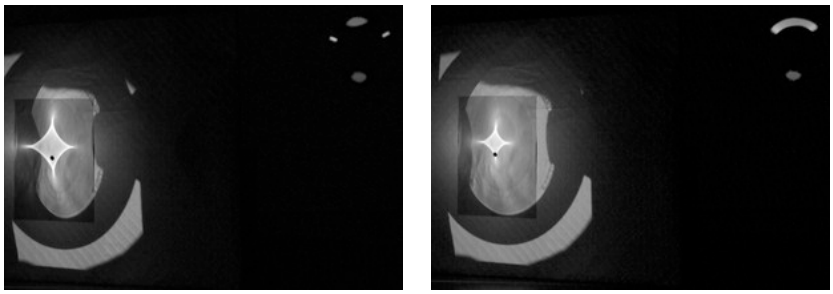

(a) The pinhole is located inside the caustics: we have the formation of four images.

(b) The symmetry is broken by tilting the deflector. The pinhole is placed on the cusp of the caustics and three of the four images merge.

Figure 17: The optical gravitational lens experiment corresponding to the case of a black hole deflector that has been slightly tilted around its vertical axis. The bright (pseudo focal) line along the optical axis which existed in the symmetric configuration (see Figs. 16a and 16b) has changed into a two dimensional caustic surface, a section of which is seen as a diamond shaped caustic (made of four folds and four cusps) in the pinhole plane. Seen on the background screen, the Einstein ring is now split into four distinct lensed images (Fig. 17a), or in three merging lensed images plus a very faint one on the other side (Fig. 17b).

and

$$\vec{t}_{x_2} = \left(0,\ 1,\ \frac{x_2}{k^2 y}\right), \tag{2.31}$$

and the components of the normal to the surface $\vec{N} = \vec{t}_{x_1} \times \vec{t}_{x_2}$, normalized, are

$$\vec{n}_{x_1} = \left(-\frac{x_1}{k^2 y}\right) \Big/ \sqrt{1 + \frac{1}{k^2}} \tag{2.32}$$

and

$$\vec{n}_{x_2} = \left(-\frac{x_2}{k^2 y}\right) \Big/ \sqrt{1 + \frac{1}{k^2}}, \tag{2.33}$$

that is to say, a light ray parallel to the axis of the cone is deflected by an angle ε such that

$$\cos\varepsilon = \vec{N} \cdot \vec{\ell} = \frac{1}{1 + 1/k^2} = \sin\alpha = \cos(\pi - \alpha), \tag{2.34}$$

where $\vec{\ell}$ represents a vector parallel to the axis of the cone.

If we tilt the cone around the x_2 axis by an angle θ we obtain the following transformation of coordinates:

$$\begin{cases} x_1' = x_1 \cos\theta - y \sin\theta \\ x_2' = x_2 \\ y' = x_1 \sin\theta + y \cos\theta. \end{cases} \tag{2.35}$$

In the system of coordinates x_1', x_2' and y', the equation of the tilted cone is

$$x_1'^2 + x_2'^2 = k^2 y'^2, \tag{2.36}$$

always with $k = \tan\alpha = 1/\tan\varepsilon \approx 1/\varepsilon$. Then, substituting the values in Eq. 2.35, we obtain the expression of the tilted cone in the system of coordinates x_1, x_2 and y, which is

$$(x_1 \cos\theta - y \sin\theta)^2 + x_2^2 = (x_1 \sin\theta + y \cos\theta)^2 k^2, \tag{2.37}$$

and after some development

$$\begin{aligned} y^2(\sin^2\theta - k^2\cos^2\theta) - 2x_1 y(1+k^2)\sin\theta\cos\theta \\ + x_1^2(\cos^2\theta + k^2\sin^2\theta) + x_2^2 = 0 \end{aligned} \tag{2.38}$$

which can be solved for y obtaining two solutions:

$$y_{1,2} = \frac{-x_1(1+k^2)\sin\theta\cos\theta \mp \sqrt{k^2(x_1^2+x_2^2) - (1+k^2)x_2^2\sin^2\theta}}{k^2 - (1-k^2)\sin^2\theta}. \tag{2.39}$$

We take the positive solution and we obtain that the two components of the normal vector are

$$n_{x_i} = -2\frac{dy}{dx_i} \Big/ \sqrt{1 + \left(\frac{dy}{dx_1}\right)^2 + \left(\frac{dy}{dx_2}\right)^2}, \tag{2.40}$$

where, posing

$$a = \sqrt{k^2(x_1^2+x_2^2) - (1+k^2)x_2^2\sin^2\theta}, \tag{2.41}$$

$$b = k^2 - (1-k^2)\sin^2\theta, \tag{2.42}$$

we have that

$$\frac{dy}{dx_1} = \frac{-\Big((1+k^2)\sin\theta\cos\theta\Big) + \dfrac{k^2 x_1}{a}}{b}, \tag{2.43}$$

$$\frac{dy}{dx_2} = \frac{-\Big((1+k^2)x_2\sin^2\theta - k^2 x_2\Big)\dfrac{1}{a}}{b}. \tag{2.44}$$

Under the assumption that $\theta \ll 1$ and $k \gg 1$, the previous derivatives become

$$\frac{dy}{dx_1} = \frac{x_1}{ky}\frac{-(1+k^2)\theta}{k^2}, \tag{2.45}$$

$$\frac{dy}{dx_2} = \frac{x_2}{ky}, \tag{2.46}$$

and once again a light ray parallel to the axis of the tilted cone is deflected by a value such that

$$\cos\varepsilon = \vec{N}\cdot\vec{\ell} = \frac{1}{1+1/k^2+\theta^2-2\theta x_1/ky}. \tag{2.47}$$

The components of the normal vector are then

$$n_{x_1} = \left(\frac{-x_1}{ky}+\theta\right)\Big/\sqrt{1+\frac{1}{k^2}+\theta^2-\frac{2\theta x_1}{ky}}, \tag{2.48}$$

$$n_{x_2} = \left(\frac{x_2}{ky}\right)\Big/\sqrt{1+\frac{1}{k^2}+\theta^2-\frac{2\theta x_2}{ky}}. \tag{2.49}$$

If $\theta = 0$, we recover the previous results. Since $1/\sqrt{1+x} \approx 1 - x/2$, we can re-write the previous components of the $\vec{n} = (n_x, n_y)$ vector by separating it in an isotropic and an anisotropic components: $\vec{n} = \vec{n}_{SIS} + \vec{n}_{nSIS}$, where

$$\vec{n}_{SIS} = \left(\frac{-x_1}{ky}, \frac{-x_2}{ky}\right), \tag{2.50}$$

$$\vec{n}_{an} = \left(\theta + \frac{x_1^2}{y^2} + \frac{\theta^2 x_1}{ky} - \frac{\theta}{k^2}, -\frac{\theta}{k^2}\frac{x_1 x_2}{y^2}\right). \tag{2.51}$$

As it can be seen, the anisotropic part does not represent an external shear.

In the next subsections we derive the exact expression for this effect in the cases of light refraction, normal reflection and grazing reflection, in analogy with the results obtained for the symmetrical lens models.

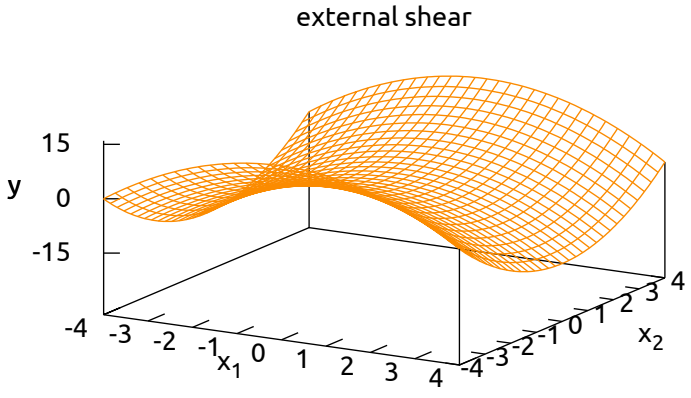

Figure 18: Shape of the surface corresponding to an external shear for the case of light refraction and normal reflection.

2.6.1 Shear for light refraction and normal reflection

exact expression for the external shear

To find the mathematical expression for the optical surface of a simulator transmitting the deflected rays by refraction and normal reflection due to an external shear, we modify the Eq. 2.7 such that we have now

$$\frac{\partial y}{\partial x_i} = -\frac{c}{n-1}(\pm x_i), \tag{2.52}$$

and for the case of normal reflection

$$\frac{\partial y}{\partial x_i} = -\frac{c}{2}(\pm x_i). \tag{2.53}$$

Integrating, we find

$$\begin{aligned} f(x_1, x_2) &= \int_{x_{i0}}^{x_i} -\frac{c}{n-1}(\pm x_i')dx_i' \\ &= -\frac{c}{2(n-1)}\left[(x_1^2 - x_2^2) - (x_{10}^2 - x_{20}^2)\right], \end{aligned} \tag{2.54}$$

while for normal reflection we find

$$\begin{aligned} f(x_1, x_2) &= \int_{x_{i0}}^{x_i} -\frac{c}{2}(\pm x_i')dx_i' \\ &= -\frac{c}{4}\left[(x_1^2 - x_2^2) - (x_{10}^2 - x_{20}^2)\right]. \end{aligned} \tag{2.55}$$

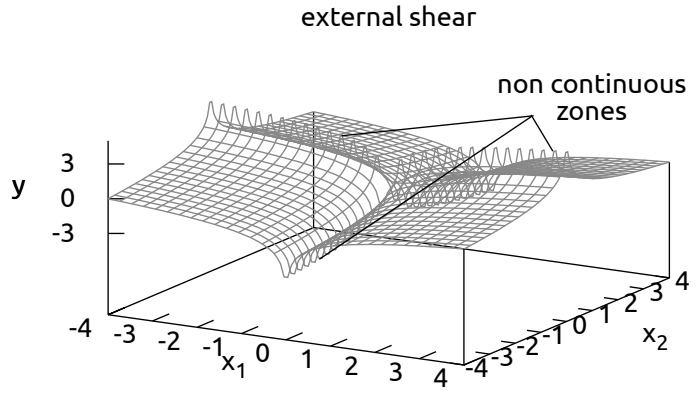

Figure 19: Shape of the theoretical surface corresponding to an external shear for the case of grazing reflection. The surface presents non continuous zones.

The effect of an external shear can then be corrected with an optical lens or a reflecting surface having the shape of an hyperbolic paraboloid (horse saddles), where the direction of the axis is given by the direction of the shear, and the slope of the paraboloid is given by its intensity. An example of this kind of surface is shown in Fig. 18.

2.6.2 Shear for grazing reflection

For grazing reflection we start from

$$\frac{\partial y}{\partial x_i} = -\frac{2}{c(\pm x_i)}, \tag{2.56}$$

and we have

$$\begin{aligned} f(x_1, x_2) &= \int_{x_{i0}}^{x_i} -\frac{2}{c(\pm x_i')} dx_i' \\ &= -\frac{2}{c}\left[\ln\left(\frac{x_1^2}{x_2^2}\right) - \ln\left(\frac{x_{10}^2}{x_{20}^2}\right)\right]. \end{aligned} \tag{2.57}$$

For the case of grazing reflection, the effect of an external shear is represented mathematically by the previous logarithmic law. By the way, as it can be seen on an example of this surface shown in Fig. 19, this surface presents non-continuous zones which make not suitable a practical implementation of a grazing reflective instrument.

2.7 An instrument to invert gravitational lens effects

A way to reconstruct the real source image of a gravitationally lensed quasar, and to take full advantage of the magnifying power of the cosmic lens, is to numerically invert such lensed images using an inverse ray tracing software. To achieve this result, one should suppose a lens model. For example, to numerically invert an image like the one proposed in Figs. 15 and 16a, it is necessary to provide a point-mass lens model to the software.

Many numerical approaches have been proposed and applied on several gravitational lens systems, with good results (see for instance the example in the work of Claeskens et al. [2006] concerning RXJ1131-1231).

Another method to invert a multiply imaged source can be done with an *ad hoc* optical instrument, specifically designed for a particular source, and placed directly at the telescope.

Surdej et al. [2010] have proposed an instrumental setup to simulate the inversion, based on two successive optical lenses as the one shown at the location D in Fig. 15: the first one simulated a distant galaxy deflecting a background source; the latter one being the actual optical instrument providing the inversion. Compared to the numerical methods, this device should allow the direct imaging of fainter features and objects located close to the source, with an improved resolution. Such optical devices include refracting lenses, while other kinds of instruments could involve reflecting surfaces shaped to correct the gravitational lens effects, and specifically adapted to the model of the deflector.

We propose the following design to achieve this goal (see Fig. 20). Let us suppose that a telescope is pointed on a gravitational mirage that previous observations suggested to model with a point-mass lens distribution plus an external shear. The gravitationally lensed images "A", "B", "C", and "D" of the source are focused on the focal plane together with the deflector "G".

Here, the Lyot mask of a first coronagraph device erases the contribution of the deflector, while the lensed images follow their optical path through a converging lens, which images the field in a relayed pupil plane where an opaque Lyot stop ring provides the nulling of the residual "G" light.

An optical lens, modeled for the case of the point-mass distribution model of the observed gravitational mirage, inverts the isotropic part of the lens effects. Furthermore, the anisotropic part, represented by the external shear, is corrected by an hy-

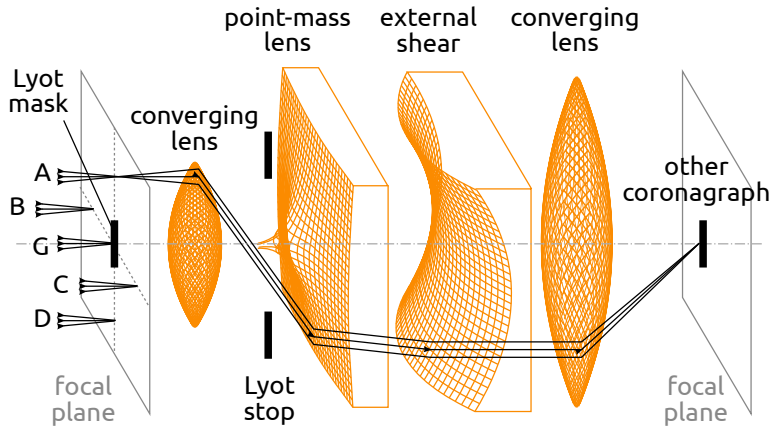

Figure 20: Simple design of an instrument capable to invert the gravitational lens effects induced by a point-mass lens plus an external shear. Four lensed images "A", "B", "C", and "D" are focused in the focal plane. We follow the path of the only "A" image. A Lyot mask erases the light of the deflector "G". A converging lens images the field in a relayed pupil plane where a Lyot stop is placed. Then an optical point-mass lens inverts the isotropic part of the mirage. Furthermore, an hyperbolic paraboloid provides the correction of the external shear and collimates the beam. Another converging lens focuses the image on a relayed focal plane. Here, a single image of the original source is retrieved, and another coronagraph masks the reconstructed source to explore the closer neighborhood of the lensed background source.

perbolic paraboloid whose orientation and slope are designed to provide the correction of the residual lens effects, collimating then into parallel beams the light rays. Another converging lens focuses the light rays on a relayed focal plane. Here, a single image of the original source is retrieved, with an improved resolution.

Other designs could involve the reflecting surfaces previously calculated. These surfaces could either be specifically designed for each gravitational mirage that we wish to study, or dynamically calculated using adaptive optics systems providing the minimization of the entropy of the recombined image in the focal plane.

other designs

Moreover, another coronagraphic system can provide a further nulling by masking the flux of the reconstructed source enhancing close fainter features in its neighborhoods. Several kinds of coronagraphs could be applied to this system. In Chap. 3 we have suggested a new concept of coronagraph with a dynamic hologram capable of removing the residual speckle halo of the source.

3 Coronagraphy with hologram

In Sect. 2.7 we proposed the design of an instrument capable to invert the gravitational lens effects produced by a macro deflector, and we proposed to couple this instrument with a coronagraph, namely an optical device designed to block the light from a distant astronomical source, such as a star or a distant quasar.

To achieve this goal, we propose a new concept of coronagraph with adaptive hologram and we present it in this chapter. We describe here the method that we proposed in a recent paper [Ricci et al., 2009], following an original idea of Labeyrie [2004]. In particular, we will present the theoretical background, while the numerical simulations of the instrument are treated in Chap. 4.

The performances of this new kind of coronagraph design are studied to overcome the limitations of the current devices: the central source flux is recuperated instead of being masked, as in the Lyot coronagraph Lyot [1939], and it is added, phase-shifted, to the coherent speckle halo, with the help of a dynamic hologram placed in the relayed pupil plane, where the Lyot stop is located..

This operation allows to remove most of the residual source light and increases the detectability of a close object, like a faint planet in the case of the utilization of the coronagraph for the direct imaging of exo-planets, or a faint feature near the central zone of a bright extragalactic source, as for example the host galaxy of a distant quasar.

Even if in our paper we focused on the first option (direct imaging of exo-planets), we suggest this concept also for other kinds of sources such as quasars and AGN, to enhance the features in the nearby surroundings (for example the host galaxy or the AGN's central zone). For that matter in this chapter we will refer to a generic bright source (the source that will be masked by the coronagraph) and to a generic faint feature located near the source (the feature that will be enhanced thanks to the nulling provided by the coronagraph).

In Sect. 3.1 we briefly mention the various existing types of coronagraphs, and we remind the functioning of the traditional Lyot device in Sect. 3.2. Sect. 3.3 describes two kinds of optical

design presented in our works (Sect. 3.3.1 and 3.3.2). A complete explanation of the operation implemented by such a hologram in a Lyot coronagraph is given in Sect. 3.4. In Sect. 3.5 we discuss the adaptive hologram technology, and finally in Sect. 3.6 we summarize the results.

3.1 State of the art

Since the pioneer solar coronagraph developed by Lyot [1939] in the first half of the XXth century to study the solar corona, the coronagraphic techniques have been particularly developed in recent years, significantly improving its attenuation gain, which was limited to about 10 000.

The so-called "Lyot coronagraph" (see Fig. 21) was improved by replacing the opaque mask with phase masks [Roddier and Roddier, 1997, Riaud et al., 2001], which attenuated the background level below 10^{-7} [Riaud et al., 2003]. The stronger chromatic dependence of phase masks was mitigated with devices such as the achromatic annular groove phase mask [Mawet et al., 2007].

Another way to improve the existing coronagraphs and erase the rings of the PSF (Point Spread Function) of the source is to apodize the pupil, for example using prolate functions [Aime et al., 2002, Soummer et al., 2003]. Unfortunately, a large fraction of the light is absorbed by the apodization mask. The loss is avoided with an apodizing device [Guyon, 2003, Guyon et al., 2007] using a pair of distorted mirrors to modify the light distribution across the pupil. With this loss-less achromatic apodization, features or objects as faint as 10^{-10} can in principle be directly imaged.

However, in practice, even a theoretically perfect coronagraph is greatly affected by the residual bumpiness of the incoming source wavefront, caused by imperfect mirror polishing or residual atmospheric turbulence, which cannot be perfectly corrected by adaptive optics. The residual halo of the source light in the image typically exhibits a speckle pattern at a relative level much higher than 10^{-10}.

Maréchal's formula Roddier [1981] shows that, concerning the specific case of the direct detection of an exo-planet that is 10^9 times weaker than its parent star with a 10m telescope operating at 1µm, the RMS (Root Mean Square) wavefront error among 10cm patches, such as obtained by 10 000 actuators, should remain below 0.5nm.

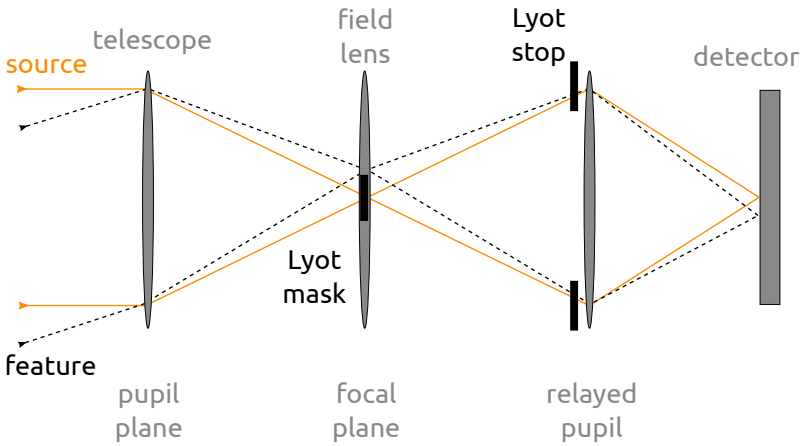

Figure 21: Classical Lyot coronagraph: the light of a bright source (solid) and of a faint close feature (dotted) are focused by the telescope at different locations in the focal plane. The Lyot mask attenuates the light of the object without suppressing the close off axis feature. A field lens re-images the objects in a relayed pupil plane. The Lyot stop blocks the diffracted residual light. A convergent lens re-images the field on the detector.

Since such an accuracy is not achievable with the present figuring techniques, one method to remove the residues is to add stages of adaptive elements. Several adaptive devices proposed in the literature [Codona and Angel, 2004, Labeyrie, 2004, Putnam et al., 2006] use the following interesting property: if the source is unresolved, as in the case of an AGN or of a sufficently distant star, the light of the speckle halo is coherent with that of the central source, usually absorbed by the Lyot mask.

It is in principle possible to retrieve this light and use it to create destructive interference with the speckle halo. This solution improves the detectability of the faint non-coherent exo-planet, with a second step of adaptive optics.

3.2 Traditional Lyot coronagraph

In a traditional coronagraph device (see Fig. 21), the light of a bright source and a faint close feature (for example the Sun and the solar corona a distant quasar and its host galaxy; or a star and its companion) is focused by the telescope in different locations of the focal plane, where an opaque mask is placed. A

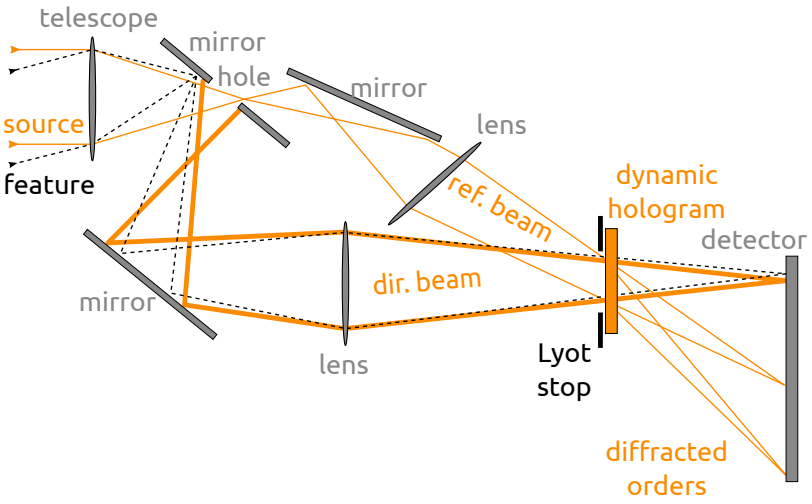

Figure 22: Implementation of a hologram in the classical Lyot coronagraph. The opaque mask is replaced by a flat mirror with a central hole. The light of the source is retrieved through a small hole (typically with the size of the Airy peak) to create a reference beam. The light out of the Airy peak of the source and the light of the faint feature do not pass through the hole (direct beam). The direct beam intersects the reference beam in the pupil plane, where the Lyot stop is placed in front of a dynamic hologram (described in Sect 3.4).

circular mask, called "Lyot mask", has a typical size designed to block the light of the object without suppressing the close feature.

A lens in the focal plane provides the re-imaging of the field in a relayed pupil plane. Here, the residual light of the source is diffracted into a bright ring. An annular opaque mask, called "Lyot stop", attenuates this light improving the nulling of the source. Finally, a convergent lens re-images the field in its focal plane, where the detector (for example a CCD camera) is placed.

However, the Lyot coronagraph is not perfect and the extinction can not be much better than 10 000 even when using a perfect optics (without bumps on the mirrors).

3.3 Introduction of an adaptive hologram

As explained in our papers [Ricci et al., 2009, 2010a], the central part of the beam can be retrieved instead of being absorbed. We present two different designs that can be adopted to reach this

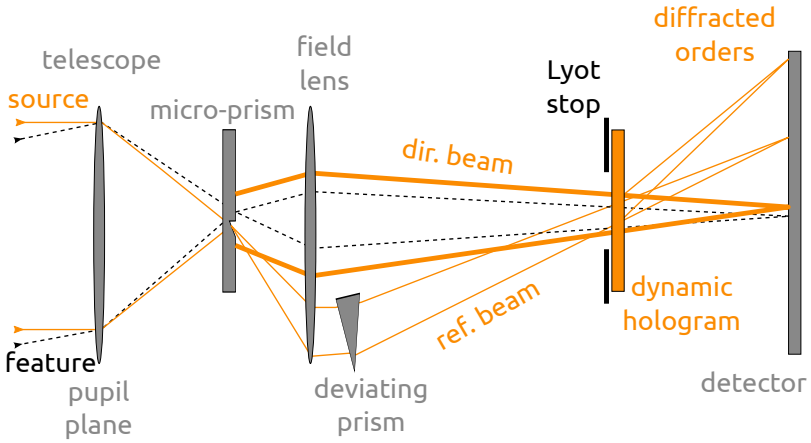

Figure 23: Alternative design of an adaptive hologram in the coronagraph, with the introduction of a micro-prism (zoomed in Fig. 24). The micro-prism separates the source's geometric beam (reference beam), and preserves the outer diffracted rings and speckles plus the fainter features (direct beam). A larger deviating prism deflects the reference beam in such a way that it intersects the direct beam in the relayed pupil image, where the Lyot stop is placed in front of a dynamic hologram (described in Sect 3.4).

goal: a flat mirror with a central hole (Sect. 3.3.1) and a micro-prism deflector (Sect. 3.3.2).

3.3.1 Design with a flat mirror with a central hole

In this implementation (see Fig. 22), the opaque mask is replaced by a flat mirror with a central hole, in order to retrieve the central light of the source. This small hole has the typical size of the Airy peak, acting as a spatial filter. It allows to create a flat wavefront. We refer to this collected light as to the "reference beam".

Analogously, we refer to the external part of the light of the source (which does not pass through the hole) as to the "direct beam". The direct beam proceeds its path together with the light of the unmasked closer feature (for example the light of an exo-planet orbiting around a star whose light was masked). The reference beam is deflected in such a way that it intersects the direct beam in the pupil plane, where the Lyot stop is placed.

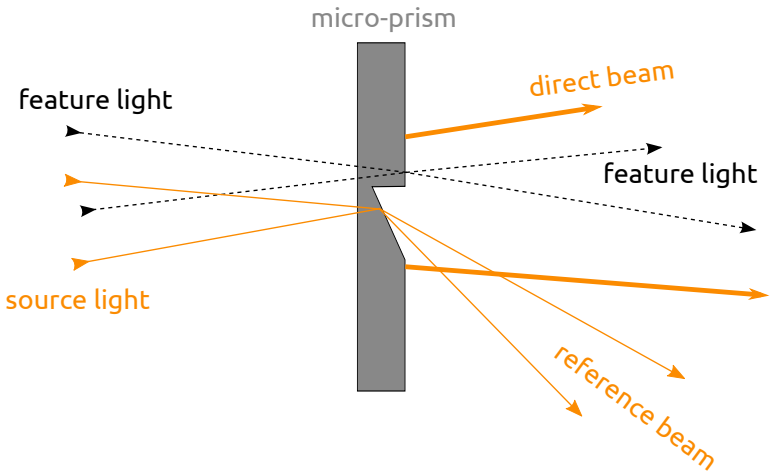

Figure 24: Detail of the micro-prism. The micro-prism design can be adapted to match a desired size for specific observations.

3.3.2 Design with a deviating micro-prism

As shown in Fig. 23 and in detail in Fig. 24, the focal occulter is replaced by a deviating micro-prism which separates the source's geometric beam, that we called "reference beam", while preserving the outer diffracted rings and speckles, together with the images of the fainter features, forming the "direct beam".

The micro-prism size can vary between that of the Airy peak and a size of several rings, such as a Lyot mask. A larger deviating prism deflects the reference beam in such a way that it intersects the direct beam in the relayed pupil image where the Lyot stop is located.

3.4 Functioning

Regardless of the adopted design (central hole in a flat mirror or deviating micro-prism), a dynamic hologram is located just behind the Lyot stop. The functioning of the proposed dynamic hologram is basically summarized as follows:

recording the hologram

- The reference beam and the direct beam add in a coherent way, creating fringes in the speckles of the hologram. This process is called "recording the hologram". The fringes of the recorded hologram act like a grating, and diffract an incoming light beam in several orders. These orders become

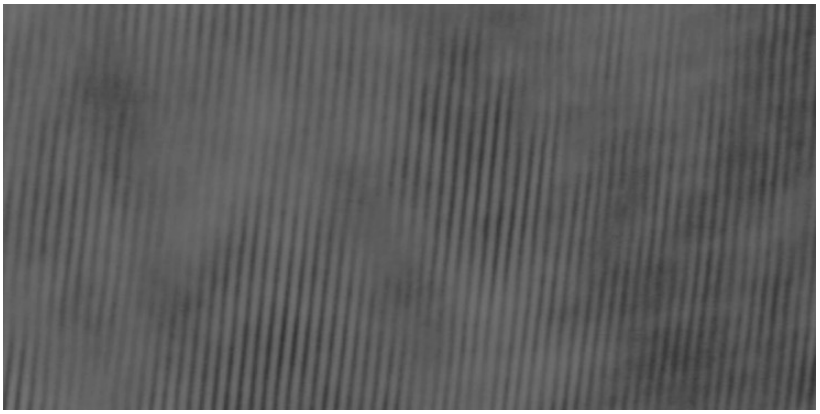

Figure 25: Picture of the fringes generated by a hologram in a laboratory test. The details about these tests are given in Chap. 4.

focused in the focal plane where a detector is placed (see again Figs. 22 and 23).

- If we illuminate the recorded hologram with the reference beam only, a reconstructed image of the source's speckles appears on the detector, together with other diffracted orders. Using a reference beam phase-shifted by π (or a negative hologram), we obtain the same image phase-shifted by π.

destructive interference between direct and π-shifted reference beam

- Our purpose is to create an interference between the direct beam and the reference beam phase-shifted by π. Thanks to this phase shifting, the order 0 of the direct beam adds destructively with the order $+1$ of the phase-shifted reference beam, containing the reconstructed image of the star's speckles, thus nulling the residual speckles of the source.

- The faint feature's light, being incoherent with respect to the reference beam, is not reconstructed by the hologram, and is thus not erased in the focal plane.

- Once the field is recorded by the detector, another cycle of correction can start again with a new recording of the hologram.

In the final image, the reference beam is diffracted by the hologram into several orders. We call these orders ($-1\mathrm{ref}$, $0\mathrm{ref}$, and $+1\mathrm{ref}$). The order "$+1\mathrm{ref}$" is a reconstruction of the speckled wavefront, phase-shifted by π. The reference beam may intersect the direct beam at an angle of several degrees. We note ψ_d and $I_d = |\psi_d|^2$ the complex amplitude of the direct beam and its intensity at a point P in the hologram's plane (see Fig. 22 or

Fig. 23), while ψ_r and $I_r = |\psi_r|^2$ are the corresponding values for the reference beam.

As we explained above, the interference between the reference beam and the direct beam creates fringes in the speckles of the hologram. Fig. 25 shows a picture of the fringes generated by a hologram in a laboratory test carried out in Calern (France) by the team of Antoine Labeyrie. The fringes behave like a grating, which diffracts several orders becoming focused in the focal plane. (see Fig. 26).

Hervé Le Coroller proposed to study the role of the diffraction orders in the detection of a faint object. He has given an analytical description (Eqs. 3.1–3.4).

We performed the numerical simulations [Ricci et al., 2009] and we computed, for the first time, the performances of the hologram in presence of mirror imperfections, photon noise and transmission noise (see Chap. 4).

The complex amplitude resulting from the interference of the two beams at point P in the pupil is

$$\psi = \psi_d + \psi_r, \tag{3.1}$$

while the intensity I is

$$\begin{aligned} I &= \psi\psi^* \\ &= (\psi_d + \psi_r)(\psi_d^* + \psi_r^*) \\ &= I_r + \psi_d\psi_r^* + \psi_d^*\psi_r + I_d \\ &= I_r \left[1 + \frac{\psi_r^*\psi_d}{I_r} + \frac{\psi_r\psi_d^*}{I_r} + \frac{I_d}{I_r}\right]. \end{aligned} \tag{3.2}$$

The hologram has an amplitude transmittance $\tau = I^{\gamma/2}$, where the parameter γ is the classical intensity contrast in photographic materials [Perez, 2000]. By illuminating the recorded hologram with the reference beam only, a reconstructed image of the speckles of the bright source, noted $+1ref$ on Fig. 26, appears on the detector. Using a reference beam phase-shifted by π, we obtain the same image phase-shifted by π if the hologram is a positive print. Note that in the article of Labeyrie and Le Coroller [2004] the π shift was obtained with a negative hologram, which is equivalent. Finally, the order 0 of the direct beam (that we call 0s) adds destructively with the order $+1ref$, thus nulling the residual speckles of the source.

The feature's light, being incoherent with the reference beam and little affected by the micro-prism, is not reconstructed by the hologram, and therefore escapes the nulling. If we illuminate the

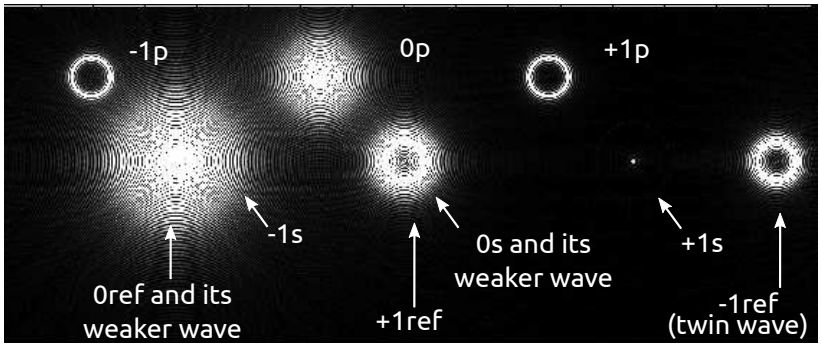

Figure 26: Simulation of an imaged system composed of a bright unresolved source (like a quasar or a star) and a faint companion (like a feature in the quasar's host galaxy, or an exo-planet orbiting around the parent star). The system is imaged by means of a Lyot coronagraph equipped with an adaptive hologram. Here, for clarity, the faint feature is particularly bright and far from the bright source. The diffracted orders -1, 0 and $+1$ of the feature are noted respectively $-1p$, $0p$ and $+1p$. The orders -1, 0 and $+1$ of the source are noted respectively $-1s$, $0s$ and $+1s$. The order $+1s$ looks faint in this figure because it is fainter than the direct flux of the source ($0s$) and the reference beam ($0ref$). The orders -1 (twin wave), 0 and $+1$ of the reference beam are noted respectively $-1ref$, $0ref$ and $+1ref$. The nulling of the source is caused by the destructive interference of its order 0 ($0s$) and the order $+1$ of the reference beam ($+1ref$), both superposed on the detector. Here, no π phase shift is introduced in the reference beam, so as to show the diffracted orders $+1ref$, and $0s$. The "twin wave" falls out of the detector at left, but here spuriously appears at right due to aliasing. This effect is caused by the moderate sampling which we had to use in the hologram.

recorded hologram with the reference beam, now phase-shifted by π, the transmitted complex amplitude becomes:

$$\psi = \tau\left(\psi_d + \psi_r e^{i\pi}\right) = \tau\left(\psi_d - \psi_r\right). \tag{3.3}$$

If $\gamma = 2$, the usual value considered optimal in holographic practice, the product of both factors having respectively four and two terms leads to eight terms. As expected, since the reconstructed direct wave is shifted by π with respect to the transmitted direct wave, the corresponding pair of terms cancels. Another pair of terms also cancels for a related reason. The expression thus simplified is:

$$\begin{aligned}\psi &= (I_r\psi_d - I_r\psi_d) - I_r\psi_r + I_d\psi_d - \psi_r^2\psi_d^* + \psi_r^*\psi_d^2 \\ &= -I_r\psi_r + I_d\psi_d - \psi_r^2\psi_d^* + \psi_r^*\psi_d^2.\end{aligned} \tag{3.4}$$

The remaining terms of Eq. 3.4 represent various orders which are diffracted by the hologram, locally behaving like a diffraction grating, and becoming separated on the camera. Some of them widely spread their light on the camera, thereby degrading the visibility of planet peaks. In the following, we discuss the impact of each term of Eq. 3.4 on the detection of the feature, always referring to Fig. 26 for the labels of the orders.

transmitted reference wave

- The term $I_r\psi_r$ is the transmitted reference wave, producing an intense but sharp focus on the camera (order 0 of the reference beam, that we label as 0_{ref}). The apodization of the reference beam causes an improving in the nulling depth since its Airy rings in its zero-order image pattern become attenuated, and thus contaminate less the image of the faint feature. Such apodization occurs naturally if the micro-prism separator (see Fig. 24) selects the central Airy peak down to its first dark ring. Additional spatial filtering can be achieved at the micro-prism if needed.

weaker wave

- The term $I_d\psi_d$ describes a wave that propagates close to the direct source's residue wave ($I_r\psi_d$), nulled by the hologram, but with attenuated and spatially modulated intensity. We refer to this term as to the "weaker wave". The modulation causes some diffractive spreading on the camera, contaminating the image of the close feature (the exoplanet or the host galaxy of the quasar). This is mitigated by using a very intense reference beam, relative to the direct beam, so that $I_d\psi_d \ll I_r\psi_d$. The intensity thus achievable, as limited by the energy content of the Airy peak in the focal plane of the telescope, defines the maximal possible gain with a hologram. This suggests that the maximum nulling achievable is:

$$G \approx \frac{\sum_p I_r^2}{\sum_p I_d^2}, \tag{3.5}$$

  where the $\sum_p$ summing extends to all points of the pupil plane that are not blocked by the Lyot stop. The numerical simulations carried on in Chap. 4 support this estimate.

- The term $\psi_r^*\psi_d^2$ is the order $+1$ of the direct beam ($+1$s in Fig. 26);

twin wave

- The term $\psi_r^2\psi_d^*$ is a wave similar to the direct beam (direct stellar residue wave), since its complex amplitude is proportional to the conjugate of ψ_d. This last wave is termed the "twin wave" (order -1 of the reference beam, labeled

as $-1ref$). Its contamination is discussed in Sect. 4.1, while facing the numerical simulations.

The order -1 of the direct beam ($-1s$) cancels with the wave $I_d\psi_r$ that propagates close to the order 0 of the reference beam.

3.5 Adaptive hologram technology

A dynamic hologram (or adaptive hologram) works both as a wavefront sensor and an actuator array, thus behaving like the feedback loop of conventional adaptive optics.

In the absence of re-writable holographic materials having enough light sensitivity and response speed, the sensing and playing functions of the hologram can also be achieved by two separate components: a camera and a Spatial Light Modulator (SLM). To detect and process the light beams simultaneously, the camera can be fed by a beam splitter while the SLM is located in the relayed pupil, that is to say at the hologram position indicated in Fig. 22.

Of interest are EM-CCD camera chips, incorporating electron multiplication which makes them nearly photon-limited at low light levels; and SLMs such as those using a liquid crystal film on a silicon matrix, currently available with 1280×720 pixels[1]. Such existing components are readily usable to test a holographic coronagraph on a laboratory bench and then on a telescope, particularly at red and near infrared wavelengths where the lifetime of speckles is longer. Inserting a computer or dedicated fast processor in the video connection is useful to adjust the π phase shift, the γ contrast, and the other parameters of the printed hologram. Much slower speeds suffice in space, where an artificial star such as a remote laser source can in principle be used to record the hologram.

With these existing components, a typical observing sequence involves the near simultaneous printing of the hologram with the live recorded pattern. Laboratory tests are required.

3.6 Results

We discussed the implementation of the original design of an apodized Lyot coronagraph by suggesting the introduction of a dynamic hologram in the optical scheme. We also proposed two designs to implement this concept (see Figs. 22 and 23). A

1 See www.cambridgecorrelators.com/products.html

theoretical approach shows that it is possible in principle to cancel the residual speckle halo of a bright source improving the enhancement of a close faint feature.

We realized numerical simulations to prove the validity of this concept, as well as a study concerning a practical implementation in laboratory tests (see Chap. 4).

4 Coronagraph simulations

In this chapter we go deeply into the simulations of the new concept of coronagraph with adaptive hologram introduced in Chap. 3. We recall the details of the results, obtained with numerical simulations, that we presented in a recent paper [Ricci et al., 2009] and subsequently refined with a large number of tests to study the possibilities for a practical implementation [Ricci et al., 2010a,b].

The intent of the simulations in the mentioned works was to reproduce the angular separation between a star and an Earth-like planet located at 1AU from its parent star, at 11pc from us (like the Sun and the Earth as seen from the planet Gliese 436b), and observed with a 6.5m telescope. Nevertheless, the results in terms of nulling depth are valid regardless of the source and of the faint feature, and can be applied to unresolved extragalactic objects as quasars and AGN. For that reason we will refer, as in Chap. 3, to a more general concept of bright source and close faint feature.

Preliminary laboratory tests to implement this kind of device are ongoing in the laboratories of Calern (France).

In Sect. 4.1 we describe the simulation parameters and their optimization; in Sect. 4.2 we introduce several configurations of coronagraphs, to compare our implementation with the classical solutions. We show the numerical results and we discuss the gain obtained under different conditions: ideal ones (Sect. 4.2.1); with the introduction of static wavefront bumpiness as in the case of mirror imperfections (Sect. 4.2.2); with the addition of photon noise (Sect. 4.2.3) and with transmission noise on the hologram (Sect. 4.2.4). In Sect. 4.3 we summarize the results of all these steps with the aim of comparing the performances in the separate cases. Sect. 4.4 is particularly focused on the possibilities of a practical implementation in the case of exo-planet imaging, dealing with the degrading effect of a star which is partially resolved. We discuss its possible mitigation, and the design of an achromatized version. Finally, in Sect. 4.5 we report the results.

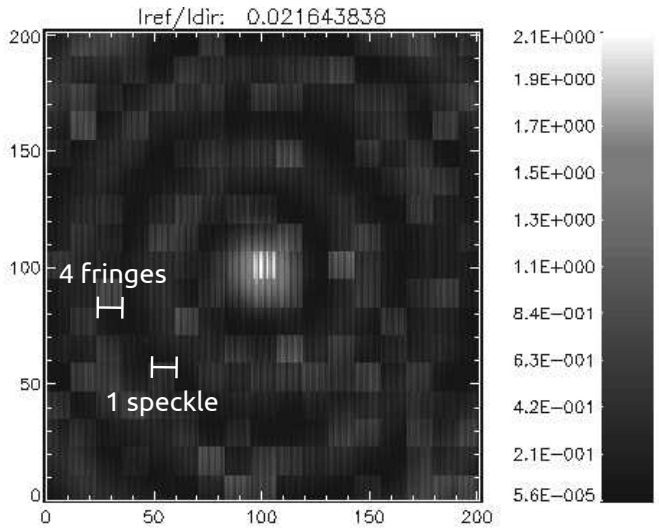

Figure 27: Numerical simulation of the central part of a hologram recorded in intensity in the pupil plane with a reference beam at 65° incidence. For a contrasted display here, the wave bumpiness is adjusted at the $\lambda/40$ level, at $\lambda = 550$nm. The reference beam intensity is much reduced, to show both the speckles (simulated as squares for simplicity) and the finer fringes within them. There are approximately four fringes per speckle, and four pixels per fringe period. The total pixel count is 1599×1599, only 200×200 of which are displayed here.

4.1 Optimization and numerical simulations

In our simulations there is no distinction between the design with the central hole (see Sect. 3.3.1) or the design with the micro-prism (see Sect. 3.3.2). We will refer to the latter one for simplicity.

We adjusted the size of the micro-prism to that of the fourth dark ring in the Airy pattern (so that its diameter amounts in our simulations to $8\lambda f/D$ or 13.5µm in visible light at $f/3$, where λ is the wavelength, f is the focal length and D is the diameter of the pupil), and the faint feature was placed in the fifth ring. This reproduces the angular separation between a star and an exo-earth located at 11pc from an observer provided with a 6.5m telescope.

In order to simplify the computations, we coarsely simulated the mirror bumpiness or turbulence with a square grid of bumps with random amplitudes, and we verified that the shape of the phase cells on the mirror do not affect our results.

For minimal calculation noise, which represents a possible problem given the high dynamic range considered, while keeping a reasonable computation time and usage of our 2GB RAM memory, we used 1599×1599 pixel arrays, with the pupil spanning 402 pixels.

The bumpiness of the incoming wavefront is converted into intensity speckles having random phases in the relayed pupil, where the hologram is placed, in response to the occultation of the Airy peak in the focal plane. In the pupil plane, the interference with the oblique reference beam generates the finer fringes seen within each speckle (see Fig. 27). For a good sampling in the hologram, at least four pixels are needed per fringe period, and simultaneously at least four fringes per speckle. A larger value of the angle θ between the direct and reference beams increases the number of fringes per speckle, but decreases the number of pixels per fringe. It also increases the spacing of the diffracted orders in the focal plane, which improves the contrast of the feature's peak. In our simulation, we used about four pixels per fringe for an angle $\theta = 65°$, as marked in Fig. 27. This corresponds to at least four fringes per speckle, if the typical scale of the bumpiness at the entrance pupil is larger than 12×12 pixels.

For optimal performances, it is important to adjust the parameters described below.

- In accordance with the classical theory of holograms, the reference beam must be substantially more intense for a faithful wavefront reconstruction by the hologram, as apparent in the second term of Eq. 3.4. In practice, here, the hologram's nulling gain is proportional to the square intensity ratio (see Eq. 3.5), i.e. $\approx 10^3$ in our numerical simulations with wavefront bumpiness imperfections at $\lambda/20$ ($\lambda = 550$nm). This ratio is limited in practice by the energy content of the Airy peak, diverted by the micro-prism to form the reference beam. The size of the micro-prism or attached filtering aperture, possibly apodized, should be optimized for maximal light collection while keeping a flat wavefront. We found that an aperture sized like the Airy peak is optimal in this respect and also to minimize the inner working angle.

  intensity ratio of reference and direct beams

- As in conventional Lyot coronagraphs, the size of the Lyot stop was adjusted to block the bright edge of the pupil image.

  size of the Lyot stop

contrast and γ parameter

- Based on Eq. 3.4, we conclude that an optimal value for γ is 2 using a positive print, with a phase shifter then introduced in the reference beam during read-out, and -2 if it is negative.

contamination by the twin wave

- The twin wave is described by the term $\psi_r^2\psi_d^*$ in Eq. 3.4. It gives a focal image identical to the direct wave, but shifted, and non-overlapping if the reference beam angle, with respect to the direct beam, exceeds the apparent pupil size. In our simulations, however, the pixel sampling of the hologram was insufficient to properly generate the twin wave, causing it to be aliased by the Fourier transform algorithm, and to appear in the final image at an incorrect "folded" location which contaminated the feature image (see Fig. 26 in Chap. 3). The aliasing effect causes the twin wave to be nearer to the 0 order of the direct beam (and then to disturb the flux of the faint feature) than if it was not aliased. In order to remove such numerical effects, we have simulated a suppressed twin wave by removing the corresponding term, in complex amplitude, in the numerical calculation, and we found an improved detection sensitivity, part of which may result from the removed aliasing effect.

In our recent paper [Ricci et al., 2009] we did not study the physical effect of the twin wave, but we know that the solution is in between the case including the twin wave (C in Table. 1) and the case where its effect is analytically subtracted (D in Table. 1). More realistic simulations of the twin wave's effect are desirable in further works, and this may require non-FFT calculation methods [Soummer et al., 2007].

Nevertheless, twin waves can be eliminated by using a thick hologram, also known as a Lippmann-Bragg hologram, in order to work in the case D of Table. 1. These have stratified nodal planes, rather than fringes, which selectively reflect a single first-order wave. Then, the hologram works like a "blazed grating", sending most light in the reconstructed image (order $+1_{ref}$).

4.2 Gain evaluation

Using the optimizations listed in Sect. 4.1, we were able to reproduce a wide range of coronagraph configurations, in order to compare their detection limit versus the flux ratio between the bright source and faint feature (F_s/F_p).

A Classical Lyot coronagraph: it is the basic traditional device described in Sect. 3.2;

B Apodized Lyot coronagraph: we simulate a traditional device including an apodized pupil to concentrate the light in the Airy peak and then to improve the nulling effect of the classical Lyot mask;

C Apodized Lyot coronagraph provided with a hologram and an apodized reference beam: we introduce the hologram in the optical scheme of the apodized Lyot coronagraph (B);

D Apodized Lyot coronagraph with hologram, apodized reference beam, and subtracted twin wave: in these simulations we improve the performances of the C device by analytically subtracting the effect of the twin wave.

The performance is evaluated under four different conditions:

- ideal ones (no mirror imperfections and absence of photon noise);
- with the introduction of mirror imperfections (also called mirror bumpiness);
- with photon noise in addition to the mirror imperfections,
- with transmission noise in order to study a practical implementation.

These steps are treated in the following subsections, and summarized in Table 1 for what concerns the two first conditions. The speckle noise N was coarsely evaluated in the images using the following equation:

$$N = \frac{\bar{I}_p - \bar{I}_s}{\sigma_s}, \tag{4.1}$$

where $\bar{I}_p$ is the mean peak intensity at the position of the faint feature; $\bar{I}_s$ is the mean background intensity of the speckles near the feature position, and σ_s is the corresponding root mean square fluctuation.

4.2.1 Gain with a perfect mirror

The first results are obtained under the assumption of perfect conditions, in the absence of mirror bumpiness and photon noise.

For the classical Lyot coronagraph (A), we obtain a detection limit in flux ratio of $F_s/F_p = 10^{3.2}$. In the case of the apodized

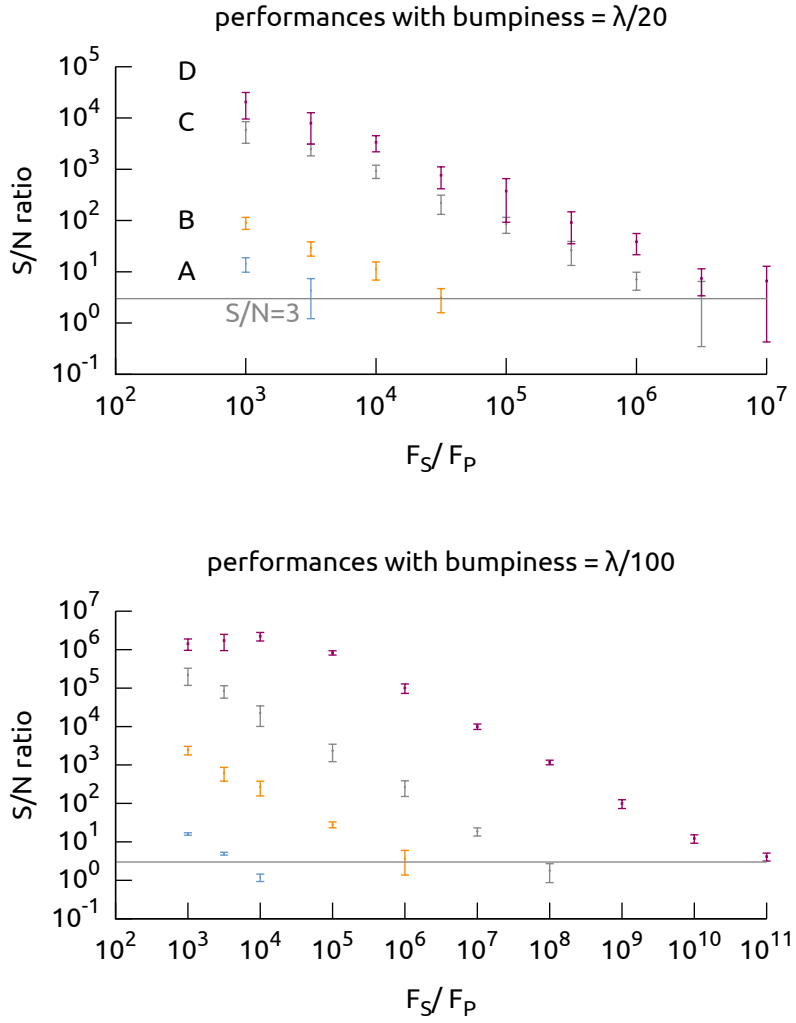

Figure 28: Simulations of several kinds of coronagraphic devices: classical Lyot coronagraph (A); apodized Lyot coronagraph (B), apodized Lyot coronagraph with the introduction of the hologram (C); apodized Lyot coronagraph with the introduction of the hologram and after subtraction of the twin wave (D). The figures show the signal-to-noise ratio (S/N) as a function of the ratio between the flux of the bright source (F_S) and the flux of the faint feature (F_P) for the cases of mirror bumpiness of $\lambda/20$ (upper figure) and $\lambda/100$ (lower figure). We find a value of $\sum I_r^2 / \sum I_d^2 \approx 10^3$ at $\lambda/20$ and $\approx 10^6$ at $\lambda/100$ for the solutions providing the hologram.

Table 1: Detection limit of the flux ratio F_s/F_p for the different configurations mentioned in Sect. 4.2 and in the absence of photon noise: perfect conditions, λ/100, and λ/20 wavefront bumpiness.

Conditions	A	B	C	D
Perfect conditions	$10^{3.2}$	$10^{11.0}$	$10^{11.0}$	$10^{11.0}$
λ/100	$10^{3.5}$	$10^{5.7}$	$10^{7.6}$	$10^{10.8}$
λ/20	$10^{3.5}$	$10^{4.5}$	$10^{6.2}$	$10^{7.9}$

Lyot coronagraph (B), the detection limit is increased to $10^{11.0}$. Introducing the hologram in the optical scheme with the apodization of the reference beam (C), the limit is $10^{11.0}$, and the same result is obtained after subtraction of the twin wave (D). Our simulations appear to be limited to this range by numerical noise. The hologram becomes most valuable in the presence of mirror imperfections.

4.2.2 Gain with a bumpy mirror

In order to test the performances of the simulated devices under more realistic conditions, we introduced a random static bumpiness on the incoming wavefront, which represents a mirror polishing imperfection, with a λ/20 peak-to-valley amplitude. We also performed simulations at λ/100, a situation intermediate between perfect conditions and the bumpiness with a λ/20 amplitude. The results are shown in two graphics in Fig. 28, while Figs. 29 and 30 show simulated images where it is possible to visually appreciate the contrast of the faint feature with respect to the speckle background.

As it can be seen in Table 1, the detection limit in flux ratio with a λ/20 wavefront bumpiness is $F_s/F_p = 10^{3.5}$ with the classical Lyot coronagraph (A); $10^{4.5}$ with the apodized Lyot coronagraph (B); $10^{6.2}$ with the hologram and apodized reference beam (C); and $10^{7.9}$ after subtracting the twin wave (D). At λ/100 we find $F_s/F_p = 10^{3.5}$ with the classical Lyot (A); $10^{5.7}$ with the apodized solution (B); $10^{7.6}$ with the hologram and apodized reference beam (C); and $10^{10.8}$ after subtracting the twin wave (D). The results in this latter case are in between those obtained under ideal conditions and those obtained at λ/20.

The results with mirror imperfections reveal the large gain then obtained with the introduction of the hologram, especially when subtracting the twin wave. Indeed, with a λ/20 wavefront bumpiness, it is not possible to detect the faint feature (as for

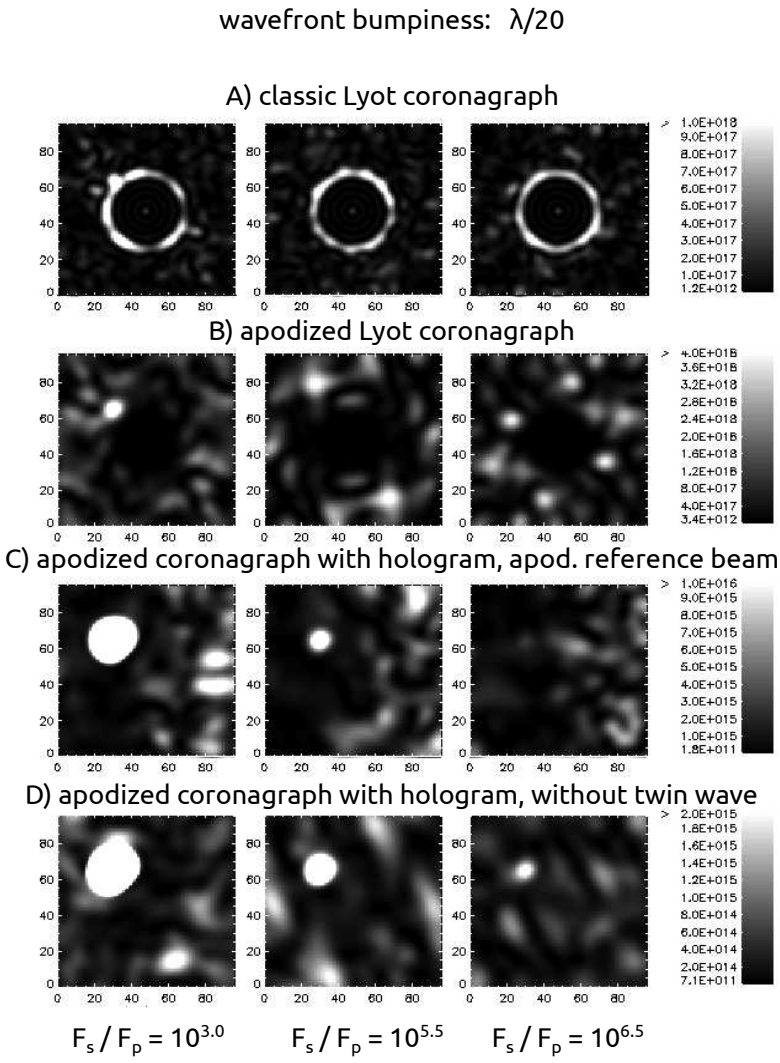

Figure 29: The four rows show simulated images with the A, B, C and D coronagraph types mentioned in Sect. 4.2. The ratio between the flux of the source F_S and the flux of the faint feature F_P is $10^{3.0}$ in the left column, $10^{5.5}$ in the central column, and $10^{6.5}$ in the right column. The wavefront bumpiness is $\lambda/20$ as described in Sect. 4.2.2. The intensity scales at right indicate the number of photons per pixel, for a source with magnitude $m_V = 7$, a telescope diameter $D = 6.5$m, $\lambda = 550$nm and spectral bandwidth $\Delta\lambda = 10$nm. The exposure time is 60s to create the hologram, then 60s more with the science camera.

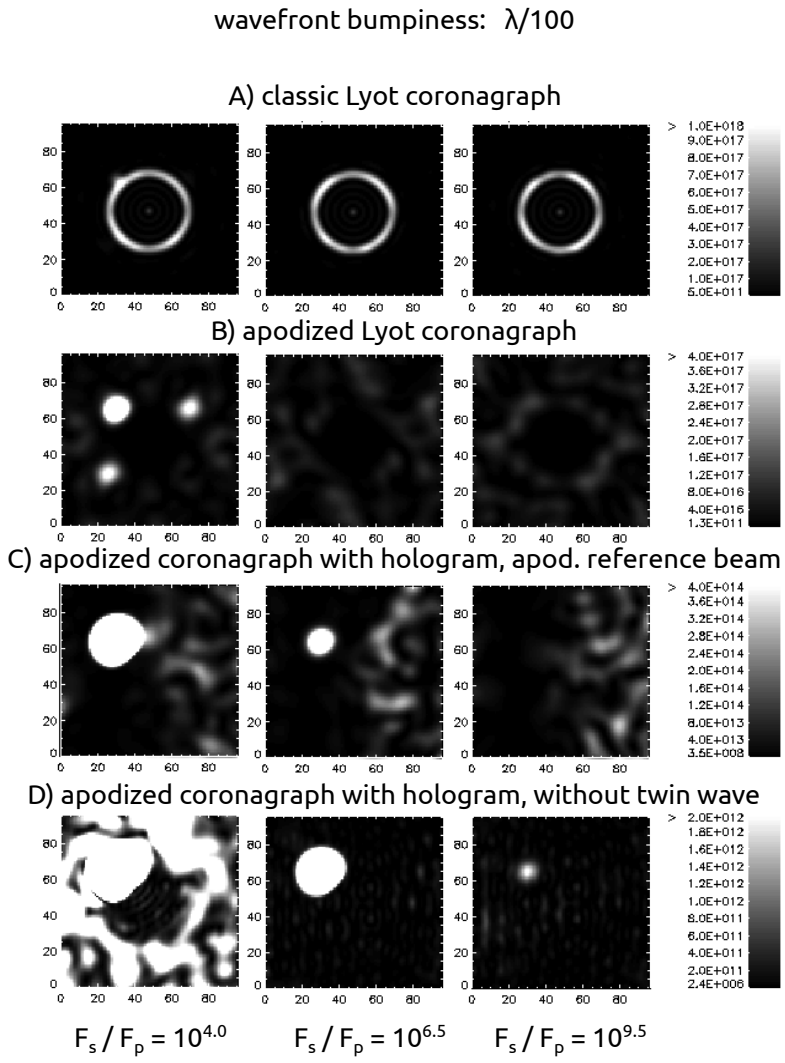

Figure 30: The four rows show simulated images with the A, B, C and D coronagraph types mentioned in Sect. 4.2. The ratio between the flux of the source F_S and the flux of the faint feature F_P is $10^{4.0}$ in the left column, $10^{6.5}$ in the central column, and $10^{9.5}$ in the right column. The wavefront bumpiness is $\lambda/100$ as described in Sect. 4.2.2. The intensity scales at right indicate the number of photons per pixel, for a source with magnitude $m_V = 7$, a telescope diameter $D = 6.5$m, at $\lambda = 550$nm and spectral bandwidth $\Delta\lambda = 10$nm. The exposure time is 60s to create the hologram, then 60s more with the science camera.

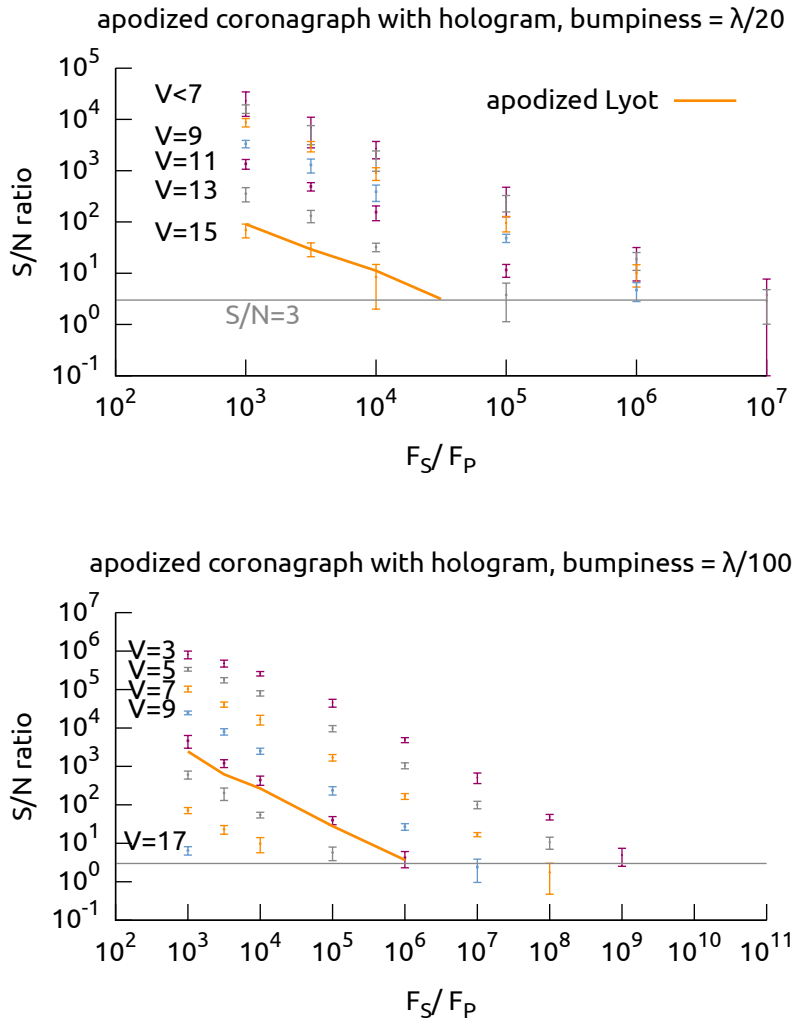

Figure 31: Simulation of an apodized Lyot coronagraph equipped with a dynamic hologram and after subtraction of the twin wave (case "D" in Fig. 30 for different V magnitudes, see legend, in presence of photon noise both on the hologram and on the CCD device. The performances of the apodized Lyot coronagraph without hologram, at $m_V = 7$ are also plotted (orange line). The figures show the S/N as a function of the ratio between the flux of the bright source F_S and the flux of the faint feature F_P for the cases of mirror bumpiness of $\lambda/20$ (upper figure) and $\lambda/100$ (lower figure), with a JWST-like space telescope and with an exposure time of 60s.

example an exo-planet) with an apodized Lyot coronagraph if the ratio F_s/F_p is larger than $10^{4.5}$ (see Fig. 29). This limit is pushed to $10^{7.9}$ using the same kind of coronagraph equipped with a hologram and after subtraction of the twin wave. The detection limit is increased by a factor $10^{3.4}$. This number is about equal to the intensity ratio, as predicted by the analytical estimation (see Eq. 3.5).

4.2.3 Gain with a bumpy mirror and photon noise

After having tested the coronagraphs under perfect conditions and in the presence of mirror bumpiness, we added photon noise. Unless the hologram is recorded with infinitely many photons, its recorded fringes are noisy, and this degrades the nulling depth on the camera image, which degrades the visibility of the feature's peak.

It can be shown that the sensitivity limitation, regarding the detection of faint features, is then ultimately the same as with a conventional adaptive optics system feeding a perfect coronagraph or apodizer, where the nulling depth is similarly limited by the number of photons detected by the wavefront sensor.

The calculation given in the former case [Labeyrie, 2004] indeed also applies to the latter case: N_p photons, detected either by a hologram or a conventional wavefront sensor, limit the achievable peak/halo nulling depth G to $G_{max} = N_p$.

Hybrid forms using both conventional adaptive optics for the correction of the wavefront and a dynamic hologram for a finer correction are also possible. They can use a single wave sensor such as a camera located in the hologram plane and serving as the holographic detector. It can then be fed to an adaptive holographic plate, incorporating its own actuators (working in transmission), in the form of the fringe patterns acting as tiny gratings within each of its speckles.

frozen photon noise (fringes-"actuator" noise in the control signal), and live photon noise

Like ordinary actuators in a servo loop, their performance is degraded by photon noise in the control signals, that is to say the recorded fringes with their "frozen" photon noise. During the observation, after the hologram recording stage, the more usual form of photon noise is also present in the recorded image and further contributes to degrade the detectability of the feature's peak.

In our simulations, we assumed that exposures of equal duration served for the two phases of hologram recording and observation. This may be optimal if the hologram is recorded with the same star which is subsequently observed.

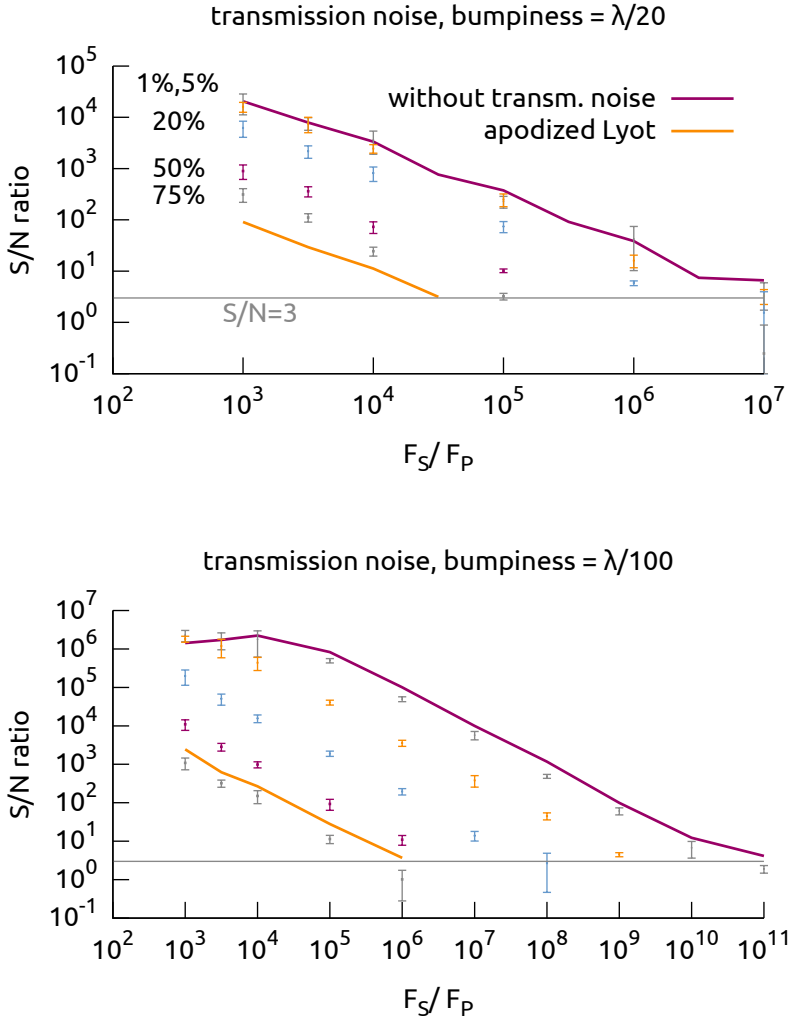

Figure 32: Simulations of an apodized Lyot coronagraph equipped with a dynamic hologram and after the subtraction of the twin wave (D). The computation does not take into account the photon noise and shows the results for different amplitudes of the transmission noise on the hologram. The figures show the S/N as a function of the ratio between the flux of the bright source F_S and the flux of the faint feature F_P for the cases of mirror bumpiness of λ/20 (upper figure) and λ/100 (lower figure).

If, however, a brighter reference star or a laser artificial star is used to record the hologram, the results given below may be considered as a lower limit since the photon noise of the hologram becomes attenuated in this latter case. Poisson-distributed photon noise was generated in the hologram and the final image using a standard IDL routine, based on C code [Press et al., 1992].

4.2.4 Gain with transmission noise on the hologram

We finally carried out additional simulations adding a transmission noise to the hologram. We have simulated several levels of random transmission noises to create transmission errors on the hologram pixels. The results are shown in Fig. 32.

The effect of this kind of noise is numerically approximately equivalent to the photon noise treated above (even if it is not the same phenomenon), and once again we show the limits of validity of our instrument, by varying the amount of the transmission noise: when this noise is less than 5% of the value of the hologram pixels (at $\lambda/20$) and 0.2% (at $\lambda/100$), the performances are not degraded. If the transmission noise is more than 20% of the value of the hologram pixels (at $\lambda/20$) and 75% (at $\lambda/100$), the performances match those of the apodized coronagraph (without hologram).

This means that it is sufficient to control the "actuators" of the hologram with a precision better than 0.2%–5% in order to override the limitation introduced by the transmission noise. In this case the results are equivalent, for different F_s/F_p ratios, to those shown in the last row of Figs. 29 and 30 (D).

4.3 Summary of the simulations

Starting from the best solution, i.e. a hologram with an apodized reference beam and without a twin wave (D), we assumed 60s exposures, both in recording the hologram and observing, using a 6.5m aperture in the V band ($\lambda = 550$nm), with a filter width of 10nm.

We see that the photon noise is negligible for source magnitudes brighter than $V = 7$ (at $\lambda/20$) and $V = 3$ (at $\lambda/100$); the hologram performance is then optimal, and independent on the star magnitude. In our simulations, those magnitudes correspond to about $\approx 3 \times 10^6$ (at $\lambda/20$) and $\approx 3 \times 10^8$ (at $\lambda/100$)

photons per speckle in the hologram, and their performances are degraded below this value.

Above magnitude $V = 13$ (at $\lambda/20$) and $V = 11$ (at $\lambda/100$), where the hologram has $\approx 3 \times 10^4$ (at $\lambda/20$) and $\approx 2 \times 10^5$ (at $\lambda/100$) photons per speckle respectively, the sensitivity gain vanishes with respect to a Lyot apodized coronagraph without a hologram.

With a ground-based telescope, affected by atmospheric perturbations, bright stars may provide enough photons during short exposures, shorter than the lifetime of the "seeing", to activate both a conventional adaptive optics system giving a high Strehl ratio, and, within the coronagraphic attachment, the recording of a dynamic hologram. On fainter stars, a bright Laser Guide Star may similarly serve for both stages of adaptive correction.

In space, where wavefront perturbations are much smaller and stable over longer periods, some faint feature detection sensitivity can be gained by recording the hologram on a star which is brighter than the observed source, or on a ground-based laser source (which is not affected by turbulence if its emitting aperture is unresolved).

4.4 Discussion about a practical implementation

In the following subsections, two aspects for the future development of the instrument are considered: the chromaticism of the coronagraph with a hologram; and the problems introduced by a source that is poorly resolved, as for example a star in the case of the direct imaging of exo-planets.

4.4.1 Achromatizing a hologram

The fringe spacing in the hologram is normally proportional to wavelength but can be made invariant if the deviating prism (see Fig. 23 in Chap. 3) in the reference beam is replaced by a diffraction grating. If the grating operates in the first order, its angular dispersion indeed increases the incidence angle of light at increasing wavelengths.

This can reduce the hologram's wavelength sensitivity, both during the recording stage and the observations, and increase the usable spectral bandwidth, although the speckles contributed by the direct beam are also dependent on the wavelength.

Figure 33: Laboratory test carried out in Calern involving a hologram in a coronagraph device: picture of the pupil.

Further simulations, achieved within a range of wavelengths, would be of interest to specify the bandwidth then reachable.

Another approach involves a Lippmann-Bragg hologram, i.e. a thick hologram where the fringes are patterned as stratifications throughout the depth of the recording layer. These can be wavelength-multiplexed, and can simultaneously reconstruct the variously colored wavefronts that have been recorded. Some recording materials, such as lithium niobate single crystals or polymeric compounds [Shishido and Ikeda, 2007], are erasable and re-usable. Their moderate recording sensitivity however may require a bright laser star.

Preliminary laboratory tests to implement this kind of device are ongoing in the laboratories of Calern (France), and are shown in Figs. 33, 34a and 34b.

Following these already initiated laboratory simulations, tests on ground-based adaptive telescopes may be possible with available camera and Spatial Light Modulator components.

4.4.2 Resolved parent source

The original Lyot coronagraph is highly tolerant with respect to a source being resolved, as demonstrated by its initial success on the solar corona. However, a source, as for example a star, which is slightly resolved by the telescope or the hypertelescope [Tallon and Tallon-Bosc, 1992, Labeyrie, 1996, Le Coroller et al., 2004] can degrade the hologram recorded with its light, and also degrade the nulling depth in the image cleaned by a pre-recorded hologram. In both cases, what matters is the invariance of the hologram, particularly in terms of fringe positions, with respect

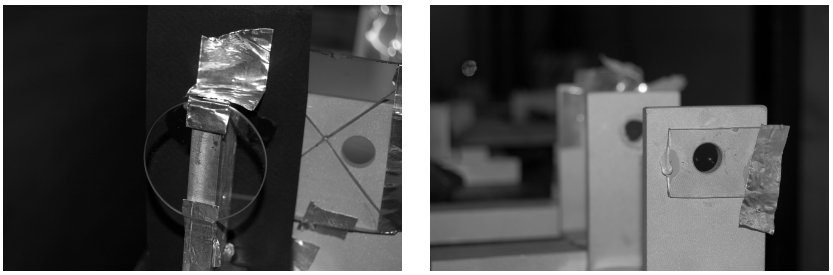

(a) Picture of the lens. (b) Zoom on the occulter.

Figure 34: Practical tests for the realization of a coronagraph with adaptive hologram using the design with a hole in a central mirror. This implementation is carried out under the supervision of Antoine Labeyrie by the team of Calern (France).

to a slight motion of a point star. Such a motion produces identical translation shifts of the central and peripheral focal patterns separated by the micro-prism.

The fringe pattern recorded in the hologram, located at a nearly infinite distance in the relayed pupil, is therefore nearly invariant. The pupil indeed remains fixed, and both interfering wavefronts reaching it become tilted by the same amount, while their phase difference is invariant. Their speckle detail is however slightly modified by the varying edge effects at the boundaries of the micro-prism and field lens.

Further simulations and laboratory experiments will be of interest to estimate the tolerable apparent size of the star vs. the desired nulling depth.

4.5 Results

Our simulations of a coronagraph provided with a dynamic hologram, and the comparison with other forms of adaptive coronagraphy, show that the theoretical photon-limited sensitivity in detecting faint exo-planets, or in detecting faint features near extragalactic sources as quasars, is comparable. These methods will therefore need to be compared in terms of their technical implementations. Hybrid methods, for example combining an adaptive mirror before the occulter and a hologram after, are likely to be similarly limited by the photon noise but may also have practical merits, such as relaxing the accuracy of the actuators [Putnam et al., 2006].

Depending on the holographic processes and materials that will become available, various forms of practical implementa-

tion may be of interest. With some re-writable holograms using amplifying photo-sensitive materials, no electronic image processing may be needed. Instead, and for a better flexibility, the recording and diffractive functions may be separated, using respectively a camera and a spatial light modulator.

With a $\lambda/20$ wavefront bumpiness, the feature detection limit is improved, in terms of flux ratio between a bright source and a faint feature, from $10^{4.5}$ to $10^{7.9}$. In terms of photon noise, we found that the hologram improves the performance of the coronagraph if it is recorded with more than $\approx 3 \times 10^4$ photons per speckle. With a $\lambda/100$ wavefront bumpiness, the detection limit improves from $10^{5.7}$ to $10^{10.8}$, and the hologram improves the performance of the coronagraph if it is recorded with more than $\approx 2 \times 10^5$ photons per speckle.

Finally, in the framework of a practical implementation, it is sufficient to control the "actuators" of the hologram with a precision better than 0.2–5% in order not to be limited by the transmission noise. This allows to improve the performances of the coronagraph by a factor 1 000–10 000, and makes this technique suitable for being developed and successfully applied to the next generation of space telescopes.

II

Photometric and spectroscopic observations and data reduction of multiply imaged quasars

5 Quasar observations

Multiply imaged quasars are of great interest in astrophysics. Indeed, from the observed flux and color variations of the lensed components, it is possible to trace their origin as either due to intrinsic variations caused by the accretion mechanism of the quasar itself or due to microlensing effects, caused by stars in the lens galaxy [Wambsganss, 2006].

In this chapter, we will summarize the observational tools used to carry out a photometric study of the multiply imaged quasars HE0435–1223 (described in detail in Chap. 6) and UM673 (described in Chap. 7). In particular, we briefly state the framework of the observations (Sect. 5.1); we describe the telescope equipment (Sect. 5.2), the method used to choose the photometric reference stars (Sect. 5.3), and finally the two reduction methods: PSF fitting (Sect. 5.4) and difference imaging (Sect. 5.5).

5.1 Framework

The photometric observations of HE0435–1223 and UM673 were performed in the framework of the MiNDSTEp (Microlensing Network for the Detection of Small Terrestrial Exoplanets) consortium: an international collaboration, which has as a main target the systematic observation of bulge microlenses [Dominik et al., 2010a] for studying the population of planets down to the Earth mass and below. The collaboration started in 2008 involving the Danish 1.54m telescope at the La Silla Observatory (Chile). In 2009, the MONET 1.2m telescopes at McDonald Observatory (Texas, USA) and at SAAO (South Africa) joined the network.

We participated to this consortium covering $\approx$ 120 observing nights over four seasons[1] at the Danish Telescope. During the nights, several projects were carried out. We summarize these project here below, and we address to the relative appendices and chapters for the details about each project and for the results.

1 The observing nights covered by the author are $\approx$ 65

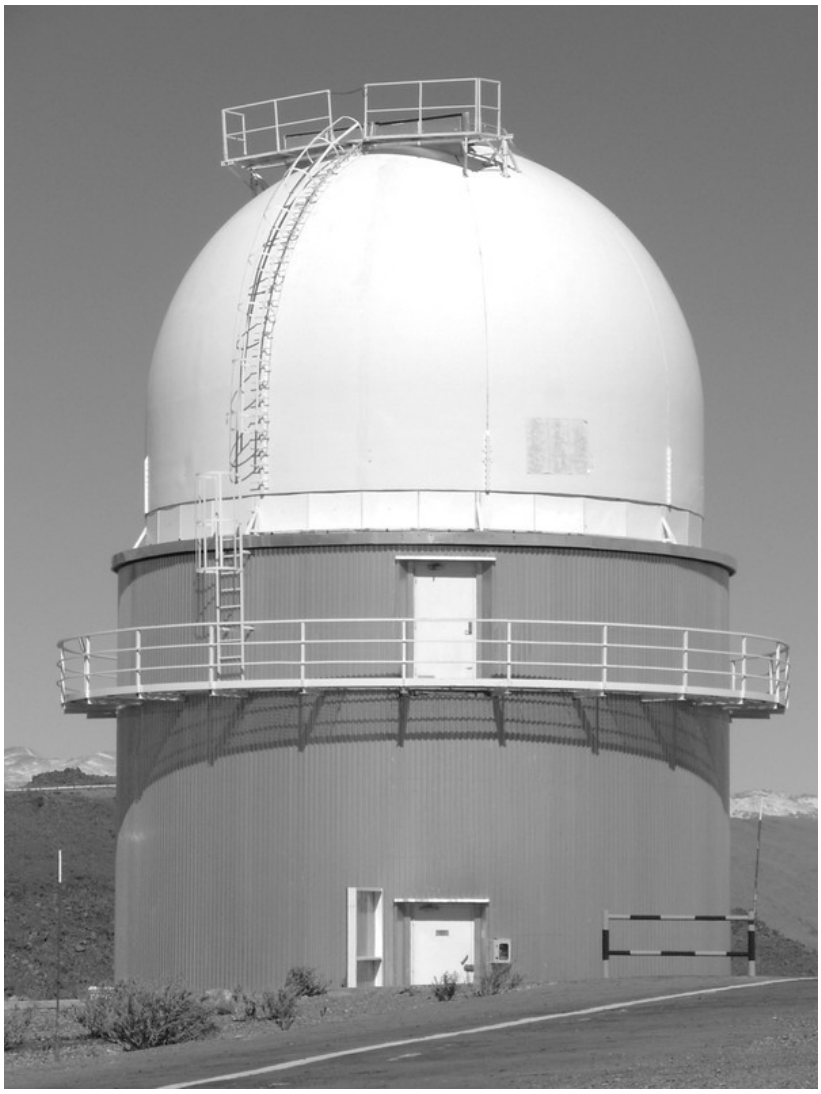

Figure 35: Picture of the Danish 1.54m telescope dome at the La Silla observatory, Chile.

- As we said, the main project consists in the systematic observation of bulge microlenses. Thanks to a system of prompt alerts based on the OGLE (the Optical Gravitational Lensing Experiment) and MOA (Microlensing Observations in Astrophysics) surveys, and on data collected from the Danish telescope and with other small size telescopes of the network, a detected anomaly in the light curve of a bulge object can be followed in real time with a dedicated and increased sampling, and spread the alert to the other telescopes to make possible the detection of very small amplitude and short duration anomalies. A brief summary of the details of this project and related results are given in App. B.

  bulge microlenses

- When the bulge is not observable, one of the largest parallel projects of this campaign is the observation of planetary transits. Using the technique of defocused photometry, it was possible to obtain very detailed light curves relative to several exo-planets, as for example WASP (Wide Angle Search for Planets) objects. The photometric accuracy and the scatter obtained with this technique is comparable to the results achieved with the CoRoT (COnvection ROtation and planetary Transits) satellite. A description of this project and a summary of the related works can be found in App. C.

  planetary transits

- Other side projects concern the observation of asteroids, the resolution of the core of globular clusters, the astrometric follow-up observations of Jovian Irregular Satellites and finally a Main Belt Comet follow up observation.

  other projects

- The parallel project that we proposed was the photometric multi-band observation of several lensed quasars: HE0435–1223, UM673/Q0142–100 (described in detail in Chap. 6 and Chap. 7), Q2237+0305, WFI2033–4723 and HE0047–1756. The first two objects were deeply studied by our team.

  gravitationally lensed quasars

5.2 Equipment

We observed the gravitationally lensed quasars during four seasons (2008–2011) using the Danish 1.54m telescope at the La Silla Observatory (Fig. 35). We used the DFOSC instrument (Danish Faint Object Spectrograph and Camera) for imaging and photometry. DFOSC is provided with a 2147×2101 pixel CCD device, covering a $13.7' \times 13.7'$ field of view with a resolution of

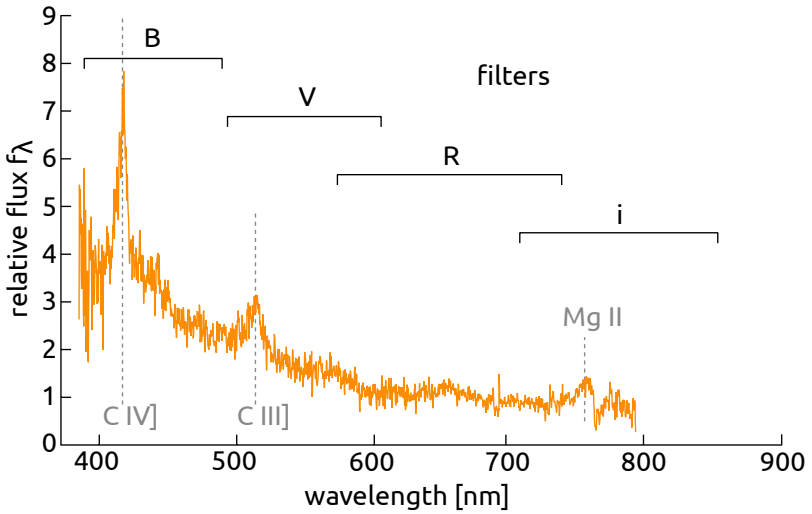

Figure 36: Position and bandwidth of the BVRi DFOSC filters superposed over the unresolved spectrum of HE0435–1223. The figure is a composition made from the spectrum shown in the paper of Wisotzki et al. [2002].

0.39″/pixel. The gain of the device is 0.74 electron/ADU in high-mode, while the RON (Read Out Noise) in this mode is 3.1 electrons [Sørensen, 2000].

The data were generally collected in 3 different filters[2]: Bessel V, Bessel R and Gunn i (see Fig. 36 and Table 2). Starting from the 2011 season, observations in the Bessel B filter were also carried out.

5.3 Reference stars

For the calculation of the flux ratio between two selected stars we applied the following method for each observation. We superposed the image of the first star on the fixed image of the second star as shown in Fig. 37. The light and black grids represent the images of the first and the second star, respectively. The big dots correspond to the knots for which the counts are known. The values $p(x, y)$ and S are the counts for each knot of the first and the second star, respectively.

To perform a precise fitting we have first to superpose these images with an accuracy better than 1 pixel. Even so, the knots of both images will not perfectly coincide with each other as shown in Fig. 37. Therefore we have to calculate intermediate

2 Information available on the Internet at http://www.eso.org/lasilla/telescopes/d1p5/misc/dfosc_filters.html

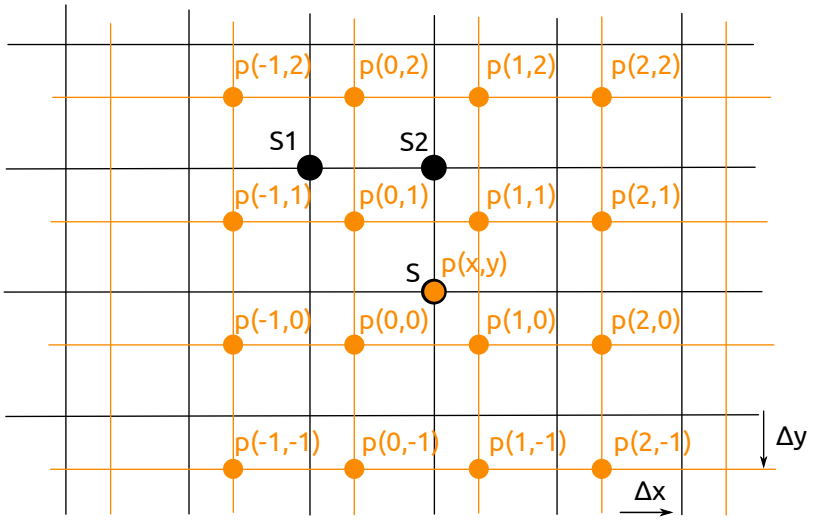

Figure 37: Scheme for the superposed images of the first (light) and second (black) stars. The big dots correspond to the knots with known fluxes. The arrows Δx and Δy indicate the shift between the images. Credits: Andrii Elyiv.

values, for example $p(x, y)$, which we may compare with the value S at the same point. For that we used bicubic interpolation [Press et al., 1992]. The intermediate value $p(x, y)$ is expressed via the polynomial:

$$p(x, y) = \sum_{i=0}^{3} \sum_{j=0}^{3} a_{i,j} x^i y^j. \tag{5.1}$$

To derive the values of the 16 coefficients $a_{i,j}$ we resolved this set of equations for 16 knots around the considered point $p(x, y)$. All of them are shown as orange dots in Fig. 37. Using this coefficient matrix $a_{i,j}$ we may derive $p(x, y)$ at any point. For the fitting of both images we minimized the quantity

$$\Delta(A,\ \Delta x,\ \Delta y) = \sum_{k} (A p_k(x + \Delta x,\ y + \Delta y) - S_k)^2, \tag{5.2}$$

which is the sum over all knots k of the first star image; A is the ratio between the total flux of the second and the first star, Δx and Δy are the relative shift between the two superposed images. Before the first iteration, we set the three parameters A, Δx and Δy within reasonable ranges. The factor A which minimizes Δ is the ratio between the fluxes of the two stars.

Table 2: Parameters of the DFOSC filters used for the photometry of the observed gravitationally lensed quasars.

Filter	ESO (#)	Size (mm)	λ (nm)	Δλ (nm)
Bessel B	450	C60.0	433.57	102.29
Bessel V	451	C60.0	544.80	116.31
Bessel R	452	C60.0	648.87	164.70
Gunn i	425	C60.0	797.79	142.88

5.4 PSF fitting method

One of the reduction techniques used in the study of the quadruply imaged quasar HE0435–1223 was the PSF fitting method, also used to determine the most adequate reference star, and applied both to HE0435–1223 and UM673.

For the fitting of the lens system we used the image of the calculated reference star as the reference PSF. Next we fitted each frame using several adjustable PSFs for the several quasar images (four for HE0435–1223 and two for UM673), and an additional PSF for the lensing galaxy, fixing the relative astrometric coordinates between the different components. In such a way we had several free parameters: the Δx and Δy relative coordinates of the gravitational lens system with respect to the reference star, and the central fluxes of the components to fit.

After minimization of the squared differences between the fluxes of the real lens system image and the simulated image with several PSFs, we derived the best fitted parameters. When doing this we used bicubic interpolation for the superposition of the individual PSFs and lensed components to better than 1 pixel. To construct the light curves, we calculated the flux ratios between each component and the reference star. This method, is based on an Object Pascal code developed by Andrii Elyiv.

5.5 Difference imaging method

We also decided to calculate the light curves using difference imaging as an independent method, also called "image subtraction".

The aim of the difference imaging technique is to subtract from each image of the field (indicated as "frame" in the following) one image of the same field (called "reference frame") taken at a different time under the best seeing conditions. This operation produces a set of subtracted frames where only the

relative flux variations between the two images (generic frame and reference frame) are visible. Performing aperture photometry on these subtracted frames, and in particular at the positions of the lensed QSO components, we derive the light curve of the lensed components.

However, differences in seeing, focus and guiding precision between frames collected at different times may produce variations in the shape of the PSF: trying the subtraction without additional operations could produce high residuals due to potential PSF slope variations. Several methods have been developed to force the PSF of the images to match [Alard, 1999, 2000]. These methods are particularly useful in crowded fields such as the galactic bulge, but less successful in sparse fields. In this paper we adopt the method proposed by Phillips [1993] and already successfully applied by Nakos et al. [2005], based on FFT (Fast Fourier Transform). This method is based on a code developed by Joel Poels and written in Python language.

If r is the reference frame and f a generic frame, then

$$f = r \otimes k, \tag{5.3}$$

where k is the convolution kernel describing the differences between the PSFs, unknown, and $\otimes$ indicates the convolution product. In the Fourier space, the previous equation can be noted as

$$F = RK, \tag{5.4}$$

where the terms are the Fourier transform ($\mathscr{F}$) of the generic frame f, the reference frame r, and the convolution kernel k. Then

$$k = \mathscr{F}(F/R). \tag{5.5}$$

Phillips [1993] gives a discussion about the limits of this technique and the solutions adopted to avoid problems with background and high frequency noise.

We normalized the frames in flux by fixing the magnitude of the reference star in each filter using the values of the catalogs mentioned above. Then we used the difference imaging method on the normalized frames. With this technique, all the non variable objects in the field disappear, allowing to automatically suppress the contribution of the lensing galaxy which is an extended and photometrically constant object.

To obtain the light curves, we performed aperture photometry of the residuals, using the positions of the reference star and of the lensed components previously derived.

6 HE0435-1223

In the present chapter we focus on the gravitationally lensed quasar[1] HE0435–1223 (see Figs. 38 and 39), showing the observational results published in a recent paper Ricci et al. [2011c,b] and concerning a systematic multi-band photometric observation, performed in the VRi spectral bands with the Danish 1.54m telescope at the La Silla Observatory.

In Sect. 6.1 we remind the previous observations carried out for this object. In Sect. 6.2 we explain how the observations were performed; in Sect. 6.3 we focus on the data reduction, carried on with two independent techniques (difference imaging and PSF fitting) described in Chap. 5 and used to construct the light curves. In Sect. 6.4 we briefly present the results. Finally, in Sect. 6.5 we summarize the conclusions.

6.1 Previous observations

The QSO was discovered by Wisotzki et al. [2000] in the course of the Hamburg/ESO digital objective prism survey, and confirmed to be a quadruply imaged quasar by Wisotzki et al. [2002]. The lensing galaxy was initially identified as an elliptical with a scale length of $\approx$ 12kpc at a redshift in the range $z = 0.3$–0.4. The time delays between the four images of the quasar, labeled "A", "B", "C", and "D", starting from the brighter one and proceeding clockwise (see Table 3 for the astrometry) were estimated around ten days, and the quasar itself showed some signs of intrinsic variability [Wisotzki et al., 2002].

Afterwards, the value of the redshift for the lensing galaxy was estimated as $z = 0.44 \pm 0.20$, and the quasar redshift was confirmed to be $z = 1.6895 \pm 0.0005$, with a Δz between the components of ≈ 0.0015 RMS [Wisotzki et al., 2003]. Such spectrophotomeric observations showed some possible signature of microlensing effects in the continuum and in the spectral emission lines for the component "D".

Morgan et al. [2005] provided milliarcsecond astrometry, revised the value of the lens redshift at $z = 0.4546 \pm 0.0002$ using the Low-Dispersion Survey Spectrograph 2 (LDSS2) on the Clay

1 RA (J2000): 04:38:14.9, DEC (J2000): -12:17:14.4

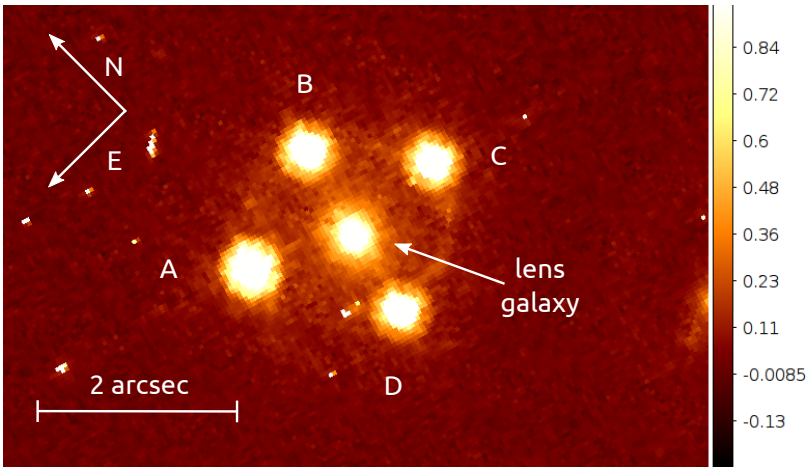

Figure 38: Image of HE0435–1223 taken with the Hubble Space telescope. The image was taken with the WFPC2 instrument using the F555W filter. Credits: The Hubble Legacy Archive.

6.5m telescope, and studied the galaxy environment of the lens, as it is placed in a dense galaxy field. The results do not show any evidence of a cluster for the considered galaxies. However, the nearest galaxies (G20, G21, G22, G23, G24 in Fig. 40) whose redshifts were not measured, let the scenario open. Nevertheless, the results of a deep investigation concerning the direction of an external shear in the gravitational field of the lens do not show any evident correlation with the position of the nearby galaxies. As a remaining explanation, Morgan et al. [2005] suggested the presence of substructures in the lensing galaxy.

The first systematic optical monitoring in the only R filter, covering the years between 2003 and 2005, was carried out by Kochanek et al. [2006], who provided astrometric measurements compatible with the previous works, measured the time delays between the images ($\Delta t_{AD} = -14.37$, $\Delta t_{AB} = -8.00$, and $\Delta t_{AC} = -2.10$ days, with errors respectively of 6%, 10% and 35%), and finally confirmed the lensing galaxy as an elliptical with a rising rotation curve.

Furthermore, Mediavilla et al. [2009] observed HE0435–1223 in the framework of a monitoring of 29 lensed quasars, and attributed eventual microlensing events to the normal stellar populations, while Blackburne and Kochanek [2010] focused on the quasar itself, applying a model with a time-variable accretion disk to the object. Mosquera et al. [2010] found clear evidence of chromatic microlensing in the "A" component, and provided an estimate of the disk size in the R band in agreement with the simple thin-disk model. Blackburne et al. [2010] used the chro-

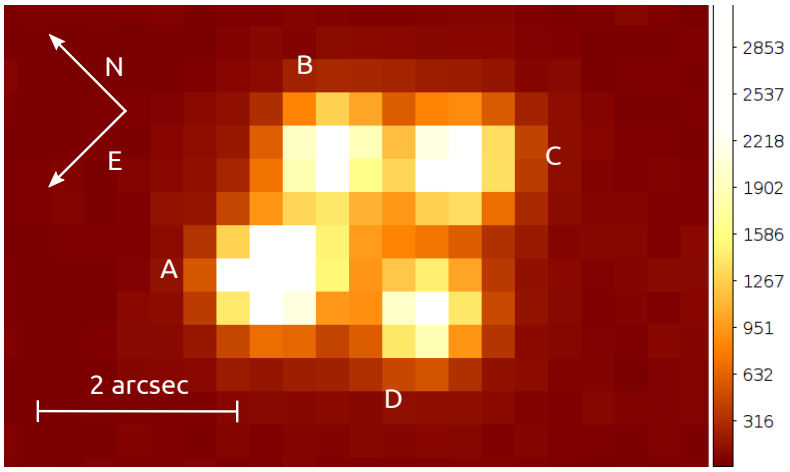

Figure 39: Image of HE0435–1223 taken with the Danish 1.54m telescope.

matic microlensing to model the accretion disk, and Courbin et al. [2010] recalculated the time delays with N-body realizations of the lensing galaxy, which they thought to belong to the "B" component ($\Delta t_{BA} = 8.4$, $\Delta t_{BC} = 7.8$ and $\Delta t_{BD} = -6.5$ days with errors of 25%, 10%, and 11% respectively).

Considering multi-color observations of other lensed quasars, a single-epoch multi-band photometry was used on the quasar MG0414+0534 to constrain the accretion disk model and the size of the emission region in the continuum [Bate et al., 2008, Bate, 2008, Floyd et al., 2008].

A multi-epoch multi-band photometry, carried out during several years, was used for the quasar Q2237+0305 by Koptelova et al. [2006], who observed the object during five years (1995–2000) in the VRI bands. Anguita et al. [2008] combined these data with OGLE observations. Mosquera et al. [2009] monitored the object in eight filters and found evidence for microlensing in the continuum, but not in the emission lines.

Table 3: Relative astrometric coordinates of the four lensed components "A", "B", "C", and "D" of HE0435–1223 and of the lens galaxy "G". Data taken from CASTLES.

	RA (arcsec)	DEC (arcsec)
A	$\equiv 0$	$\equiv 0$
B	-1.476 ± 0.003	0.553 ± 0.003
C	-2.467 ± 0.003	-0.603 ± 0.005
D	-0.939 ± 0.003	-1.614 ± 0.003
G	-1.165 ± 0.003	-0.573 ± 0.003

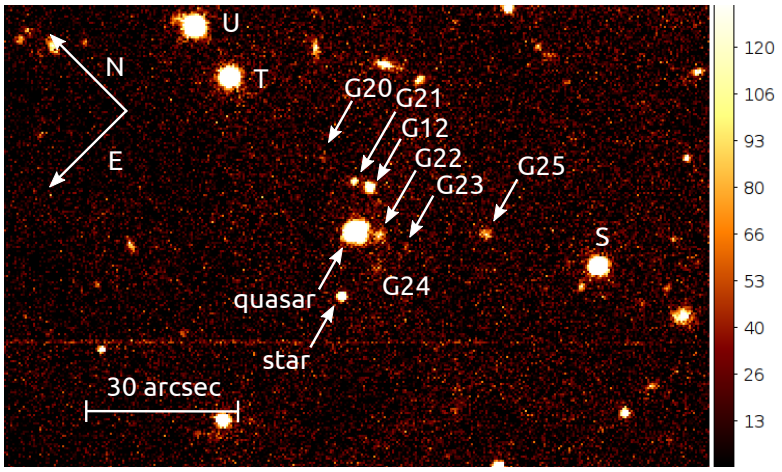

Figure 40: Zoom of a DFOSC i filter image showing the galaxy environment near HE0435–1223. The objects are labeled following the notation of Morgan et al. [2005]. The contrast, on a negative scale, was selected to improve the visibility of the galaxies. The image is a median of the three CCD frames collected on 2008/08/08.

Furthermore, Q2237+0305 was the object of deep studies focused on the lens galaxy and on the inclination of the accretion disk [Poindexter and Kochanek, 2010a,b].

Another example of multi-band observations is given by the gravitationally lensed quasar UM673, observed in the Gunn i and Cousins V filters between 1998 and 1999 [Nakos et al., 2005], in the VRI bands between 2003 and 2005 [Koptelova et al., 2009]. We also monitored this quasar during four seasons in the VRI bands, and we give the details in Chap. 7.

6.2 Pre-processing

The data were collected in 3 different filters: Gunn i, Bessel R and Bessel V . In order to work with the most homogeneous dataset, we selected only images with a 180s exposure.

For almost each night of observation, we also collected bias images and dome flat-fields, already treated *in loco* using an automatic IDL procedure, part of the MiNDSTEp pipeline for the observation of bulge microlenses. We then obtained master flat-fields for the different filters and master biases. When these images were not present for the desired date, we coupled to our science dataset, in the phase of pre-processing, the most recent set of master biases and master flat-fields.

We then obtained, during the 2008 season, 216 images:

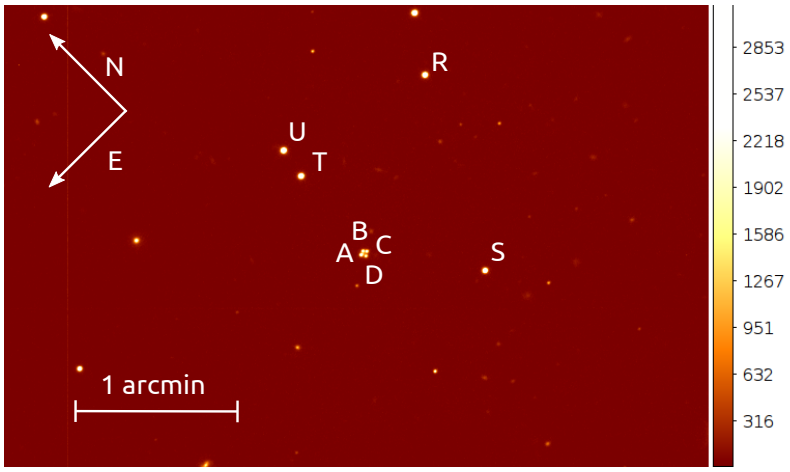

Figure 41: Zoom of a DFOSC i filter image showing the four components of the lensed quasar and four nearby stars. The components are labeled following the notation of Wisotzki et al. [2002]: "A" for the brightest component, "B", "C" and"D" clockwise. The stars "R", "S", "T" and "U" were used to search for a suitable reference star. The "R" star was finally chosen. The contrast of the displayed image, on a negative scale, was selected to improve the visibility of the lensed components. The image is a median of the three CCD frames collected on 2008/08/08.

- 70 in the i filter, corresponding to 26 nights;
- 83 in the R filter, corresponding to 32 nights;
- 63 in the V filter, corresponding to 25 nights;

distributed between July 27th and October 4th. Concerning the 2009 season, we obtained 116 images:

- 46 in the i filter, corresponding to 17 nights;
- 37 in the R filter, corresponding to 14 nights;
- 33 in the V filter, corresponding to 12 nights;

distributed between August 20th and September 19th.

The images were pre-processed (de-biased and flat-fielded), in particular the dome flats were used to erase the possible residual halos due to the inhomogeneous illumination. The sky background was subtracted fitting a 4^{th} degree surface after having masked stars and cosmic rays, and the images were recentered with an accuracy of 1px.

These steps were performed using a C++ pipeline developed by Pierre Guillaume Sprimont. We analyzed each image in order to disregard the problematic images in terms of bad tracking,

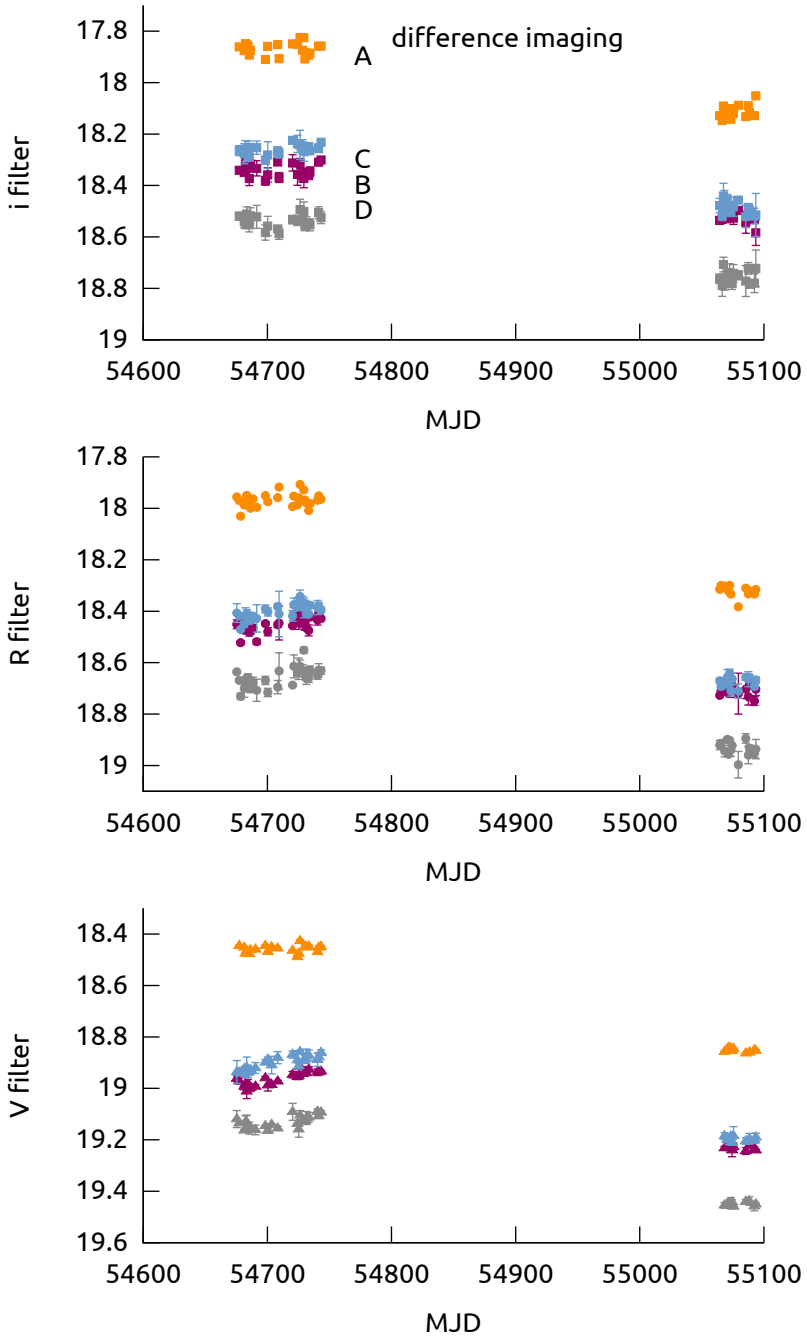

Figure 42: i, R and V light curves of the four lensed components of HE0435–1223, calculated using the difference imaging technique. The error bars correspond to the RMS of the average of one night of observation at the 1σ level.

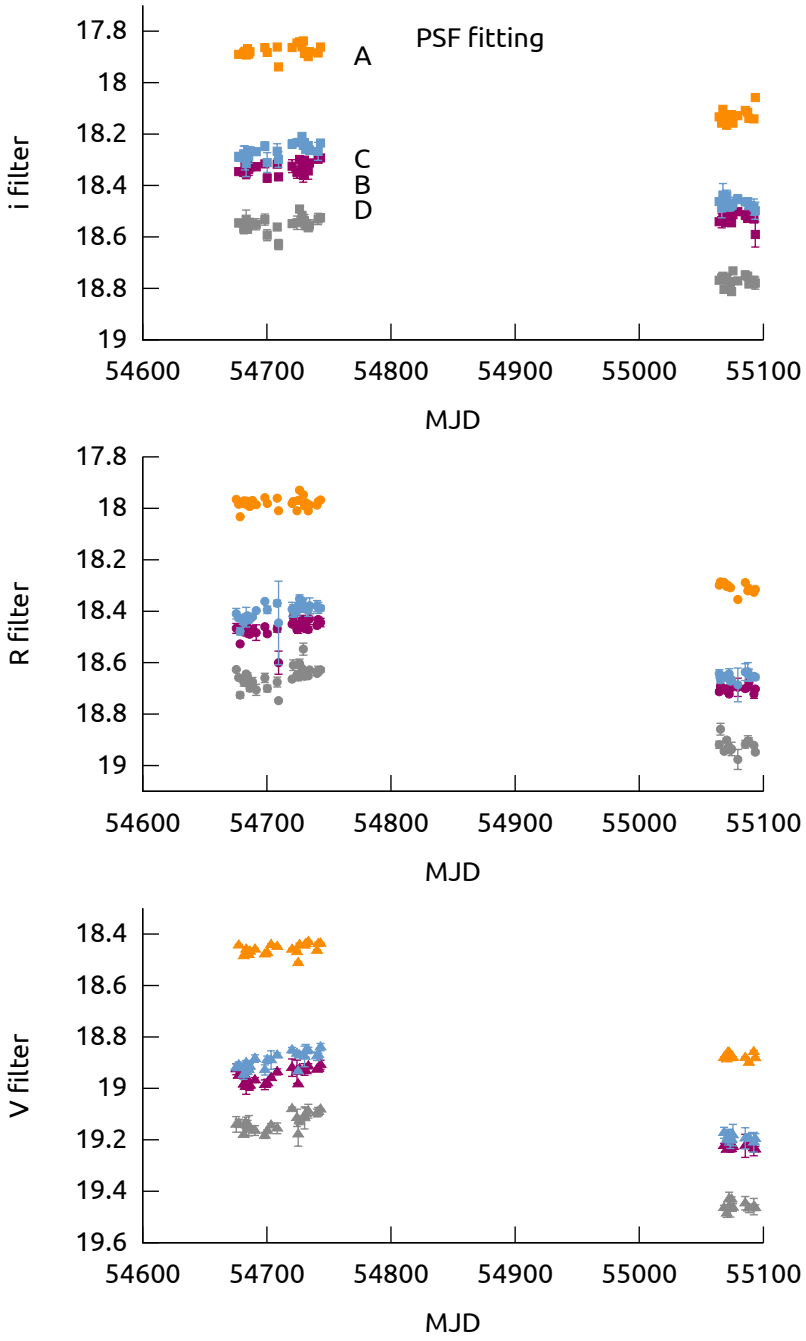

Figure 43: i, R and V light curves of the four lensed components of HE0435–1223, calculated using the PSF fitting technique. The error bars correspond to the RMS of the average of one night of observation at the 1σ level.

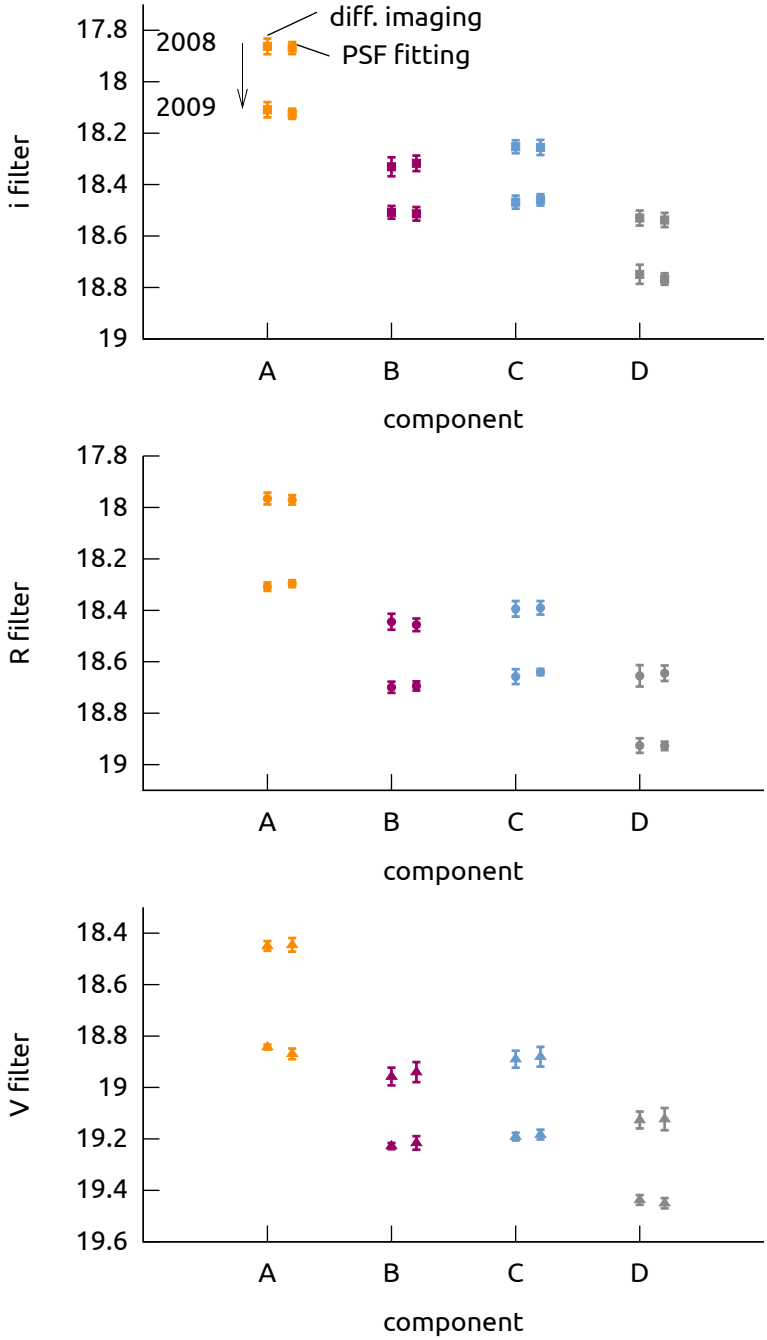

Figure 44: Average magnitude of each component for the 2008 season (upper symbols) and 2009 (lower symbols), calculated with the difference imaging technique and the PSF fitting method. The averages were calculated using an histogram of the values for each epoch, and fitting a gaussian curve. The error bar is the σ of the fitted gaussian.

particularly bad seeing (the components being completely unresolved) or bad focusing.

6.3 Data reduction

As a first step, we chose four stars near HE0435–1223, labeled "R", "S", "T" and "U" in Fig. 41, to search for a stable reference star. We examined the ratios between the fluxes of these stars in the V band as a function of time, to possibly detect some photometric variations between the 2 seasons.

We derived the light curves for the reference stars as magnitude differences and calculated the average difference, and standard deviations for the two epochs. As can be seen in Table 4, the stellar pairs including the "R" star show on average the smallest shifts between the two epochs. Moreover, the light curves of the "R" star show on average the least standard deviation σ. Therefore we may reasonably assume that the "R" star is the most stable reference star between the two seasons. Therefore we chose the "R" star as the reference for all subsequent photometric zero point determinations.

The magnitude for the reference star was taken from the USNO-B1.0 catalog for the i and R filters (16.27 and 16.33 respectively), and from the NOMAD1 catalog for the V filter (17.04). The light curves for the components of the gravitational lens system were then calculated using two independent methods: difference imaging and PSF fitting.

Concerning difference imaging we found, for the 2009 images, a weak linear dependence between the magnitude and the seeing, that we removed after calibration of this effect. The results for the 3 filters using this technique are shown in Fig. 42.

Concerning the PSF fitting method, we fitted four PSFs, one for each lensed component, and an additional PSF for the lensing

Table 4: Average V magnitude differences between the two epochs for the four reference candidates near HE0435–1223.

Pair	$\langle V_{2008} \rangle$	$\langle V_{2009} \rangle$
⟨S−R⟩	1.78 ± 0.03	1.77 ± 0.02
⟨S−T⟩	2.04 ± 0.07	1.95 ± 0.07
⟨T−R⟩	-0.411 ± 0.06	-0.40 ± 0.04
⟨U−S⟩	-2.357 ± 0.04	-2.42 ± 0.03
⟨U−R⟩	-0.581 ± 0.04	-0.65 ± 0.03
⟨U−T⟩	-0.338 ± 0.05	-0.31 ± 0.04

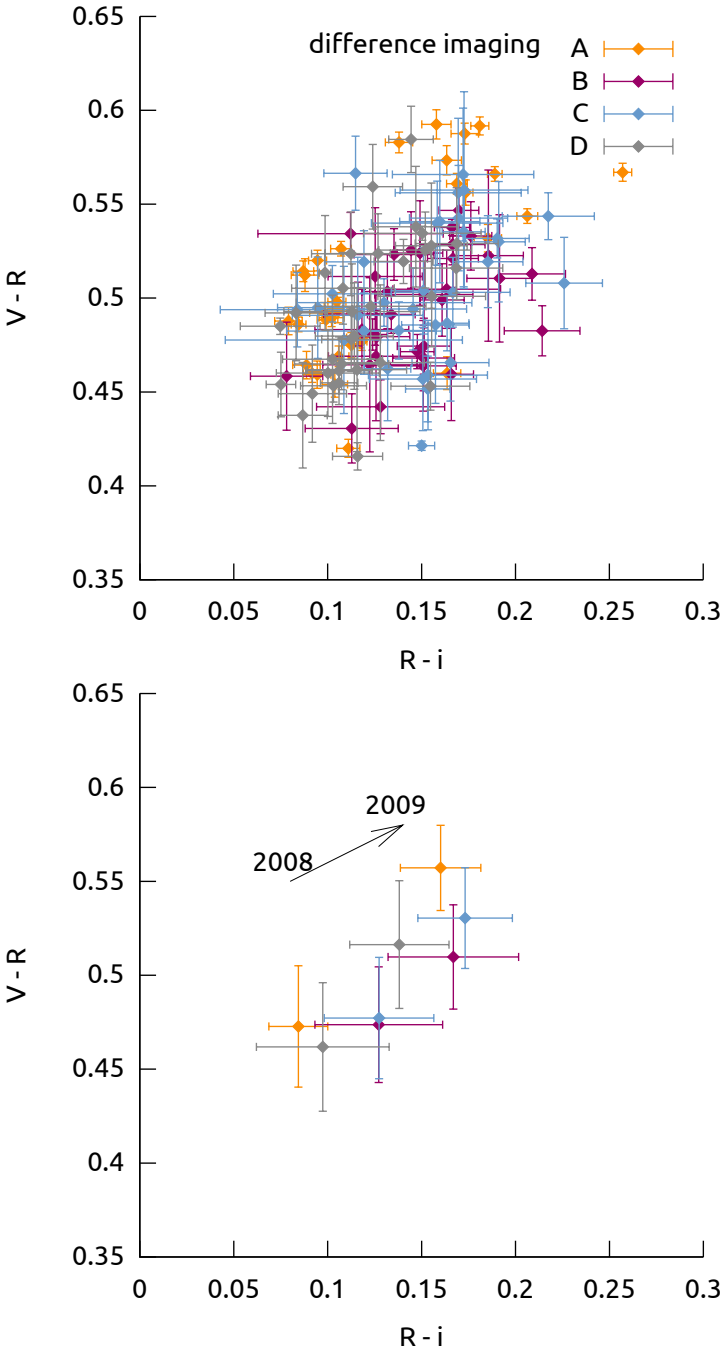

Figure 45: Above: $V-R$ vs. $R-i$ diagram of the four lensed components calculated with the difference imaging technique. Below: $V-R$ vs. $R-i$ diagram of the four lensed components (median over each epoch for each component).

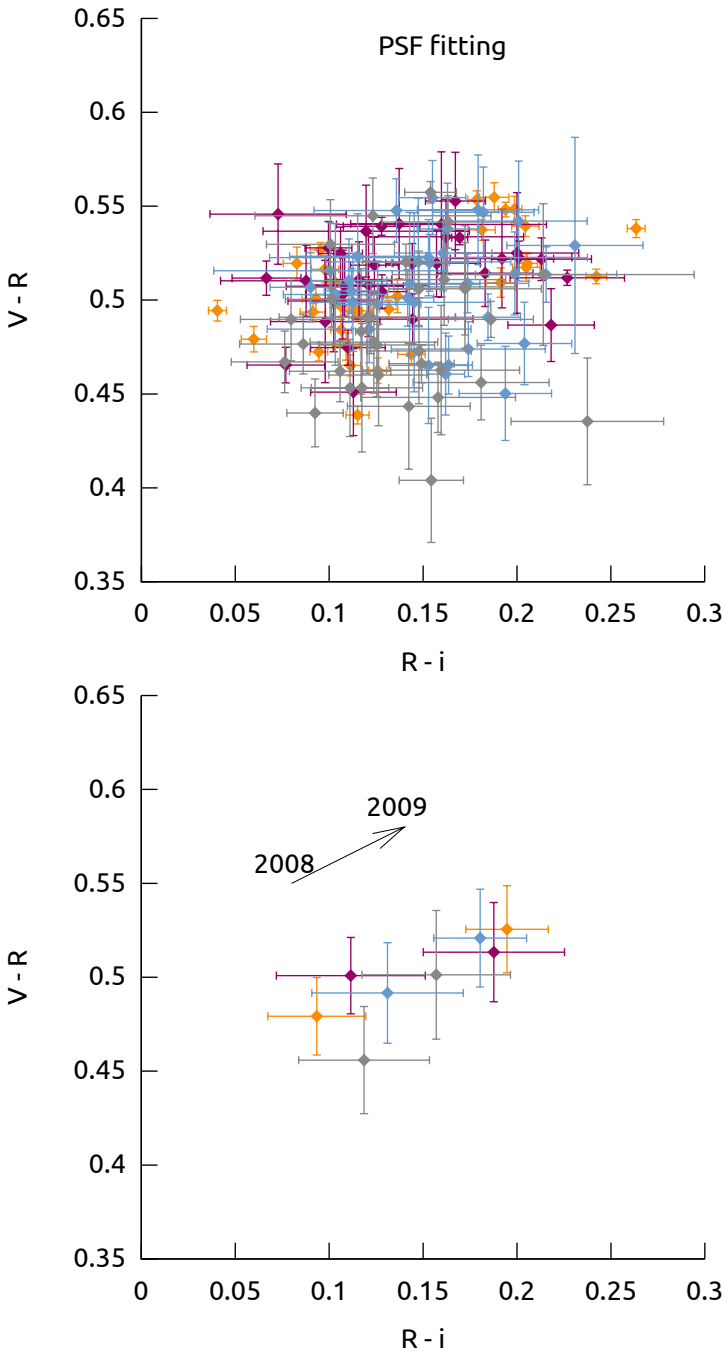

Figure 46: Above: $V-R$ vs. $R-i$ diagram of the four lensed components calculated with the PSF fitting technique. Below: $V-R$ vs. $R-i$ diagram of the four lensed components (median over each epoch for each component).

Table 5: Average magnitudes in the VRi bands of the four lensed components of HE0435–1223 during the two observing seasons (2008–2009), calculated with the difference imaging technique.

component	epoch	V	R	i
A	2008	18.45 ± 0.03	17.97 ± 0.02	17.86 ± 0.03
	2009	18.87 ± 0.02	18.30 ± 0.01	18.11 ± 0.03
B	2008	18.94 ± 0.04	18.46 ± 0.02	18.33 ± 0.04
	2009	19.22 ± 0.03	18.69 ± 0.02	18.51 ± 0.02
C	2008	18.88 ± 0.04	18.39 ± 0.03	18.25 ± 0.03
	2009	19.18 ± 0.02	18.64 ± 0.01	18.47 ± 0.03
D	2008	19.12 ± 0.04	18.64 ± 0.03	18.53 ± 0.03
	2009	19.45 ± 0.02	18.93 ± 0.02	18.75 ± 0.04

galaxy, and we fixed the relative astrometric coordinates using the astrometry provided by Kochanek et al. [2006]. The results for this method are shown in Fig. 43.

The error bars are calculated taking the RMS of the average of each night at the 1σ level.

6.4 Results

Both methods show a significant decrease in flux of the four lensed components between the 2008 and 2009 seasons. Fig. 44 shows that the amounts of the decrease are coherent between the two methods.

6.4.1 Flux variations

In order to estimate this decrease, we built an histogram of the magnitudes, and we fitted, for each component and each filter, two gaussian curves respectively for the 2008 and 2009 seasons. We took the center of the gaussians and their σ as average value for the magnitude, and their error respectively. The details are shown in Tabs. 5 and 6. In particular, all four components show a decrease by $\approx$ 0.2–0.4 magnitudes in all the filters, although we notice an amplitude slightly larger for component "A" in the V band.

The corresponding values expressed in sigma units show a shift between $\approx 11.3\sigma$ and $\approx 13.7\sigma$ in the V band, except for component "A" which shows a decrease by $\approx 26.3\sigma$. In the R and i filters, the shift is between $\approx 6.5\sigma$ and 7.5σ, except for

Table 6: Average magnitudes in the VRi bands of the four lensed components of HE0435–1223 during the two observing seasons (2008–2009), calculated with the PSF fitting technique.

component	epoch	V	R	i
A	2008	18.45 ± 0.02	17.97 ± 0.02	17.87 ± 0.02
	2009	18.84 ± 0.01	18.31 ± 0.02	18.12 ± 0.02
B	2008	18.96 ± 0.03	18.44 ± 0.03	18.32 ± 0.03
	2009	19.23 ± 0.01	18.70 ± 0.02	18.51 ± 0.03
C	2008	18.89 ± 0.03	18.39 ± 0.03	18.26 ± 0.03
	2009	19.19 ± 0.02	18.66 ± 0.03	18.46 ± 0.02
D	2008	19.13 ± 0.03	18.65 ± 0.04	18.54 ± 0.03
	2009	19.44 ± 0.02	18.93 ± 0.03	18.77 ± 0.02

component "A" ($\approx 15.0\sigma$ and $\approx 9.8\sigma$ respectively) and component "C" in the R band ($\approx 12.0\sigma$).

6.4.2 Color variations

For the fraction of nights when the object was observed in all the VRi filters, we were able to build the color-color diagram ($V-R$ vs. $R-i$) for the four components. The results are shown in Figs. 45 and 46. With the same technique used to estimate the decrease in flux, we also found a significant increase (≈ 0.05) for both the color indices $V-R$ and $R-i$ between the two observing seasons. The details are given in Tables 7 and 8. In particular, component "A" shows the largest shift in color.

The corresponding values expressed in sigma units show a shift in color between $\approx 1.3\sigma$ and $\approx 2.0\sigma$ for both color indices $V-R$ and $R-i$, except for component "A" (3.40σ in $V-R$ and 3.1σ in $R-i$).

Given the short time delays [Kochanek et al., 2006], these results support the fact that the magnitude and color variations are very likely due to intrinsic variations of the QSO, while the lensed "A" component is probably also affected by microlensing.

the global light curve

As a complementary approach, we decided to construct two "global i" light curves in order to better understand the nature of such different variations in flux and color index.

To construct the first one, we superposed the light curves of the four components by subtracting from "B", "C" and "D" their average 2008 difference in magnitude with respect to the "A" component, and we corrected the data for the time delays pro-

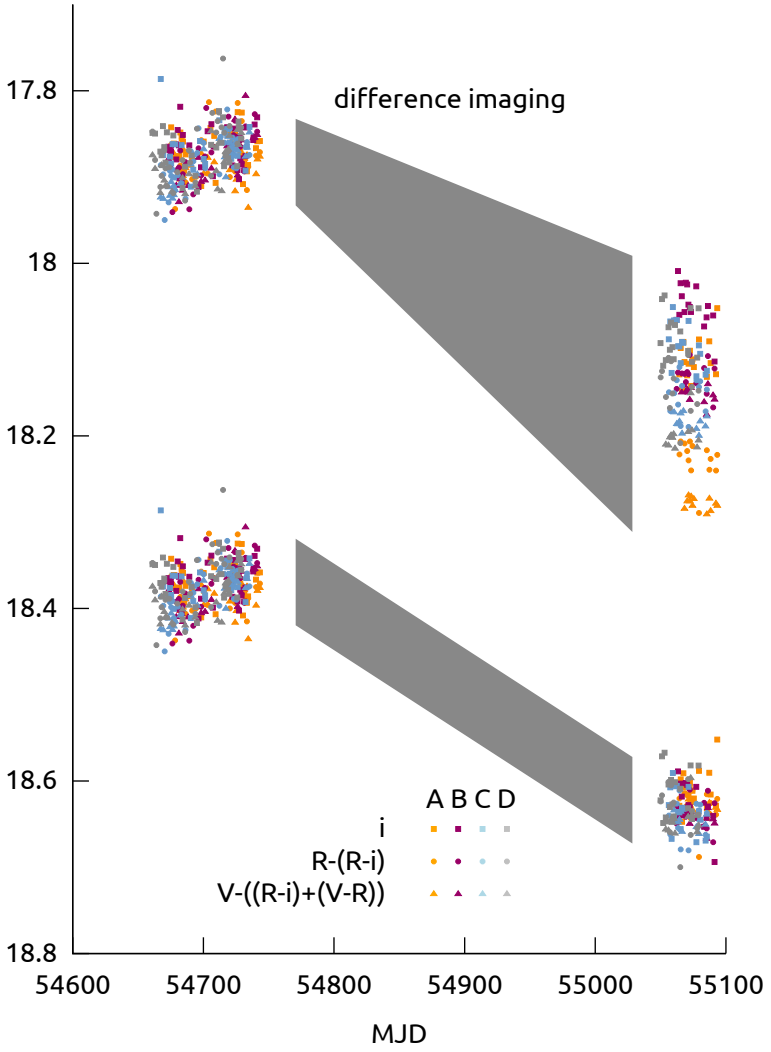

Figure 47: Upper light curve: "global i" light curve of the 4 lensed components of HE0435–1223 obtained by subtracting from "B", "C" and "D" their average 2008 i difference in magnitude with respect to the component "A"; then corrected for the time delays provided by Kochanek et al. [2006] and finally subtracting from the R and the V light curves the average 2008 $R-i$ and $(R-i)+(V-R)$ color indices, respectively. Lower light curve: repeating the same procedure, but correcting for the average 2008 magnitude and color indices for what concerns the 2008 data, and for the 2009 average magnitude and color indices for what concerns the 2009 data. The gray quadrilaterals help to connect the two epochs of observation. The figure shows the results obtained with the difference imaging technique.

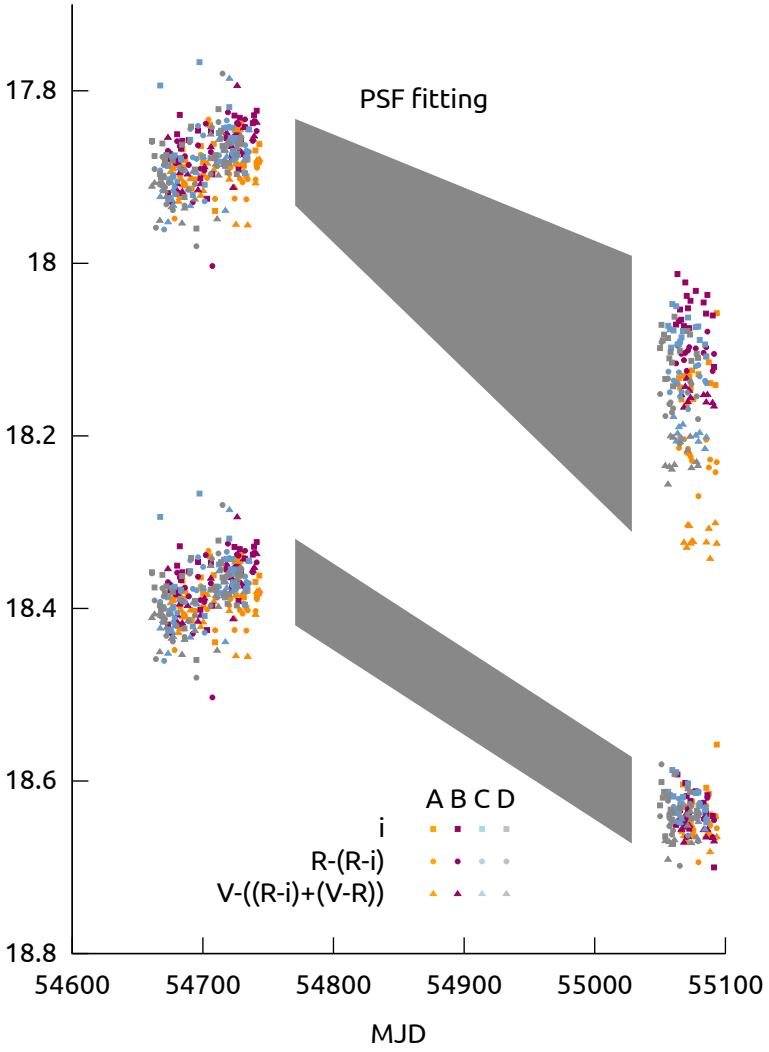

Figure 48: Upper light curve: "global i" light curve of the 4 lensed components of HE0435–1223 obtained by subtracting from "B", "C" and "D" their average 2008 i difference in magnitude with respect to the component "A"; then corrected for the time delays provided by Kochanek et al. [2006] and finally subtracting from the R and the V light curves the average 2008 $R-i$ and $(R-i)+(V-R)$ color indices, respectively. Lower light curve: repeating the same procedure but correcting for the average 2008 magnitude and color indices for what concerns the 2008 data, and for the 2009 average magnitude and color indices for what concerns the 2009 data. The gray quadrilaterals help to connect the two epochs of observation. The figure shows the results obtained with the PSF fitting technique.

Table 7: Averages and error bars (σ) characterizing the $V-R$ and $R-i$ color indices of each component of HE0435–1223 for the two observing seasons (2008–2009), obtained with the difference imaging technique.

component	epoch	$R-i$	$V-R$
A	2008	0.08 ± 0.02	0.47 ± 0.03
	2009	0.16 ± 0.02	0.56 ± 0.02
B	2008	0.13 ± 0.03	0.47 ± 0.03
	2009	0.17 ± 0.03	0.51 ± 0.03
C	2008	0.13 ± 0.03	0.48 ± 0.03
	2009	0.17 ± 0.03	0.53 ± 0.03
D	2008	0.10 ± 0.04	0.46 ± 0.03
	2009	0.14 ± 0.03	0.52 ± 0.03

vided by Kochanek et al. [2006]. Then, we superposed the obtained curves (one for each filter) by subtracting from the R and the V light curves the average 2008 $R-i$ and $(R-i)+(V-R)$ color indices, respectively. The goal of this first "global i" light curve is to visualize how the spreads in magnitude and colors evolve between the epochs. The results are shown in Figs. 47 and 48 (upper light curves).

To construct the second "global i" light curve, we repeated the same procedure, but we subtracted from the 2008 data of "B", "C" and "D" the average 2008 difference in magnitude with respect to the component "A", and from the 2009 data the corresponding average 2009 difference in magnitude. Similarly, we subtracted from the R and the V light curves the average 2008 and 2009 $R-i$ and $(R-i)+(V-R)$ color indices, respectively. The results are shown in Figs. 47 and 48 (lower light curves).

After such superpositions, we observe in 2008 a scatter in the data (see Figs. 47 and 48) significantly larger than those of the individual light curves (see Figs. 42 and 43); and in general a difference in scatter between the two epochs that we attribute to the intrinsic variation of the quasar both in magnitude and color.

We also observe a slightly growing trend in 2008, coherent with the results of Courbin et al. [2010].

magnitude of the lensing galaxy

Concerning the only PSF fitting method, we were also able to estimate the magnitude of the lensing galaxy as 19.87 ± 0.10 in the i band; 20.47 ± 0.13 in the R band; and 21.89 ± 0.24 in the V band.

No significant changes in the magnitude and in the color of the lensing galaxy were observed during the two epochs, and

Table 8: Averages and error bars (σ) characterizing the $V-R$ and $R-i$ color indices of each component of HE0435–1223 for the two observing seasons (2008–2009), obtained with the PSF fitting technique.

component	epoch	$R-i$	$V-R$
A	2008	0.09 ± 0.03	0.48 ± 0.02
	2009	0.19 ± 0.02	0.53 ± 0.02
B	2008	0.11 ± 0.04	0.50 ± 0.02
	2009	0.19 ± 0.04	0.51 ± 0.03
C	2008	0.13 ± 0.04	0.49 ± 0.03
	2009	0.18 ± 0.02	0.52 ± 0.03
D	2008	0.12 ± 0.03	0.46 ± 0.03
	2009	0.16 ± 0.04	0.50 ± 0.03

our results for the V and the i filters are coherent with those of Wisotzki et al. [2002] and Morgan et al. [2005] respectively.

Proceeding the same way, we did not find any evident color shift for the lensing galaxy: we find a value of 1.47 ± 0.33 and 1.36 ± 0.21 for the $V-R$ color index in 2008 and 2009, respectively; and 0.59 ± 0.17 and 0.61 ± 0.14 for the $R-i$ color index.

The stability of the flux of the lensing galaxy over the two epochs enforces the validity of our PSF fitting software, and we found sensibly larger error bars because the object is considerably fainter than the "A", "B", "C" and "D" components.

6.5 Conclusion

Systematic multi spectral band photometry of the quadruply imaged quasar HE0435–1223, carried out during two seasons (2008 and 2009), put in evidence a significant decrease in flux of the four lensed components between the two epochs.

The drop in flux observed for the four components between 2008 and 2009 is very likely due to a change in the intrinsic luminosity of the quasar. The same trend (intrinsic reddening of the quasar) probably accounts for the similar observed changes in the colors of the four lensed components.

This hypothesis is enforced if we suppose that the intrinsic photometric quasar variations in the different colors are not synchronized, which provide an explanation for the differences in scatter between the epochs (see Figs. 47 and 48). Microlensing

probably consists of the additional effect necessary to account for the larger flux variation of the "A" component.

The presented observations put also in evidence that a good-sampled multi-band photometry can help in discriminating the nature of the variability of multiply imaged objects, in particular gravitationally lensed quasars. We suggest to pair in the future this technique with integral field spectroscopy to provide an additional way for a still more detailed investigation of the phenomenon.

7 UM673

After having studied in Chap. 6 the flux and color variations of the quadruply imaged quasar HE0435–1223, we focus on the gravitationally lensed quasar UM673/Q0142–100 (see Fig. 49), a doubly imaged quasar[1] discovered by Surdej et al. [1987] during a high resolution imaging survey of HLQs (Highly Luminous Quasars) and deeply studied by our team [Smette et al., 1990, 1992, Daulie et al., 1993, Nakos et al., 2005].

We anticipate the results described in a new manuscript recently submitted [Ricci et al., 2011a], concerning a multi-epoch coverage over four seasons (2008–2011) of UM673, carried out in three filters (VRi).

In Sect. 7.1 we report the previous observations of the object, then we describe the observations and the pre-processing of the images in Sect. 7.2. Sect. 7.3 presents the reduction techniques; and the results are shown in Sect. 7.4. Finally, Sect. 7.5 describes the conclusions.

7.1 Previous observations

Surdej et al. [1988] reported a separation of 2.22″ between the components "A" (brighter) and "B" (fainter), and found their V magnitudes to be 16.9 and 19.1 respectively, at a redshift $z = 2.719$. The redshift of the sensibly fainter ($R = 19.2$) lensing galaxy, located very close to the "B" component, was derived to be $z = 0.49$, and the time delay between the two lensed components was estimated around 7 weeks.

A photometric monitoring of UM673 was performed during the years 1987–1993 [Daulie et al., 1993], but the photometry did not show any clear evidence for relative variations over the considered period.

In the framework of the CASTLES (CfA Arizona Space Telescope LEns Survey) project, precise astrometry (see Table 9) of the components and of the lens galaxy "G" was obtained[2], and its colors matched those of a passively evolving early-type galaxy at $z = 0.5$ [Muñoz et al., 1998].

1 RA (J2000): 01:45:16.5, DEC (J2000): -09:45:17

2 http://www.cfa.harvard.edu/castles/Individual/Q0142.html

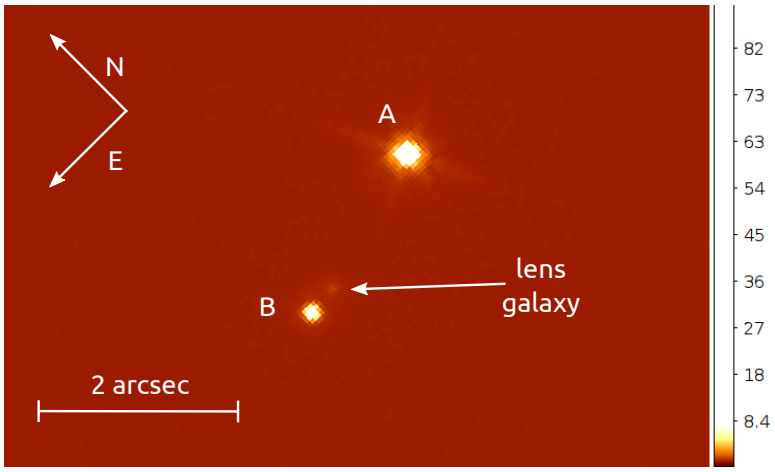

Figure 49: HST image of UM673 taken with the WFPC2 instrument using the F555W filter. The faint lens galaxy is visible. Credits: The Hubble Legacy Archive.

Lehár et al. [2000, 2002] reported HST observations of UM673 at optical and infrared wavelengths, and Sinachopoulos et al. [2001] observed the lensed quasar in the R filter for six seasons (1995–2000), detecting a significant increase by 0.3 magnitude of the combined system (lensed components and lens galaxy) with respect to the values reported at discovery, with a peak of 0.5 magnitude during the period 1995–1997. The authors performed the photometry on HST (Hubble Space Telescope) data taken in the R filter, and obtained magnitudes of 16.67, 18.96, and 19.35 for the "A", "B" components and the lens galaxy, respectively.

After spectrophotometric observations performed in 2002 by Wisotzki et al. [2004], which did not show any evidence of microlensing, the first multi-filter monitoring of UM673 was carried out by Nakos et al. [2005] between 1998 and 1999, in the Gunn i and Cousins V filters. Analysis of the light curves was made using three different photometric methods: image deconvolution [Magain et al., 2007], PSF (Point Spread Function) fitting, and image subtraction. Nakos et al. [2005] found that component "A" displayed possible evidence for microlensing.

Between 2003 and 2005, Koptelova et al. [2008, 2010b,a] observed the object in the VRI bands and succeeded for the first time in determining the time delay: $150^{+7}_{-18}{}^{+42}_{-36}$ days (at 68% and 95% confidence levels).

Finally, Fadely and Keeton [2011] examined the wavelength dependence of the flux ratios for several gravitationally lensed quasars using K and L-band images obtained at the 8m Gemini

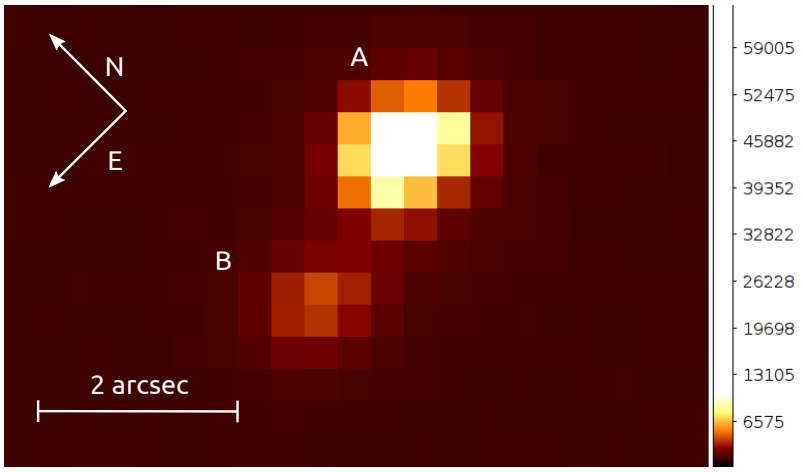

Figure 50: DFOSC i filter image, taken on 2008-08-03, showing the two components of the gravitationally lensed quasar UM673.

North telescope, detecting no difference between the two flux ratios for the specific case of UM673.

7.2 Pre-processing

We monitored UM673 during four seasons (2008–2011) using the Danish 1.54m telescope at the La Silla Observatory. With the exception of the re-aluminization of the primary mirror in 2009, the configuration software/hardware of the telescope did not change over the four epochs of observation. The data were collected in the Bessel V, Bessel R, and Gunn i filters.

We obtained a total of 130 images during the 2008 season:

- 42 in the V filter;
- 45 in the R filter;
- 43 in the i filter;

Table 9: Relative astrometric coordinates of the two lensed components "A" and "B" of UM673 and of the lens galaxy "G". Data taken from CASTLES.

	RA (arcsec)	DEC (arcsec)
A	$\equiv 0$	$\equiv 0$
B	2.145 ± 0.003	-0.613 ± 0.003
G	1.764 ± 0.003	-0.574 ± 0.003

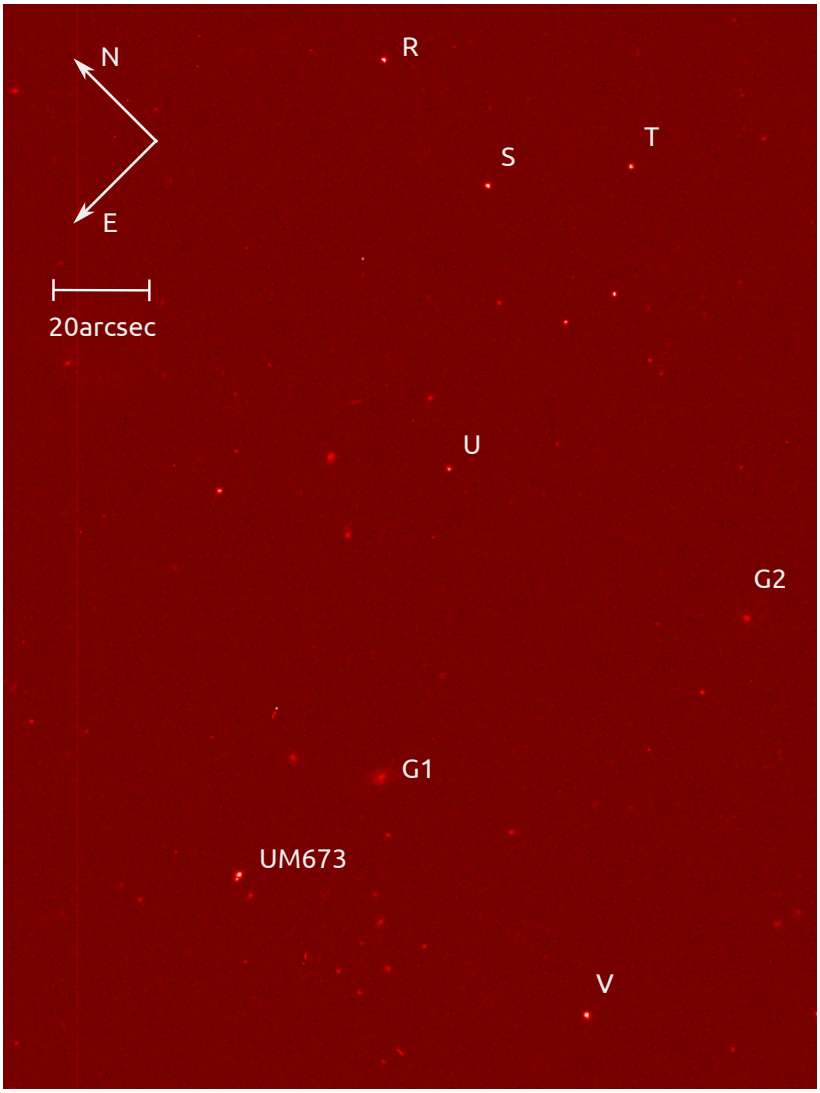

Figure 51: DFOSC V filter image, taken on 2008-08-03, showing the position of UM673 and the stars "R", "S", "T", "U", and "V" used to search for a suitable reference star. The "V" star was finally chosen. "G1" and "G2" are field galaxies.

covering 15 nights each. During the 2009 season, the number of collected images was 95:

- 34 in the V filter;
- 35 in the R filter;
- 26 in the i filter;

covering 13, 12 and 9 nights, respectively. Then, during the 2010 season the total number of images was 150:

- 72 in the V filter;
- 78 in the R filter;

covering 23 and 26 nights, respectively. Finally, during the 2011 season we obtained 113 images:

- 51 in the V filter;
- 53 in the R filter;
- 9 in the i filter;

covering 15, 16 and 1 night(s), respectively. The total number of images obtained over the four seasons is thus 488.

In 2010, no i filter image was taken, as the monitoring was foreseen since the beginning in the only VR filters, and the i filter was taken depending on the remaining telescope time with respect to the other MiNDSTEp parallel projects. All the frames were acquired with 180s exposures.

We treated the images following the same procedure as those relative to HE0435–1223 described in a previous paper [Ricci et al., 2011c], with the exception that we used the images already de-biased and flat-fielded *in loco* by the IDL (Interactive Data Language) automatic pipeline used at the Danish Telescope for the daily monitoring of the bulge microlenses.

7.3 Data reduction

We carefully checked the evolution of the scale of the images between the seasons, and we found a constant value of 0.395″ per pixel. We also checked the evolution of the position angle between the CCD pixel grid and the equatorial coordinate one, finding a change in angle between the seasons: 4.5′ between 2008 and 2009, 5.2′ between 2008 and 2010, and 4.7′ between 2008 and

Table 10: Maximum shifts of the R filter magnitudes between epochs and in σ units for the stars "R", "S", "T", "U", and "V" in Fig. 51.

star	Δm_R	$\Delta m_R/\sigma_R$
"R"	0.014	0.67
"S"	0.030	1.29
"T"	0.058	2.69
"U"	0.037	0.84
"V"	0.020	0.90

2011. We took this effect into account in our data reduction. Finally, we checked the seeing values for all the observations. We decided to fit the "U" star (see Fig. 51) with a two-dimensional Gaussian function, and we found that the R filter images had the best seeing. We then decided to search for a suitable reference star in that filter by choosing only the best seeing nights of the season, corresponding to a total of 9-18 images per season, depending on the filter.

Independently we have measured the flux ratio between the two bright galaxies "G1" and "G2" (see Fig. 51) using aperture photometry. In the analysis we used the best seeing images.

The reference candidates are the stars "R", "S", "T", and "V" in Fig. 51: we compared the fluxes of these stars with the total flux of the bright galaxies "G1" and "G2" using aperture photometry. For this test we decided to use galaxies because we can be sure of their stability. Table 10 contains the maximum differences of the magnitudes between seasons and in sigma units for the four concerned stars and also for the star "U".

On the basis of this analysis, we conclude that star "R" and star "V" are comparably stable. However, star "V" is closer to the lens system, and it is possible to use its shape as a reference PSF for the lens fitting. Also, it had been found to be photometrically stable by Sinachopoulos et al. [2001] and Nakos et al. [2003]; finally it was already used by Nakos et al. [2005] as a reference for the PSF fitting of UM673.

From all these considerations, we decided to use star "V" as the reference star for the PSF fitting of the lens system and the further normalization in magnitude of the light curves. Moreover, we calculated the R magnitude of the "G1" and "G2" galaxies with aperture photometry, using "V" as the reference star. We found values of $m_R = 17.47 \pm 0.03$ for "G1", and $m_R = 17.92 \pm 0.05$ for "G2".

We tested if it was possible, on the basis of our data, to reconstruct the lens galaxy "G" and to measure its magnitude. The test was carried out using the 44 best quality images in the R filter. Each image was interpolated with a bicubic spline and every pixel was divided in a grid of 10×10 new subpixels. Then we superposed these oversampled images and we summed them up to obtain an oversampled image with a high signal-to-noise ratio. The PSF fitting of this image showed that it was not possible to correctly and definitely reconstruct the lens galaxy due to its too small distance from the "B" component.

Then in the following analysis we considered the magnitude of the lens galaxy "G" in the different filters as those provided by HST[3], for instance we have $m_V = 20.81 \pm 0.02$, $m_R = 19.35 \pm 0.01$, and $m_I = 18.72 \pm 0.03$.

We applied the PSF fitting technique to account for the magnitude of the lens system on the best frames previously chosen, by applying the robust method already used in our previous work [Ricci et al., 2011c].

Our method is based on the simultaneous fit of each frame with three PSFs using bicubic interpolation: two for the components "A" and "B", and the third for the lens galaxy "G", fixing the relative astrometry between the components provided by Muñoz et al. [1998]. We then had four free parameters: the two spatial positions of the system with respect to the reference, and the amplitude of the two lensed components (as previously described, we fixed the amplitude of the lens galaxy with respect to the selected reference star).

Koptelova et al. [2010b] observed UM673 in the VRi filters, and obtained the photometry without taking separately into account the magnitude of the lens galaxy "G". As the lens galaxy is located very close to the "B" component, let us label as "B+G" the results relative to the "B" component obtained in this way.

As a complementary approach, we decided to apply our PSF fitting technique in the same way, to evaluate the differences in magnitude and in color of the two lensed components with respect to the results obtained as described above.

To normalize the magnitudes in the VRi filters, we used the values of the star "V" provided by Nakos et al. [2003]: $m_V = 16.54 \pm 0.01$, $m_R = 16.00 \pm 0.01$, and $m_I = 15.55 \pm 0.01$. Moreover, the R and i magnitudes are coherent with those provided by the USNO-B1 catalog.

3 http://www.cfa.harvard.edu/castles/Individual/Q0142.html

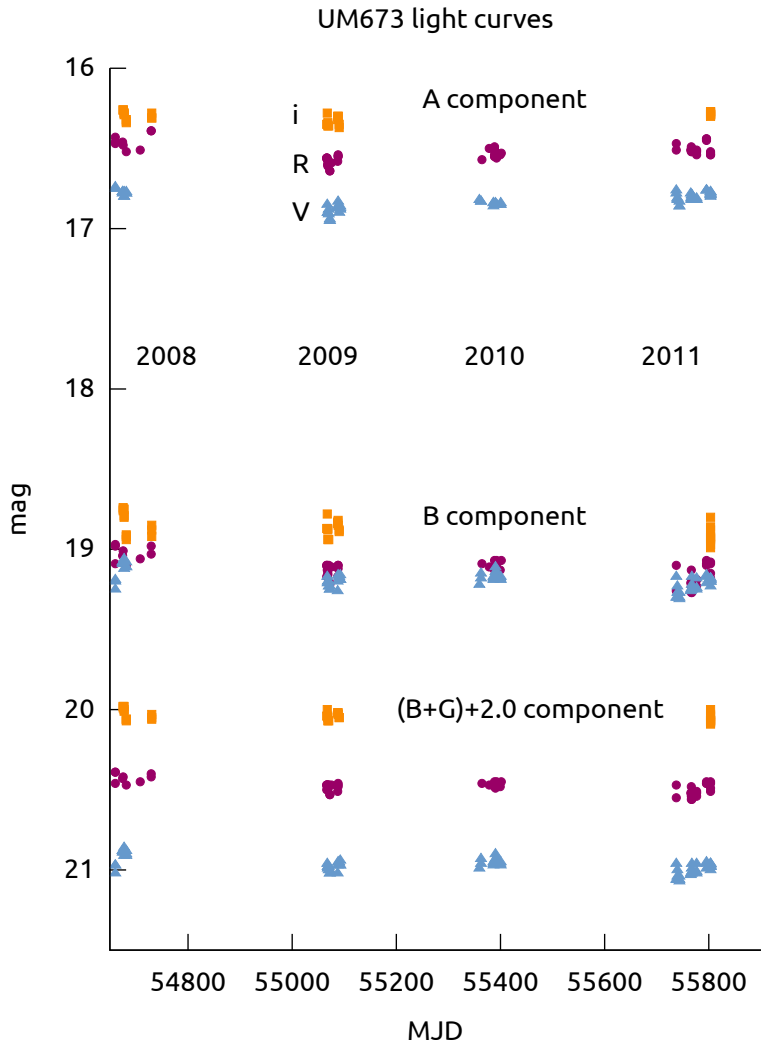

Figure 52: Light curves in the VRi filters of the two lensed components "A" and "B" of the gravitationally lensed quasar UM673. The plot also shows the "B+G" values, obtained by fitting the "B" component without separating the contribution of the lens galaxy "G". The "B+G" light curves have been shifted by 2 magnitudes.

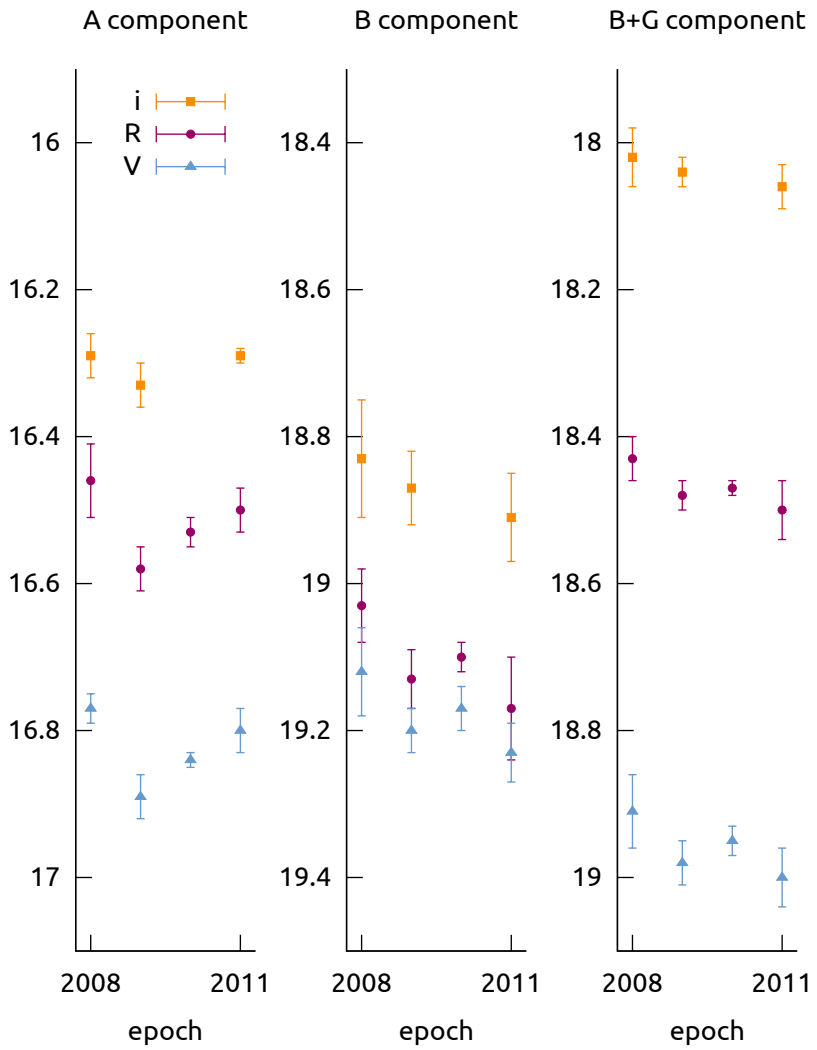

Figure 53: Average light curves over each epoch of observation of the two lensed components "A" and "B". The "B+G" average light curve is also shown. The error bars show the RMS of the average at the 1σ level.

Table 11: Average magnitude of the four observing seasons (2008–2011) for the gravitationally lensed components of UM673 in the VRi bands.

component	epoch	V	R	i
A	2008	16.77 ± 0.02	16.46 ± 0.05	16.29 ± 0.03
	2009	16.89 ± 0.03	16.58 ± 0.03	16.33 ± 0.03
	2010	16.84 ± 0.01	16.53 ± 0.02	
	2011	16.80 ± 0.03	16.50 ± 0.03	16.29 ± 0.01
B	2008	19.12 ± 0.06	19.03 ± 0.05	18.83 ± 0.08
	2009	19.20 ± 0.03	19.13 ± 0.04	18.87 ± 0.05
	2010	19.17 ± 0.03	19.10 ± 0.02	
	2011	19.23 ± 0.04	19.17 ± 0.07	18.91 ± 0.06
B+G	2008	18.91 ± 0.05	18.43 ± 0.03	18.02 ± 0.04
	2009	18.98 ± 0.03	18.48 ± 0.02	18.04 ± 0.02
	2010	18.95 ± 0.02	18.47 ± 0.01	
	2011	19.00 ± 0.04	18.50 ± 0.04	18.06 ± 0.03

7.4 Results

7.4.1 Flux variations

The separate light curves of the two lensed components "A" and "B" of UM673 and the "B+G" light curve are shown in Fig. 52. For a robust measurement of variability, we calculated the average and the rms over each season. The results are shown in Fig. 53 and in Table 11: we have an initial common behavior for the different filters and components: the magnitude slightly increases between the 2008 and the 2009 seasons, and decreases between the 2009 and the 2010 seasons. Then, during the 2011 season, the flux of the "A" component kept increasing, while the "B" component slightly decreased.

In particular, in the V filter we notice a decrease in flux by 0.12 magnitude between the 2008 and 2009 seasons for the "A" component (corresponding to a decrease of 4σ), and an increase in flux by 0.09 magnitude between the successive three seasons (2009–2011). The flux of the "B" lensed component, as well as of "B+G", slightly decreased in this filter over the four seasons.

In the R filter the behavior is the same: for the "A" component the flux decreased by 0.12 magnitude (above 3σ) between the first two seasons and successively increased by 0.08 magnitude between the 2009 and the 2011 seasons. The flux of the "B" lensed component decreased by 0.15 magnitude (3σ), while for "B+G" the behavior is less evident.

Table 12: Average $R-i$ and $V-R$ color indices of the four observing seasons (2008–2011) for the gravitationally lensed components of UM673.

component	epoch	$R-i$	$V-R$
A	2008	0.16 ± 0.05	0.31 ± 0.05
	2009	0.25 ± 0.04	0.31 ± 0.04
	2010		0.31 ± 0.03
	2011	0.22 ± 0.03	0.29 ± 0.04
B	2008	0.20 ± 0.09	0.09 ± 0.08
	2009	0.27 ± 0.06	0.07 ± 0.05
	2010		0.07 ± 0.04
	2011	0.26 ± 0.03	0.05 ± 0.08
B+G	2008	0.40 ± 0.05	0.49 ± 0.06
	2009	0.45 ± 0.03	0.50 ± 0.03
	2010		0.49 ± 0.03
	2011	0.45 ± 0.05	0.49 ± 0.05

Finally, in the i filter we notice the same trends as detected in the other filters but with a less significant amplitude.

7.4.2 Color variations

From the data collected during the 2008, 2009, and 2011 seasons, we are able to build a color-color diagram to inspect for color variations of the two lensed components and of "B+G" with time. The results are shown in Fig. 54 and in Table 12. We have a weak increase by 0.09 magnitude in the $R-i$ color index for the "A" lensed component between the first two seasons, while the $V-R$ color index remains stable. By the way, all our color variations are within the error bars. The "B" lensed component and "B+G" show smaller variations for both color indices.

Our results show that the color indices of the "B+G" component are coherent with the work of Koptelova et al. [2010b]. Moreover, the temporal evolution of the color index between the observations of Koptelova et al. [2010b] and the current data (see the arrows in Fig. 54) show a weak trend indicating that the quasar becomes redder as its magnitude increases, as already observed in our multi-color study of the gravitationally lensed quasar HE0435–1223 [Ricci et al., 2011c].

A result of this inspection is the difference in color observed between the two lensed components. We find that the "A" com-

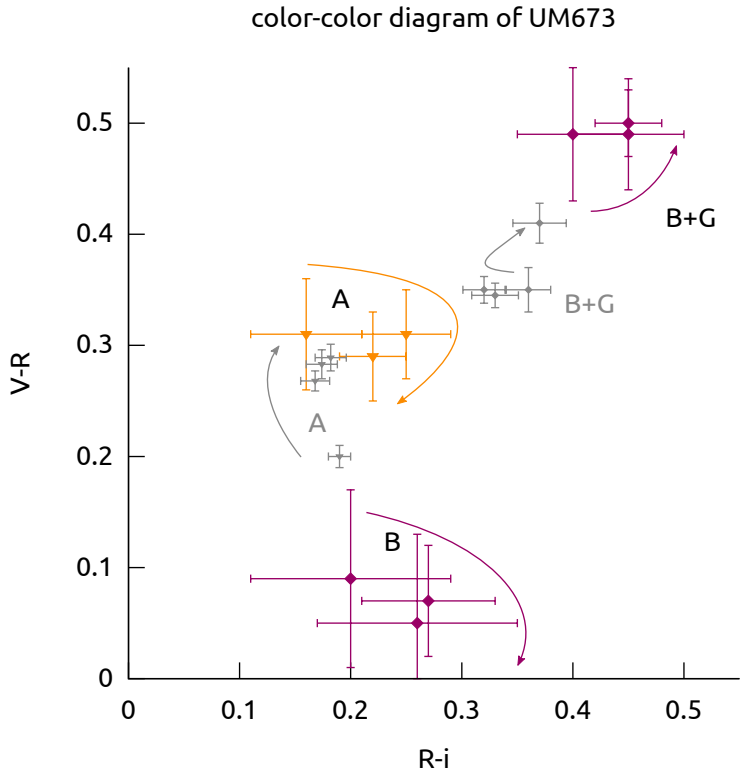

Figure 54: Color-color diagram of the two lensed components "A" and "B" of UM673. The "B+G" values are relative to the color indices of the "B" component obtained without separating the contribution of the lens galaxy, as in the approach of Koptelova et al. [2010b]. The arrows help to follow the evolution of the color index over the epochs. The smaller points, which also have smaller error bars are elaborated from the data provided by Koptelova et al. [2010b].

ponent has a $V-R$ color index larger by 0.23 magnitude than that of the "B" component.

On the basis of the difference in color between the two lensed components, we conclude that the "B" component is intrinsically bluer than the "A" component for what concerns the $V-R$ color index.

Several hypotheses for the explanation of this difference in the color index could be envisaged: an intrinsic variation of the quasar, a microlensing effect, the extinction operated by the deflector, and finally a chromatic differential amplification.

We can exclude the first two effects as current and previous observations [Koptelova et al., 2010b] do not show any evidence for such phenomena.

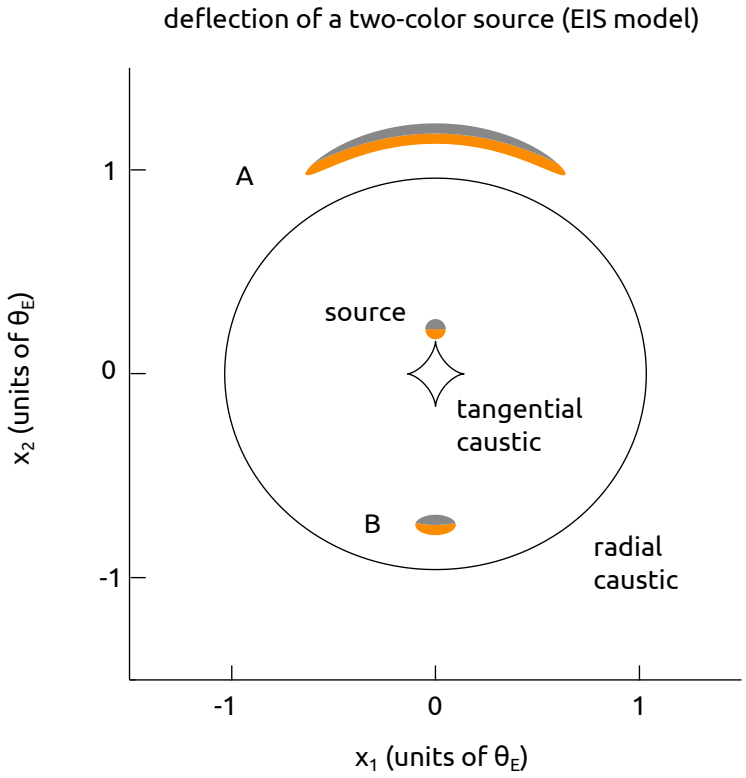

Figure 55: Illustration of the possible differential color amplification for the case of UM673. In this toy model, simulated by Olivier Wertz, a circular source is composed of two half hemispheres having different colors (gray and orange in this case). The source is placed close but slightly outside the upper cusp of the tangential caustics produced by an EIS deflector, following the configuration proposed by Surdej et al. [1988]. The source is gravitationally lensed in two images labeled "A" and "B", in analogy with the components of UM673. The magnitude difference between the two lensed components A and B turns out to be approximatively that observed for UM673 (2.1 magnitudes). The color difference between the two gray and orange lensed colored images is of the same order (0.2 magnitude) as that observed for the V-R color index of UM673 "A" and "B".

Koptelova et al. [2008], based on the measurements of Falco et al. [1999], suggested that the extinction of the lens galaxy [Cardelli et al., 1989, Jean and Surdej, 2007] could provide an explanation for the difference in color between the "A" lensed component and "B+G", redder. However, having removed the contribution of the lens galaxy from"B+G", we find that the "B" lensed component is bluer than "A".

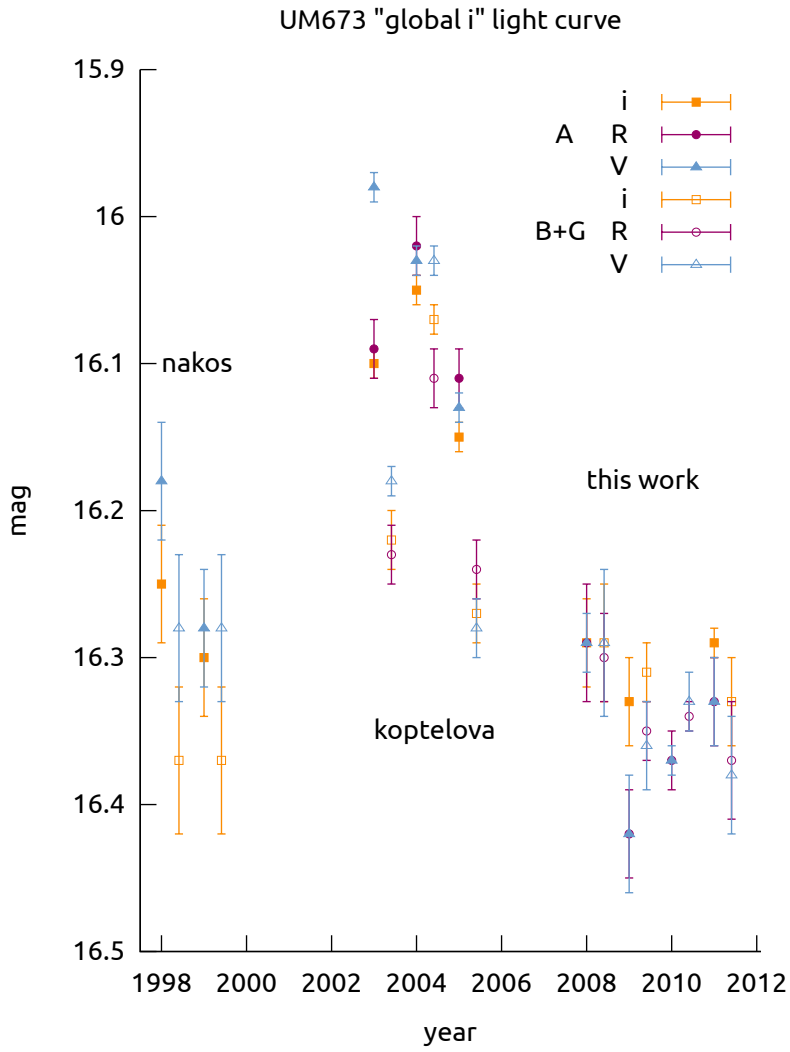

Figure 56: "Global i" light curve of UM673 built by embedding to our curves the data of Nakos et al. [2005] and Koptelova et al. [2010b]. In particular, Koptelova et al. [2010b] did not separate the contribution of the lens galaxy "G" from the lensed component "B" and we used here the same approach. The symbols follow the notation of Fig. 52. To construct the curve, we shifted the three curves relative to the "B+G" component (empty symbols) by correcting them for the time delay. Then, we calculated the three average 2008 differences in magnitude between "A" and "B+G", one for each filter, and we subtracted this value to the "B+G". Finally, we subtracted to the curves in the R and V filters their 2008 $V-R$ and $V-i$ color indices, respectively.

Instead, we suggest a possible differential color amplification as the source of differences observed in color between the two lensed components.

To illustrate such a possibility, we have made use of a toy model, simulated by Olivier Wertz, consisting of a circular source, divided in two half hemispheres having different colors (gray and orange in Fig. 55). The source has been placed near one of the cusps of the tangential caustics produced by an EIS lens model, in accordance with a possible configuration proposed by Surdej et al. [1988]. The resulting amplification (2.1 magnitudes) and color difference (0.2 magnitude) between the lensed gray and orange images are comparable to those observed for UM673 "A" and "B".

Indeed, as we may see in Fig. 55, the magnification (resulting in a flux amplification) of the two half gray and orange lensed images is not the same. In particular, the orange half source located closer to the cusp is more amplified than the other half (in gray).

A "global i" light curve which also includes the results of Nakos et al. [2005] (PSF fitting) and Koptelova et al. [2010b] is shown in Fig. 56. To construct this figure, first we shifted in time the light curve of the "B+G" component using the value of the time delay (150 days) provided by Koptelova et al. [2010b]. Then we calculated for each filter the average 2008 difference in magnitude between the two components, and we corrected the "B+G" light curve for these values. Finally, we corrected the V and R light curves of both components by their average 2008 $V - i$ and $R - i$ color indices, respectively. We chose the 2008 season as a reference only because it represents the beginning of our observations.

Fig. 56 shows that the flux of the quasar intrinsically varied over the seasons, with an amplitude of ≈ 0.4 magnitude, peak-to-valley over the last decade.

7.5 Conclusion

We presented a photometric monitoring, carried out during four epochs in three different filters, of the doubly imaged quasar UM673.

The results show a significant decrease in flux of the "A" lensed component between the first two seasons (2008–2009), and a smaller increase between the successive three seasons (2009–2011). This behavior is conspicuous in the V and R bands.

Our inspection also shows that the fainter "B" lensed component is intrinsically bluer than the brighter "A" lensed component.

We suggest that this difference in color observed between the two lensed components of UM673 might be due to a differential color amplification. Finally, our observations are in good agreement with the previous works carried out by Nakos et al. [2005] and Koptelova et al. [2010b].

Further observations could help in corroborating the separate color variations of the components and the slight trend observed between the seasons.

8 RXJ1131-1231

After having presented the results of the photometric studies of HE0435–1223 and UM673, we focus in this chapter on spectroscopic studies of the multiply imaged quasar[1] RXJ1131-1231.

We present a preliminary data reduction of multi-object spectroscopic observations, with a non-straight slit designed to embed up to three of the four lensed components.

We also provide a preliminary reduction concerning the forbidden [OIII] region, in particular concerning the two λ5007 and λ4959 emission lines.

In Sect. 8.1 we review some previous works on this object, and in Sect. 8.2 we describe the instrument and the peculiar slit that have been used. Then, in Sect. 8.3 we give a detailed description of the steps achieved during the pre-processing, while the preliminary data reduction is presented in Sects. 8.4.1, 8.4.2 and 8.4.3. Finally, in Sect. 8.5 we show preliminary results.

8.1 Previous observations

RXJ1131-1231 (see Fig. 57) is a multiply imaged quasar discovered by Sluse et al. [2003]. The source, located at $z_s = 0.658$ is lensed by an elliptical galaxy at $z_d = 0.295$. Sluse et al. [2003] modeled the lens with a SIS plus shear, detected magnitude variations in the V filter and provided an initial photometry.

In a further work, Sluse et al. [2006] obtained accurate astrometry of the four lensed components "A", "B", "C", and "D" as well as the astrometry of the lensing galaxy "G" and a nearby companion "X" using space-based HST NIC2 images and ground-based VLT observations (see Table. 13); the photometric observations revealed possible evidence for microlensing affecting the "A" lensed component.

A deep study of the lens model, as well the source reconstruction based on inverse ray tracing, was carried on by Claeskens et al. [2006]. The nature of the "X" object was associated with a satellite dwarf elliptical galaxy of the lens Galaxy "G", which was modeled adding an octupole to the Singular Isothermal Ellipsoid model with an external shear. Finally, the inverse ray

1 RA (J2000): 11:31:51.6, DEC (J2000): -12:31:57

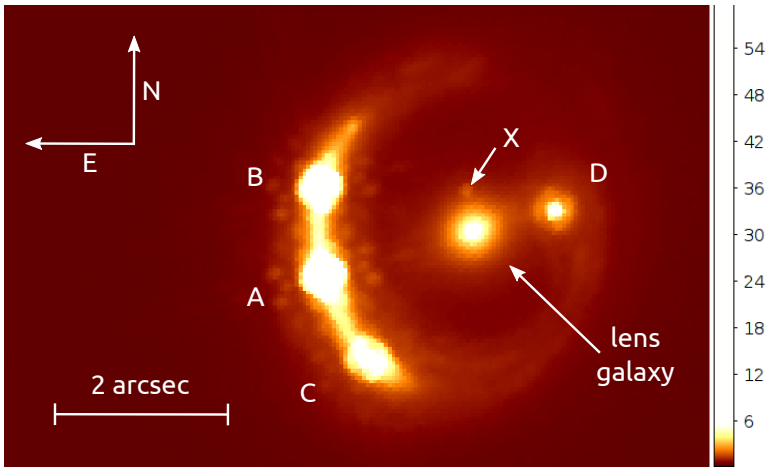

Figure 57: Image of RXJ1131-1231 taken with the Hubble Space telescope. The image was taken with the WFPC2 instrument using the F555W filter. Credits: The Hubble Legacy Archive.

tracing technique allowed to reconstruct the shape of the source and to identify it as a luminous Seyfert 1 spiral galaxy with a bluer central companion. This reconstruction was corroborated by the inverse ray tracing operated by Brewer and Lewis [2008].

A further long slit spectroscopic analysis by Sluse et al. [2007] revealed evidences for differential microlensing concerning the BELs (Broad Emission Lines), and allowed to investigate the quasar structure, and suggested integral field spectroscopy as a tool for a more detailed analysis of the lens system.

Sugai et al. [2007] studied the lens substructures using integral field spectroscopy observations carried on at the Subaru telescope, finding evidences of millilensing and microlensing occurring on the "C" lensed component, as well as minor microlensing effects on the Hβ line emitting region of the "A" component.

8.2 Instrument

Our observations were carried out with the FORS2 (FOcal Reducer and low dispersion Spectrograph) of the VLT (Very Large Telescope). The instrument is designed for the wavelength range from 330nm to 1100nm with a spatial resolution of 0.25″/pixel in the standard readout mode (2 × 2 binning).

FORS2 is installed on UT1 (Antu) and optimized for the red spectral band with a very low fringing thanks to a mosaic of two 2000 × 4000 CCDs (with a pixel size of 15µm). FORS2 has many modes, including multi-object spectroscopy with exchangeable

Table 13: Astrometry and V magnitude of RXJ1131-1231 as provided by Sluse et al. [2006] and Sluse et al. [2003], respectively.

	RA (arcsec)	DEC (arcsec)	V filter
A	$\equiv 0$	$\equiv 0$	17.97 ± 0.09
B	0.032 ± 0.001	1.184 ± 0.001	17.52 ± 0.10
C	-0.590 ± 0.001	-1.117 ± 0.001	18.59 ± 0.11
D	-3.115 ± 0.011	0.875 ± 0.001	20.11 ± 0.14
G	-2.027 ± 0.001	0.607 ± 0.001	18.40 ± 0.30
X	-1.936 ± 0.011	1.100 ± 0.011	18.40 ± 0.30

masks, long-slit spectroscopy, imaging and spectro-polarimetry and high-time resolution imaging and spectroscopy. Our observations were carried out in the multi-object spectroscopic mode.

The peculiarity of the observations is that a non-straight slit was used for RXJ1131-1231: the slit geometry is bent in such a way to embed the "B", "A" and "C" lensed components (see Fig. 58), as well as the part of the resolved Einstein ring in their proximities.

This type of slit produces on the two dimensional spectral image a pattern of banana-shaped emission and absorption lines, that requires a specific approach in the data reduction and in the further analysis.

8.3 Pre-processing

We collected 45 epochs of FORS2 observations distributed between 2008-04-03 and 2010-04-02 with a rate of 1–4 images per month when the object was observable (from December to July).

The observations were carried out with the GR600B, GR300V, GR600I, and GR600z grisms. In particular, we have:

- 78 images with the GR600B grism;
- 152 images with the GR300I grism;
- 34 images with the GR600I grism;
- 38 images with the GR600z grism;

for a total number of 302 spectra. We debiased and flat-fielded the science frames using the calibration images taken during the same nights. Whenever these calibration frames were not available, we paired the science frames with the closer bias or flat-field image.

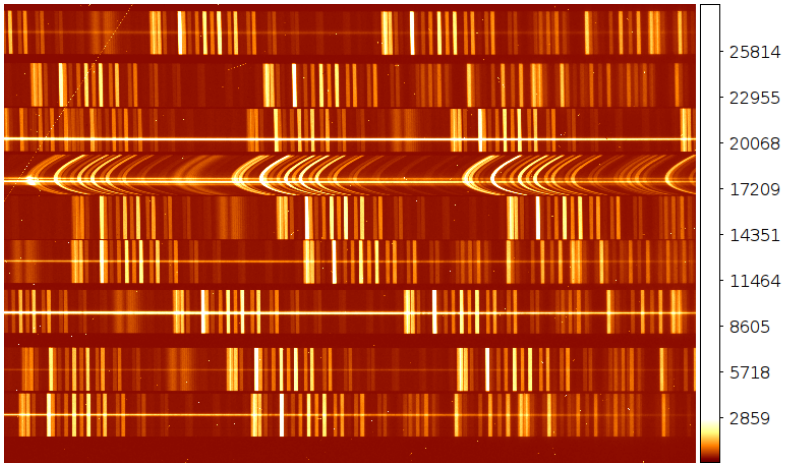

Figure 58: Zoom of a multi-spectral FORS2 science image of RXJ1131-1231. It is possible to see the bent emission and absorption lines of RXJ1131-1231 in the fourth row of the field. At the center of the bent zone, the traces of the "B", "A", and "C" lensed components are also visible. The other straight spectra correspond to other stars in the same field.

Finally, we extracted for each observation the zone relative to the RXJ1131-1231 spectrum as well as the same zone on the wavelength calibration image.

8.4 Data reduction

We based our reduction approach on the "quarklib" library developped by Pierre Guillaume Sprimont and written in the C++ programming language. This library was initially optimized for the treatment of other FORS2 multi-slit spectra in the framework of the XMM-LSS survey [Adami et al., 2011], and we adapted it to the treatment of the RXJ1131-1231 data. The peculiar approach to face the problem of the bent slit gave us the opportunity to redevelop the tasks in a more efficient way. A further implementation based on a TCP/IP "server/client" system, with multi-thread facilities and a modern web interface is currently in progress.

First of all we proceeded with the detection of the cosmic ray mask using the gradient of the science image. Tuning the parameters for this step is very important because it has a direct effect on the further steps.

Instead of considering each pixel of the image as a matrix element of a regular grid of pixels, we associate to each pixel a triplet of values (x_p, y_p, z), where x_p and y_p are the spectral and spatial coordinates in pixel units, and z are the counts. This

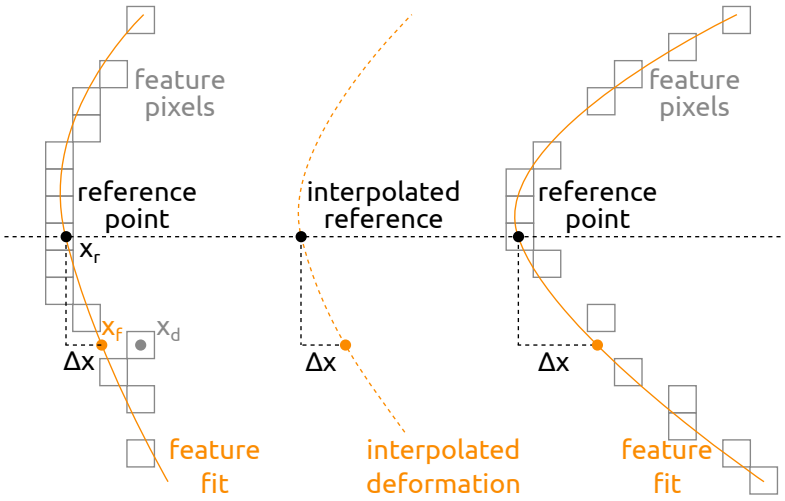

Figure 59: Detection and correction of the spatial deformation: the feature pixels (squares) of two subsequent features are fitted (solid curves), and the deformation between the features is interpolated (dashed curve). Then for every pixel having x_d spatial coordinate, we define $\Delta x = x_f - x_r$, that is to say the difference between the fitted deformation x_f and the fitted reference point x_r.

approach is useful while calculating the spatial deformation. Of course, at this step of the reduction, each pixel has integer values for the x_p and y_p coordinates.

8.4.1 Spatial deformation

The detection of the spatial deformation consists of the most complex step. The idea is to automatically detect the larger number of emission and absorption lines (that we also call "features").

To perform this operation, we calculate the gradient of the science image in the x direction, to get rid as much as possible of the contribution of three continuum traces, mostly horizontal. Then, with a two-step system of thresholds, we detect pixels which are associated between them in order to re-create the traces of the several features.

At this point, each detected feature (composed by several pixel elements still having each one integer x_p and y_p coordinates) is fitted using a polynomial or a spline, as shown in Fig. 59. Then, the deformation values for each pixel between two consecutive features is calculated via interpolation.

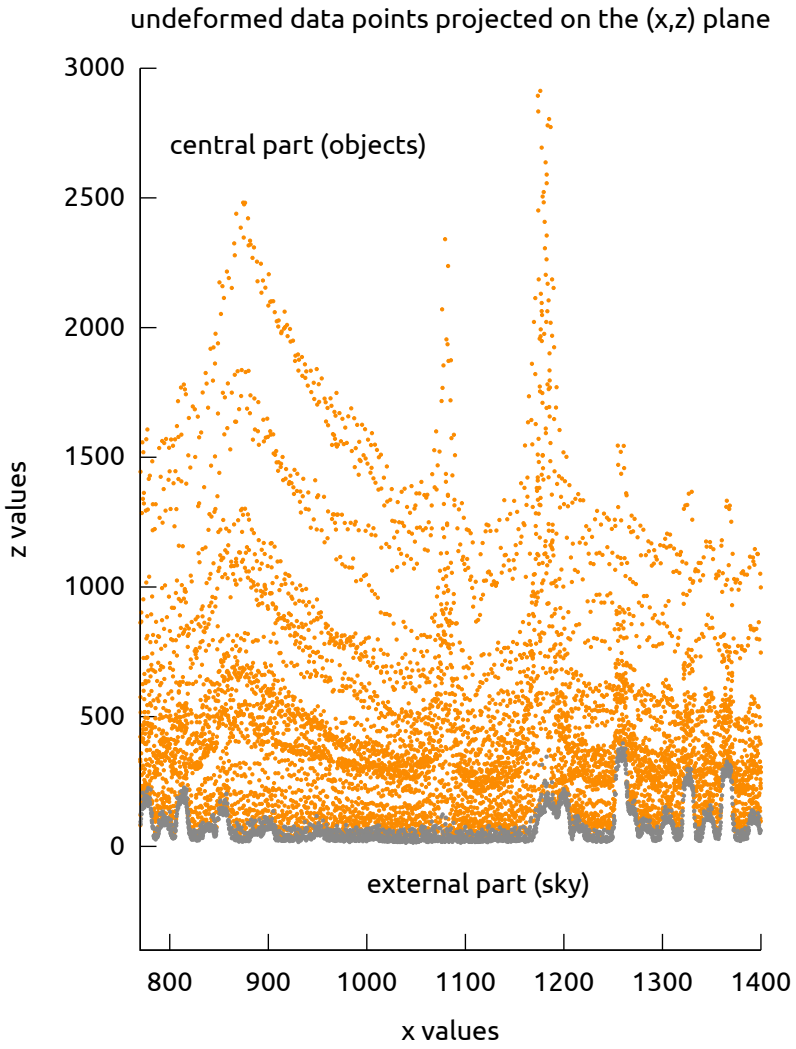

Figure 60: Data points projected on the (x, z) plane: the graph represents all the points of the spectrum corrected for the spatial deformation. We enhanced the external part points which contain mostly information related to the sky. The central part points contain the information relative to the three objects. The graph is zoomed on the [OIII] region.

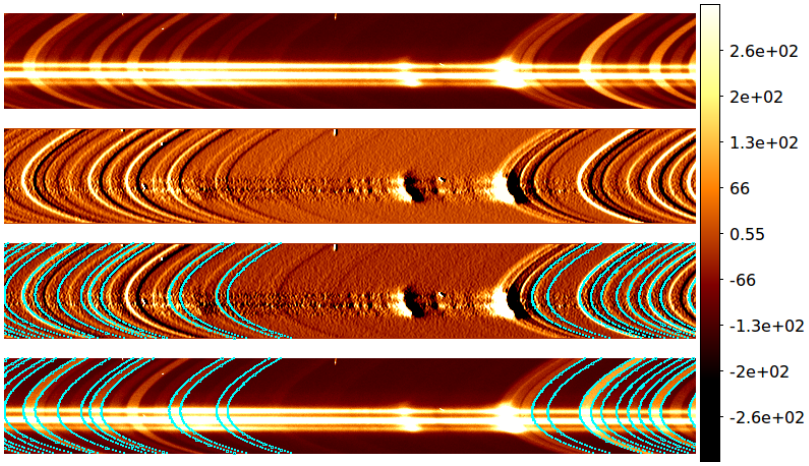

Figure 61: Example of feature detection for the determination of the spatial deformation. The upper image is a zoom on the [OIII] region of a FORS2 science frame taken with the GR600z grism. The image just below illustrates the gradient calculated along the x (spectral) direction. Just below, the features are detected on the gradient. The last image shows how the features are related to the science frame.

This operation provides for every pixel a correction Δx. Concerning the feature pixels, this Δx is the difference between an x_r reference point of the fit and the several x_f fitted coordinates relative to each x_p of the feature. Concerning the non feature pixels, the Δx is given by the interpolation (see again Fig. 59).

Once the spatial deformation is calculated and every x_p value is corrected for Δx, our regular grid of pixels having integer x_p and y_p coordinates does not exist anymore. The regular "pixels grid" idea is replaced by a more appropriate concept of "point cloud". If there was no spatial deformation or a very little spatial deformation, then the point cloud would have been regular or almost regular too. This can be seen by applying our technique to the spectrum image of a reference star, which had a straight slit.

A detail of the "pixel cloud" concept is easily visible in Fig. 60, while Fig. 61 shows an example of fit of the spatial deformation.

8.4.2 Sky fit and sky subtraction

The further step is the fit of the sky. Once having isolated the side zones where the sky is dominant, we model the features using a bidimensional spline with different degrees of freedom between the x spectral direction and the y spatial direction.

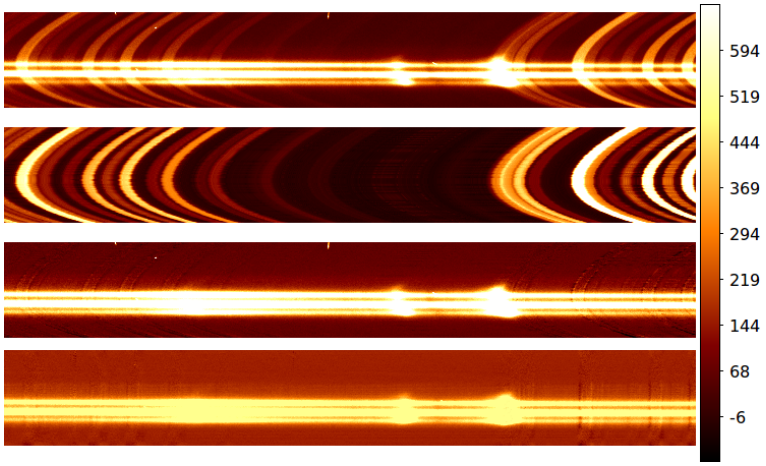

Figure 62: Example of sky modeling, sky subtraction and rebinned image. The upper image is a zoom on the [OIII] region of the same science frame taken with the GR600z grism as in Fig. 61. The image just below is a calculated model of the sky. Just below, an image after sky subtraction is presented. The last image shows an example of rebinned "undeformed" image, built to have a better idea of the results. This image is purely useful for a visual inspection, as the data reduction procedure is based on the idea of "point cloud" instead of considering a regular grid of pixels.

It is important to notice that the fit is done on the point cloud: due to the high deformation of the slit, high and fine Δx corrections are applied to each point, and the resulting cloud is well sampled and spread. This helps to have a very smooth sky subtraction while correcting the z values. An example of result for sky modeling and sky subtraction is shown in 62 (central images).

Another approach based on a bidimensional polynomial fit was tried, but the results were not satisfactory.

Finally, we tried to use the wavelength calibration image for a better detection of the spatial deformation and the deformation was found very easily thanks to the high signal to noise ratio. However, once we performed the sky subtraction, we had very high residuals. After several tests on several images and with different grisms, we concluded that, due to a possible displacement of the mask between the science image and the calibration image, the frames were not compatible in order to perform a good sky subtraction.

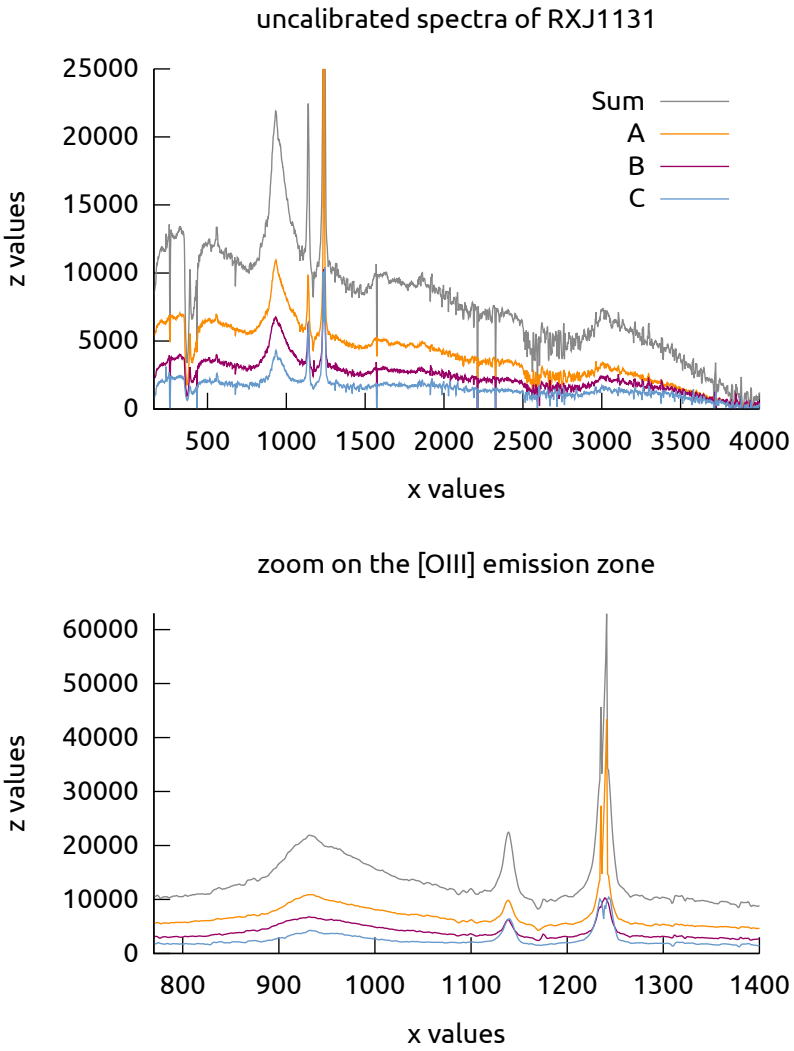

Figure 63: Example of an uncalibrated extracted spectra of RXJ1131-1231, before the subtraction of the continuum (upper graph). The Flux scale is truncated to enhance the faint features. A zoom on the high flux region is shown in zoom in the [OIII] region (lower graph). The zoom represents the same part of the spectrum as shown in Figs. 60, 61 and 62.

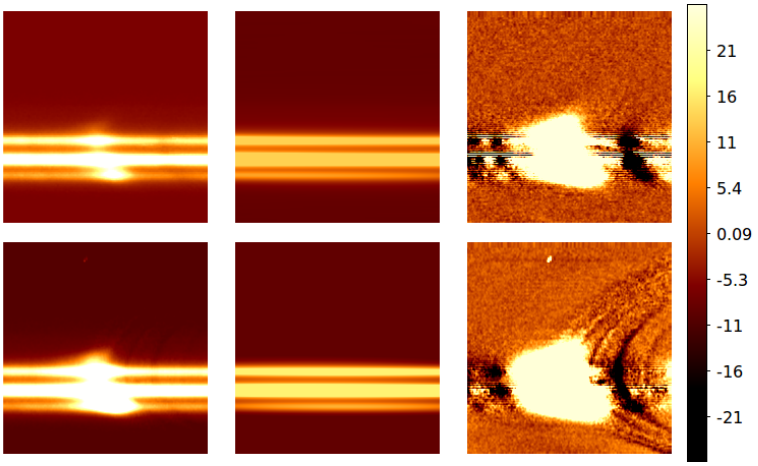

Figure 64: Subtraction of the continuum around the two emission regions. The left panels show the two regions relative to the [OIII] emission lines: λ5007 (lower) and λ4959 upper. The middle panels show the spline fitting of the continuum, while the right panels display the two regions after subtraction of the continuum.

8.4.3 Extraction of the spectra

The pipeline for the pre-processing, the cosmic ray masking, the spatial deformation detection, and the sky subtraction is solid but can be improved. The automation gives good results for most of the good seeing images, while the tuning is somehow difficult. A work to simplify the management of the several parameters and to treat separately the peculiar difficult images is in progress.

Concerning the extraction of the spectra and the calibration in flux and wavelength, specific pipeline tasks are already coded and operational, although the fine tuning to provide a fully automatic reduction has still to be terminated.

The extraction of the spectra is based on the concept of "sliding window". As the point cloud is not a regular grid, we select a spectral window within a given range (x_a, x_b), and we project the pixels on the (y, z) plane.

At this point, for an initial guess we fit three gaussians with seven free parameters: three centroid positions, three amplitudes, and one sigma. Then, we move the sliding window to select a spectral window in the range $(x_{a+\Delta a}, x_{b+\Delta b})$, and we repeat the procedure.

Once we have this initial guess, we proceed with a second finer fit and then with the extraction of the spectrum. An example of extracted spectra is given in Fig. 63.

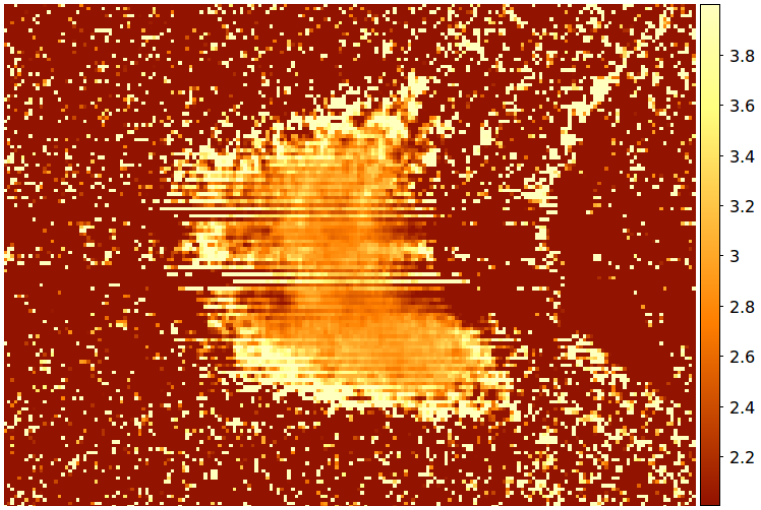

Figure 65: Ratio of the [OIII] spectral lines of RXJ1131-1231.

8.5 Preliminary results

As written in the previous section, the data reduction is still in progress, and in particular the steps relative to the flux and wavelength calibrations have to be done.

Despite this, we provide preliminary results concerning the forbidden [OIII] region, in particular concerning the two λ5007 and λ4959 emission lines. The theoretical intensity ratio between these emission lines, originating from the ionized NLR, can be mathematically calculated, and the results were recently updated [Dimitrijević et al., 2007] including relativistic effects, fixing the value at 2.98.

We chose the best seeing sky subtracted bidimensional images taken with the GR600z grism, and we averaged them after a 2×2 pixel oversampling and a recentering with an accuracy of one (new) pixel. Then we cut two regions around the two emission lines, we fitted the continuum and we subtracted it from each image (see Fig. 64).

Finally, we divided the region relative to the λ5007 emission line by the region relative to the λ4959 emission line.

The result is a two-dimensional ratio of the [OIII] spectral lines of the gravitationally lensed quasar shown in Fig. 65. The setup of a reduction technique to quantify this value (visibly around 3), and to compare it with the theoretical value is in progress.

9 Conclusions and perspectives

The present work gave an overview of the field of gravitational lensed quasars, focusing on the aspects relative to direct imaging, photometry and spectroscopy.

direct imaging: optical lenses and coronagraphy

First, we proposed to design a specific optical instrument, modeled in such a way that makes possible the inversion of gravitational lens effects. Direct imaging of the cosmic mirage could then take advantage from the magnification provided by the lensing galaxy, with a flux amplification, magnification and a resulting enhanced angular resolution. We provided the mathematical expressions of the surfaces of such optical instruments for the case of refraction and reflection.

These surfaces are related to particular lens models, and we also studied the surface that may account for the presence of an external shear. Preliminary optical tests were already performed in our institute, and we plan to develop this concept in the near future in the framework of the realization of a telescope instrument.

Such an instrument, once the inversion of the gravitational lens effects is performed, could be paired with a coronagraph device capable to mask the central bright source to inspect its immediate neighborhoods, enhancing eventual fainter features.

To complete this step, several coronagraph devices could be envisaged. In this work we decided to propose a new concept of coronagraph that implements the traditional Lyot coronagraph with the introduction of a dynamic (or adaptive) hologram in the optical scheme. The hologram provides the nulling of the residual speckle halo of the bright source, and improves the detection of the close fainter features.

We carried out a large number of numerical simulations under different conditions to test the validity of this concept, and we conclude that it is possible to override the current limits of coronagraphy improving the nulling performances by a factor 1 000–10 000. We also gave the limits to reach this goal in terms of magnitude and precision in the control of the "actuators" of the hologram. These results also include a discussion about a future practical implementation of the instrument.

This "extreme" cononagraphy technique will allow in the future the direct imaging of exo-earths (10^{-8}–10^{-10} times fainter

than their host star). The innovation of our study consisted in adding a further correction step (the hologram) after the coronagraph, and such studies are important to reach a sufficiently high nulling ($> 10^6$). Laboratory tests are required to refine this technique.

photometry of two gravitationally lensed quasars

In parallel to this work, we also obtained observational data during the photometric study of the multiply imaged quasars HE0435–1223 and UM673. We carried out multi-epoch observations of these objects in different optical bands, and we found for both these systems significant flux and color variations. We attribute such changes to a variation in the intrinsic luminosity of the quasar. In particular, HE0435–1223 also showed possible signatures of microlensing effects, while the changes in color of UM673 might be due to a differential color amplification.

Our observations put also in evidence that a good-sampled multi-band photometry can help in discriminating the nature of the variability of multiply imaged objects, in particular gravitationally lensed quasars.

spectroscopy: preliminary data reduction

Finally, we started the reduction of FORS2 spectroscopic data of the multiply imaged quasar RXJ1131-1231. The work is in a preliminary phase and we foresee the setup of a fully automated and modern software capable to overtake in quality and computing speed the actual software for the spectral analysis in general, and in particular for what concerns FORS2 multi-slit spectra of multiply imaged extragalactic objects.

A One-dimensional description

In this appendix we re-derive some of the already known mathematical solution (see the work of Refsdal and Surdej [1994]) concerning the shapes of the rotationally symmetrical surfaces of the optical gravitational lenses/mirrors for the SIS, PM and UD lens models (see Fig. 66), in analogy with the two-dimensional description given in Chap. 2.

a.1 Transparency

a.1.1 Singular isothermal sphere

$$M(x) = kx \tag{A.1}$$

$$\frac{dy}{dx} = \frac{-4G}{c^2(n-1)}\frac{kx}{x} = \frac{-4Gk}{c^2(n-1)} \tag{A.2}$$

$$\begin{aligned} y - y_0 &= \int_{x_0}^{x} \frac{-4Gk}{c^2(n-1)}\,dx' \\ &= \frac{-4Gk}{c^2(n-1)}(x - x_0) \end{aligned} \tag{A.3}$$

a.1.2 Point-mass lens

$$M(x) = M \tag{A.4}$$

$$\frac{dy}{dx} = \frac{-4G}{c^2(n-1)}\frac{M}{x} \tag{A.5}$$

$$\begin{aligned} y - y_0 &= \int_{x_0}^{x} \frac{-4GM}{c^2(n-1)}\frac{1}{x'}\,dx' \\ &= \frac{-4GM}{c^2(n-1)} \ln\left(\frac{x}{x_0}\right) \end{aligned} \tag{A.6}$$

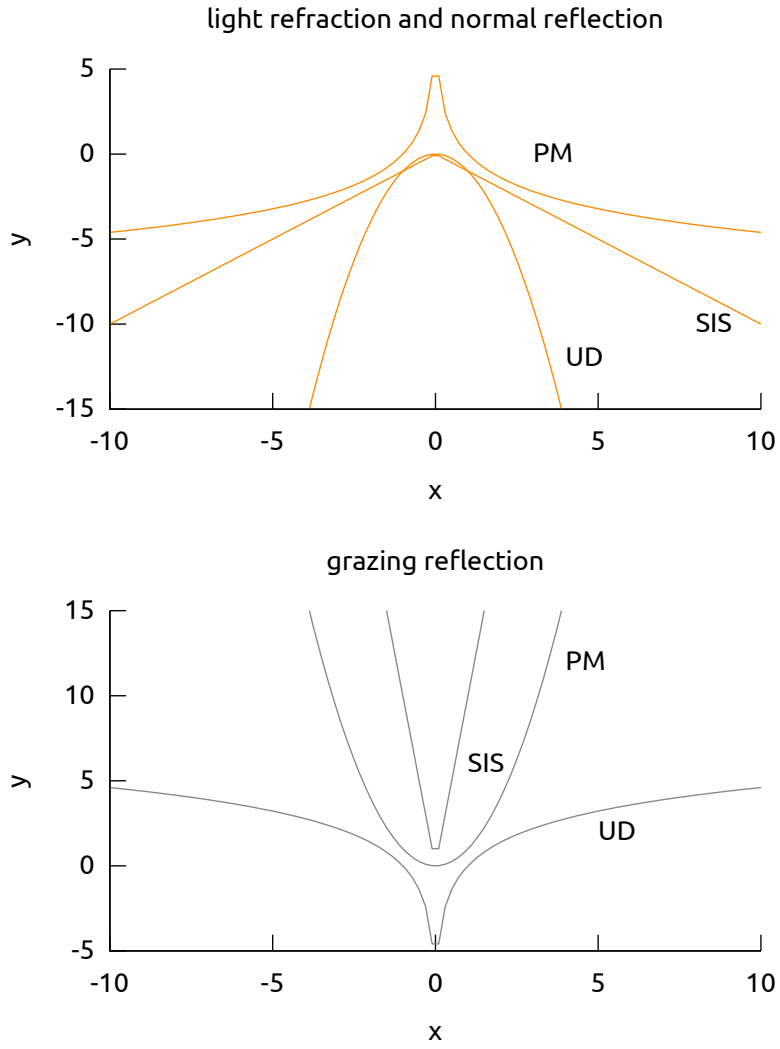

Figure 66: Shape of the surfaces corresponding to the SIS, PM and UD lens models.

a.1.3 Uniform disk

$$M(x) = \pi\Sigma_0 x^2 \tag{A.7}$$

$$\frac{dy}{dx} = \frac{-4G}{c^2(n-1)}\frac{\pi\Sigma_0 x^2}{x} = \frac{-4G}{c^2(n-1)}\pi\Sigma_0 x \tag{A.8}$$

$$\begin{aligned} y - y_0 &= \int_{x_0}^{x} \frac{-4G\pi\Sigma_0}{c^2(n-1)} x'\,dx' \\ &= \frac{-2G\pi\Sigma_0}{c^2(n-1)}(x^2 - x_0^2) \end{aligned} \tag{A.9}$$

a.2 Normal reflection

a.2.1 Singular isothermal sphere

$$M(x) = -kx \tag{A.10}$$

$$\frac{dy}{dx} = \frac{-4G}{2c^2}\frac{kx}{x} = \frac{-2Gk}{c^2} \tag{A.11}$$

$$\begin{aligned} y - y_0 &= \int_{x_0}^{x} \frac{-2Gk}{c^2}\,dx' \\ &= \frac{-2Gk}{c^2}(x - x_0) \end{aligned} \tag{A.12}$$

a.2.2 Point-mass lens

$$M(x) = M \tag{A.13}$$

$$\frac{dy}{dx} = \frac{-2G}{c^2}\frac{M}{x} \tag{A.14}$$

$$\begin{aligned} y - y_0 &= \int_{x_0}^{x} \frac{-2GM}{c^2}\frac{1}{x'}\,dx' \\ &= \frac{-2GM}{c^2}\ln\left(\frac{x}{x_0}\right) \end{aligned} \tag{A.15}$$

a.2.3 Uniform disk

$$M(x) = \pi\Sigma_0 x^2 \tag{A.16}$$

$$\frac{dy}{dx} = \frac{-2G}{c^2}\frac{\pi\Sigma_0 x^2}{x} = \frac{-2G}{c^2}\pi\Sigma_0 x \tag{A.17}$$

$$\begin{aligned} y - y_0 &= \int_{x_0}^{x} \frac{-2G\pi\Sigma_0}{c^2} x'\,dx' \\ &= \frac{-G\pi\Sigma_0}{c^2}(x^2 - x_0^2) \end{aligned} \tag{A.18}$$

a.3 Grazing reflection

a.3.1 Singular isothermal sphere

$$M(x) = -kx \tag{A.19}$$

$$\frac{dy}{dx} = \frac{c^2}{2G}\frac{x}{kx} = \frac{c^2}{2Gk} \tag{A.20}$$

$$\begin{aligned} y - y_0 &= \int_{x_0}^{x} \frac{c^2}{2Gk}\,dx' \\ &= \frac{c^2}{2Gk}(x - x_0) \end{aligned} \tag{A.21}$$

a.3.2 Point-mass lens

$$M(x) = M \tag{A.22}$$

$$\frac{dy}{dx} = \frac{c^2}{2G}\frac{x}{M} \tag{A.23}$$

$$\begin{aligned} y - y_0 &= \int_{x_0}^{x} \frac{c^2}{2GM} x'\,dx' \\ &= \frac{c^2}{4GM}(x^2 - x_0^2) \end{aligned} \tag{A.24}$$

a.3.3 Uniform disk

$$M(x) = \pi\Sigma_0 x^2 \tag{A.25}$$

$$\frac{dy}{dx} = \frac{c^2}{2G}\frac{x}{\pi\Sigma_0 x^2} = \frac{c^2}{2G}\frac{1}{\pi\Sigma_0 x} \tag{A.26}$$

$$\begin{aligned} y - y_0 &= \int_{x_0}^{x} \frac{c^2}{2G\pi\Sigma_0}\frac{1}{x'}\,dx' \\ &= \frac{c^2}{2G\pi\Sigma_0}\ln\left(\frac{x}{x_0}\right) \end{aligned} \tag{A.27}$$

B Bulge microlensing

In this appendix we briefly present the current results and publications concerning the systematic anomaly monitoring of bulge microlensing events. A summary of these publications may be found at pag. 154.

The MiNDSTEp consortium has adopted a three-step strategy of survey, follow-up, and anomaly monitoring of several microlensing events mainly in the bulge, but also in the Magellanic Clouds, with the aim of identifying planetary signals.

The first step is based on the prompt alerts of the microlensing surveys such as OGLE and MOA. Concerning the other two steps, the campaign makes use of the innovative approach by ARTEMiS (Automated Robotic Terrestrial Exoplanet Microlensing Search) for a fully-deterministic selection of targets [Dominik et al., 2010b], and moreover by profiting from online internet tools for visualizing in real-time the acquired data.

During these first four years of observation (2008–2011) we personally monitored hundreds of bulge events switching every 2–3 minutes between the targets proposed by an automatic software based on the OGLE and MOA surveys. When an anomaly was detected, an alert proposes to the software to re-design the target list in order to increase the sampling during the anomaly to check whether the deviation from the standard curve represented a possible signature of a planetary feature. This automatic and deterministic approach gave interesting results either for the detection of binary systems [Shin et al., 2011] and most of all for the detection of planets [Gould et al., 2010] , in particular for the following targets:

- MOA-2009-BLG-266LB: a cold 10 earth mass planet [Muraki et al., 2011];
- MOA-2009-BLG-319LB: a sub-saturn mass planet Miyake et al. [2011];
- OGLE-2009-BLG-092/MOA-2009-BLG-137: Ryu et al. [2010];
- OGLE 2008-BLG-290, an event that made possible an accurate limb darkening measurement Fouqué et al. [2010];
- MOA-2009-BLG-387LB: a massive planet orbiting an M dwarf [Batista et al., 2011a,b].

C Planetary transits

In this appendix we briefly describe the planetary transit parallel project of the MiNDSTEp campaign. We collaborated to these observations during the first four years 2008–2011, personally covering most of the transits whose results have been already published. A summary of these publications may be found at pag. 155).

The light curves are obtained with the telescope significantly defocussed and exposure times of 60–120s, so that the PSF of the star is spread over 20–30px (8–12″). This allows to achieve a signal-to-noise ratio particularly high for the following reasons:

- a smaller fraction of the time is used for CCD readout (typically 30–50s for the Danish CCD in windowed mode), so we have lower photon and scintillation noises;
- the flat-fielding errors are averaged down and the flat-field becomes a non-critical issue.

The average scatter in the light curves is generally below 1mmag RMS, and in the best case has reached 0.42mmag.

Other advantages of using the Danish telescope and the DFOSC instrument for this project are that the telescope is equatorially mounted (the light path through the telescope and instrument does not change whilst tracking an object), and the autoguider can be kept in focus whilst DFOSC is defocussed. Finally, the large DFOSC field of view allows to operate a good compromise between the readout time in windowed mode and the inclusion of several reference stars near the target.

Data from the project have been recently published in five papers in refereed journals:

- WASP-5 [Southworth et al., 2009d,e], WASP-4 [Southworth et al., 2009a,b] and WASP-2 [Southworth et al., 2010b, 2011c]: these objects were used to confirm the validity of the defocussed photometry technique;
- WASP-7 [Southworth et al., 2011a,b] was found to have a much lower density with respect to the data in the literature;

- WASP-18 [Southworth et al., 2009c, 2010a] is an extremely short-period (< 1 day). We observed both transit (planet in front of the star) and occultation (planet behind the star),
- WASP-17 (the least dense transiting planet known); WASP-15, WASP-16, WASP-24, WASP-25, WASP-28 and WASP-29; WASP-30 (a 60-Jupiter-mass brown dwarf) were also observed.

In addition to these objects, other targets were also observed with the new Lucky Camera, to test the performances of this instrument that aim to replace the DFOSC as the standard instrument for photometry.

The Lucky Camera is a new concept of photometric camera which is able to take up to 30 images per second, disregard the fraction of them which have a poor quality, correct for the centroid position of each image, and then sum up the frames to obtain a high seeing image with a tremendous gain with respect to the traditional cameras.

In particular, we observed with the Lucky Camera the exoplanet GJ 1214; and the hot Jupiter QATAR-2 [Bryan et al., 2011] with its second massive companion in an outer orbit.

Bibliography

C. Adami, A. Mazure, M. Pierre, P. G. Sprimont, C. Libbrecht, F. Pacaud, N. Clerc, T. Sadibekova, J. Surdej, B. Altieri, P. A. Duc, G. Galaz, A. Gueguen, L. Guennou, G. Hertling, O. Ilbert, J. P. Le Fèvre, H. Quintana, I. Valtchanov, J. P. Willis, M. Akiyama, H. Aussel, L. Chiappetti, A. Detal, B. Garilli, V. Lebrun, O. Lefèvre, D. Maccagni, J. B. Melin, T. J. Ponman, D. Ricci, and L. Tresse. The XMM-LSS survey: optical assessment and properties of different X-ray selected cluster classes. A&A, 526:A18+, February 2011. doi: 10.1051/0004-6361/201015182. (Cited on pages 110 and 155.)

C. Aime, R. Soummer, and A. Ferrari. Total coronagraphic extinction of rectangular apertures using linear prolate apodizations. A&A, 389:334–344, jul 2002. doi: 10.1051/0004-6361:20020419. (Cited on page 34.)

C. Alard. Image subtraction with non-constant kernel solutions. *ArXiv Astrophysics e-prints*, March 1999. (Cited on page 71.)

C. Alard. Image subtraction using a space-varying kernel. A&AS, 144:363–370, June 2000. doi: 10.1051/aas:2000214. (Cited on page 71.)

T. Anguita, R. W. Schmidt, E. L. Turner, J. Wambsganss, R. L. Webster, K. A. Loomis, D. Long, and R. McMillan. The multiple quasar Q2237+0305 under a microlensing caustic. A&A, 480:327–334, March 2008. doi: 10.1051/0004-6361:20078221. (Cited on page 75.)

R. Antonucci. Unified models for active galactic nuclei and quasars. ARA&A, 31:473–521, 1993. doi: 10.1146/annurev.aa.31.090193.002353. (Cited on page 3.)

N. Bate. Modelling anomalous lensed quasars. In *Manchester Microlensing Conference*, 2008. (Cited on page 75.)

N. F. Bate, D. J. E. Floyd, R. L. Webster, and J. S. B. Wyithe. A microlensing study of the accretion disc in the quasar MG 0414+0534. MNRAS, 391:1955–1960, December 2008. doi: 10.1111/j.1365-2966.2008.14020.x. (Cited on page 75.)

V. Batista, A. Gould, S. Dieters, S. Dong, I. Bond, J. P. Beaulieu, D. Maoz, B. Monard, G. W. Christie, J. McCormick, M. D.

Albrow, K. Horne, Y. Tsapras, M. J. Burgdorf, S. Calchi Novati, J. Skottfelt, J. Caldwell, S. Kozłowski, D. Kubas, B. S. Gaudi, C. Han, D. P. Bennett, J. An, The MOA Collaboration, F. Abe, C. S. Botzler, D. Douchin, M. Freeman, A. Fukui, K. Furusawa, J. B. Hearnshaw, S. Hosaka, Y. Itow, K. Kamiya, P. M. Kilmartin, A. Korpela, W. Lin, C. H. Ling, B. S. Makita, K. Masuda, Y. Matsubara, N. Miyake, Y. Muraki, M. Nagaya, K. Nishimoto, K. Ohnishi, T. Okumura, Y. C. Perrott, N. Rattenbury, T. Saito, D. J. Sullivan, T. Sumi, W. L. Sweatman, P. J. Tristram, E. von Seggern, P. C. M. Yock, The PLANET Collaboration, S. Brillant, J. J. Calitz, A. Cassan, A. Cole, K. Cook, C. Coutures, D. Dominis Prester, J. Donatowicz, J. Greenhill, M. Hoffman, F. Jablonski, S. R. Kane, N. Kains, J.-B. Marquette, R. Martin, E. Martioli, P. Meintjes, J. Menzies, E. Pedretti, K. Pollard, K. C. Sahu, C. Vinter, J. Wambsganss, R. Watson, A. Williams, M. Zub, The FUN Collaboration, W. Allen, G. Bolt, M. Bos, D. L. DePoy, J. Drummond, J. D. Eastman, A. Gal-Yam, E. Gorbikov, D. Higgins, J. Janczak, S. Kaspi, C.-U. Lee, F. Mallia, A. Maury, L. A. G. Monard, D. Moorhouse, N. Morgan, T. Natusch, E. O. Ofek, B.-G. Park, R. W. Pogge, D. Polishook, R. Santallo, A. Shporer, O. Spector, G. Thornley, J. C. Yee, The MiNDSTEp Consortium, V. Bozza, P. Browne, M. Dominik, S. Dreizler, F. Finet, M. Glitrup, F. Grundahl, K. Harpsøe, F. V. Hessman, T. C. Hinse, M. Hundertmark, U. G. Jørgensen, C. Liebig, G. Maier, L. Mancini, M. Mathiasen, S. Rahvar, D. Ricci, G. Scarpetta, J. Southworth, J. Surdej, F. Zimmer, The RoboNet Collaboration, A. Allan, D. M. Bramich, C. Snodgrass, I. A. Steele, and R. A. Street. MOA-2009-BLG-387Lb: a massive planet orbiting an M dwarf. A&A, 529:A102+, May 2011a. doi: 10.1051/0004-6361/201016111. (Cited on pages 127 and 154.)

V. Batista, A. Gould, S. Dieters, S. Dong, I. Bond, J. P. Beaulieu, D. Maoz, B. Monard, G. W. Christie, J. McCormick, M. D. Albrow, K. Horne, Y. Tsapras, M. J. Burgdorf, S. Calchi Novati, J. Skottfelt, J. Caldwell, S. Kozlowski, D. Kubas, B. S. Gaudi, C. Han, D. P. Bennett1, J. An, F. Abe, C. S. Botzler, D. Douchin, M. Freeman, A. Fukui, K. Furusawa, J. B. Hearnshaw, S. Hosaka, Y. Itow, K. Kamiya, P. M. Kilmartin, A. Korpela, W. Lin, C. H. Ling, S. Makita, K. Masuda, Y. Matsubara, N. Miyake, Y. Muraki, M. Nagaya, K. Nishimoto, K. Ohnishi, T. Okumura, Y. C. Perrott, N. Rattenbury, T. Saito, D. J. Sullivan, T. Sumi, W. L. Sweatman, P. J. Tristram, E. von Seggern, Yock P. C. M., MOA Collaboration, S. Brillant, J. J. Calitz, A. Cassan, A. Cole, K. Cook, C. Coutures, D. Dominis Prester,

J. Donatowicz, J. Greenhill, M. Hoffman, F. Jablonski, S. R. Kane, N. Kains, J.-B. Marquette, R. Martin, E. Martioli, P. Meintjes, J. Menzies, E. Pedretti, K. Pollard, K. C. Sahu, C. Vinter, J. Wambsganss, R. Watson, A. Williams, M. Zub, PLANET Collaboration, W. Allen, G. Bolt, M. Bos, D. L. DePoy, J. Drummond, J. D. Eastman, A. Gal-Yam, E. Gorbikov, D. Higgins, J. Janczak, S. Kaspi, C.-U. Lee, F. Mallia, A. Maury, L. A. G. Monard, D. Moorhouse, N. Morgan, T. Natusch, E. O. Ofek, B.-G. Park, R. W. Pogge, D. Polishook, R. Santallo, A. Shporer, O. Spector, G. Thornley, J. C. Yee, μ Collaboration, V. Bozza, P. Browne, M. Dominik, S. Dreizler, F. Finet, M. Glitrup, F. Grundah, K. Harpsoe, F. V. Hessman, T. C. Hinse, M. Hundertmark, U. G. Jorgensen, C. Liebig, G. Maier, L. Mancini, M. Mathiasen, S. Rahvar, D. Ricci, G. Scarpetta, J. Southworth, J. Surdej, and F. Zimmer. MOA-2007-BLG-387Lb light curve I band (Batista+, 2011). *VizieR Online Data Catalog*, 352:99102–+, April 2011b. (Cited on page 127.)

J. A. Blackburne and C. S. Kochanek. The Effect of a Time-varying Accretion Disk Size on Quasar Microlensing Light Curves. ApJ, 718:1079–1084, August 2010. doi: 10.1088/0004-637X/718/2/1079. (Cited on page 74.)

J. A. Blackburne, D. Pooley, S. Rappaport, and P. L. Schechter. Sizes and Temperature Profiles of Quasar Accretion Disks from Chromatic Microlensing. *ArXiv e-prints*, July 2010. (Cited on page 74.)

B. J. Brewer and G. F. Lewis. Unlensing HST observations of the Einstein ring 1RXS J1131-1231: a Bayesian analysis. MNRAS, 390:39–48, October 2008. doi: 10.1111/j.1365-2966.2008.13715.x. (Cited on page 108.)

M. L. Bryan, K. A. Alsubai, D. W. Latham, N. R. Parley, A. Collier Cameron, S. N. Quinn, J. A. Carter, B. J. Fulton, P. Berlind, W. R. Brown, L. A. Buchhave, M. L. Calkins, G. A. Esquerdo, G. Furesz, U. Grae Jorgensen, K. D. Horne, R. P. Stefanik, R. A. Street, G. Torres, R. G. West, M. Dominik, K. B. W. Harpsoe, C. Liebig, S. Calchi Novati, D. Ricci, and J. F. Skottfelt. Qatar-2: A K dwarf orbited by a transiting hot Jupiter and a more massive companion in an outer orbit. *ArXiv e-prints*, October 2011. (Cited on pages 130 and 155.)

J. A. Cardelli, G. C. Clayton, and J. S. Mathis. The relationship between infrared, optical, and ultraviolet extinction. ApJ, 345:245–256, October 1989. doi: 10.1086/167900. (Cited on page 103.)

B. W. Carroll and D. A. Ostlie. *An Introduction to Modern Astrophysics*. Weber State University, 1996. (Cited on page 3.)

J.-F. Claeskens and J. Surdej. Gravitational lensing in quasar samples. *Astronomy and Astrophysics Reviews*, 10:263–311, 2002. doi: 10.1007/s001590000010. (Cited on page 12.)

J.-F. Claeskens, D. Sluse, P. Riaud, and J. Surdej. Multi wavelength study of the gravitational lens system RXS J1131-1231. II. Lens model and source reconstruction. A&A, 451:865–879, June 2006. doi: 10.1051/0004-6361:20054352. (Cited on pages 5, 30, and 107.)

J.F. Claeskens. *Aspects statistiques du phénomène de lentille gravitationnelle dans un échantillon de quasars très lumineux*. Bulletin de la Société Royale des Sciences de Liège. Univ., 1999. URL http://books.google.com/books?id=lPwlMwAACAAJ. (Cited on page 23.)

J. L. Codona and R. Angel. Imaging Extrasolar Planets by Stellar Halo Suppression in Separately Corrected Color Bands. ApJ, 604:L117–L120, apr 2004. doi: 10.1086/383569. (Cited on page 35.)

F. Courbin, V. Chantry, Y. Revaz, D. Sluse, C. Faure, M. Tewes, E. Eulaers, M. Koleva, I. Asfandiyarov, S. Dye, P. Magain, H. van Winckel, J. Coles, P. Saha, M. Ibrahimov, and G. Meylan. COSMOGRAIL: the COSmological MOnitoring of GRAvItational Lenses IX. Time delays and N-body realisations of the lens in HE 0435-1223. *ArXiv e-prints*, September 2010. (Cited on pages 75 and 88.)

G. Daulie, O. Hainaut, D. Hutsemekers, P. Magain, M. Remy, A. Smette, J. Surdej, and E. van Drom. The relative photometric lightcurve of UM673 A&B. In J. Surdej, D. Fraipont-Caro, E. Gosset, S. Refsdal, & M. Remy, editor, *Liege International Astrophysical Colloquia*, volume 31 of *Liege International Astrophysical Colloquia*, pages 181–+, 1993. (Cited on page 91.)

M. S. Dimitrijević, L. Č. Popović, J. Kovačević, M. Dačić, and D. Ilić. The flux ratio of the [OIII] λλ5007, 4959 lines in AGN: comparison with theoretical calculations. MNRAS, 374:1181–1184, January 2007. doi: 10.1111/j.1365-2966.2006.11238.x. (Cited on page 117.)

M. Dominik, U. G. Jørgensen, N. J. Rattenbury, M. Mathiasen, T. C. Hinse, S. Calchi Novati, K. Harpsøe, V. Bozza, T. Anguita,

M. J. Burgdorf, K. Horne, M. Hundertmark, E. Kerins, P. Kjærgaard, C. Liebig, L. Mancini, G. Masi, S. Rahvar, D. Ricci, G. Scarpetta, C. Snodgrass, J. Southworth, R. A. Street, J. Surdej, C. C. Thöne, Y. Tsapras, J. Wambsganss, and M. Zub. Realisation of a fully-deterministic microlensing observing strategy for inferring planet populations. *Astronomische Nachrichten*, 331:671–+, July 2010a. doi: 10.1002/asna.201011400. (Cited on page 65.)

M. Dominik, U. G. Jørgensen, N. J. Rattenbury, M. Mathiasen, T. C. Hinse, S. Calchi Novati, K. Harpsøe, V. Bozza, T. Anguita, M. J. Burgdorf, K. Horne, M. Hundertmark, E. Kerins, P. Kjærgaard, C. Liebig, L. Mancini, G. Masi, S. Rahvar, D. Ricci, G. Scarpetta, C. Snodgrass, J. Southworth, R. A. Street, J. Surdej, C. C. Thöne, Y. Tsapras, J. Wambsganss, and M. Zub. Realisation of a fully-deterministic microlensing observing strategy for inferring planet populations. *Astronomische Nachrichten*, 331:671–+, July 2010b. doi: 10.1002/asna.201011400. (Cited on pages 127 and 154.)

A. Einstein. Die Feldgleichungen der Gravitation (The Field Equations of Gravitation). *Koniglich Preussische Akademie der Wissenschaften*, pages 844–847, 1915. (Cited on page 11.)

R. Fadely and C. R. Keeton. Near-infrared K and L' Flux Ratios in Six Lensed Quasars. AJ, 141:101, March 2011. doi: 10.1088/0004-6256/141/3/101. (Cited on page 92.)

E. E. Falco, C. D. Impey, C. S. Kochanek, J. Lehár, B. A. McLeod, H.-W. Rix, C. R. Keeton, J. A. Muñoz, and C. Y. Peng. Dust and Extinction Curves in Galaxies with $z > 0$: The Interstellar Medium of Gravitational Lens Galaxies. ApJ, 523:617–632, October 1999. doi: 10.1086/307758. (Cited on page 103.)

D. J. E. Floyd, N. F. Bate, and R. L. Webster. Probing the emitting region using anomalous lensed QSOs. Mem. Soc. Astron. Italiana, 79:1271–+, 2008. (Cited on page 75.)

P. Fouqué, D. Heyrovský, S. Dong, A. Gould, A. Udalski, M. D. Albrow, V. Batista, J.-P. Beaulieu, D. P. Bennett, I. A. Bond, D. M. Bramich, S. Calchi Novati, A. Cassan, C. Coutures, S. Dieters, M. Dominik, D. Dominis Prester, J. Greenhill, K. Horne, U. G. Jørgensen, S. Kozłowski, D. Kubas, C.-H. Lee, J.-B. Marquette, M. Mathiasen, J. Menzies, L. A. G. Monard, S. Nishiyama, I. Papadakis, R. Street, T. Sumi, A. Williams, J. C. Yee, S. Brillant, J. A. R. Caldwell, A. Cole, K. H. Cook, J. Donatowicz, N. Kains, S. R. Kane, R. Martin, K. R. Pollard, K. C. Sahu, Y. Tsapras, J. Wambsganss, D. L. Depoy, B. S.

Gaudi, C. Han, C.-U. Lee, B.-G. Park, M. Kubiak, M. K. Szymański, G. Pietrzyński, I. Soszyński, O. Szewczyk, K. Ulaczyk, F. Abe, A. Fukui, K. Furusawa, A. C. Gilmore, J. B. Hearnshaw, Y. Itow, K. Kamiya, P. M. Kilmartin, A. V. Korpela, W. Lin, C. H. Ling, K. Masuda, Y. Matsubara, N. Miyake, Y. Muraki, M. Nagaya, K. Ohnishi, T. Okumura, Y. Perrott, N. J. Rattenbury, T. Saito, T. Sako, S. Sato, L. Skuljan, D. Sullivan, W. Sweatman, P. J. Tristram, A. Allan, M. F. Bode, M. J. Burgdorf, N. Clay, S. N. Fraser, E. Hawkins, E. Kerins, T. A. Lister, C. J. Mottram, E. S. Saunders, C. Snodgrass, I. A. Steele, T. Anguita, V. Bozza, K. Harpsøe, T. C. Hinse, M. Hundertmark, P. Kjærgaard, C. Liebig, L. Mancini, G. Masi, S. Rahvar, D. Ricci, G. Scarpetta, J. Southworth, J. Surdej, C. C. Thöne, A. Riffeser, and S. Seitz. OGLE 2008-BLG-290: an accurate measurement of the limb darkening of a galactic bulge K Giant spatially resolved by microlensing. A&A, 518:A51+, July 2010. doi: 10.1051/0004-6361/201014053. (Cited on pages 127 and 154.)

A. Gould, S. Dong, B. S. Gaudi, A. Udalski, I. A. Bond, J. Greenhill, R. A. Street, M. Dominik, T. Sumi, M. K. Szymański, C. Han, W. Allen, G. Bolt, M. Bos, G. W. Christie, D. L. DePoy, J. Drummond, J. D. Eastman, A. Gal-Yam, D. Higgins, J. Janczak, S. Kaspi, S. Kozłowski, C.-U. Lee, F. Mallia, A. Maury, D. Maoz, J. McCormick, L. A. G. Monard, D. Moorhouse, N. Morgan, T. Natusch, E. O. Ofek, B.-G. Park, R. W. Pogge, D. Polishook, R. Santallo, A. Shporer, O. Spector, G. Thornley, J. C. Yee, μFUN Collaboration, M. Kubiak, G. Pietrzyński, I. Soszyński, O. Szewczyk, Ł. Wyrzykowski, K. Ulaczyk, R. Poleski, OGLE Collaboration, F. Abe, D. P. Bennett, C. S. Botzler, D. Douchin, M. Freeman, A. Fukui, K. Furusawa, J. B. Hearnshaw, S. Hosaka, Y. Itow, K. Kamiya, P. M. Kilmartin, A. Korpela, W. Lin, C. H. Ling, S. Makita, K. Masuda, Y. Matsubara, N. Miyake, Y. Muraki, M. Nagaya, K. Nishimoto, K. Ohnishi, T. Okumura, Y. C. Perrott, L. Philpott, N. Rattenbury, T. Saito, T. Sako, D. J. Sullivan, W. L. Sweatman, P. J. Tristram, E. von Seggern, P. C. M. Yock, MOA Collaboration, M. Albrow, V. Batista, J. P. Beaulieu, S. Brillant, J. Caldwell, J. J. Calitz, A. Cassan, A. Cole, K. Cook, C. Coutures, S. Dieters, D. Dominis Prester, J. Donatowicz, P. Fouqué, K. Hill, M. Hoffman, F. Jablonski, S. R. Kane, N. Kains, D. Kubas, J.-B. Marquette, R. Martin, E. Martioli, P. Meintjes, J. Menzies, E. Pedretti, K. Pollard, K. C. Sahu, C. Vinter, J. Wambsganss, R. Watson, A. Williams, M. Zub, PLANET Collaboration, A. Allan, M. F. Bode, D. M. Bramich, M. J. Burgdorf,

N. Clay, S. Fraser, E. Hawkins, K. Horne, E. Kerins, T. A. Lister, C. Mottram, E. S. Saunders, C. Snodgrass, I. A. Steele, Y. Tsapras, RoboNet Collaboration, U. G. Jørgensen, T. Anguita, V. Bozza, S. Calchi Novati, K. Harpsøe, T. C. Hinse, M. Hundertmark, P. Kjærgaard, C. Liebig, L. Mancini, G. Masi, M. Mathiasen, S. Rahvar, D. Ricci, G. Scarpetta, J. Southworth, J. Surdej, C. C. Thöne, and MiNDSTEp Consortium. Frequency of Solar-like Systems and of Ice and Gas Giants Beyond the Snow Line from High-magnification Microlensing Events in 2005-2008. ApJ, 720:1073–1089, September 2010. doi: 10.1088/0004-637X/720/2/1073. (Cited on pages 127 and 154.)

O. Guyon. Phase-induced amplitude apodization of telescope pupils for extrasolar terrestrial planet imaging. A&A, 404:379–387, jun 2003. doi: 10.1051/0004-6361:20030457. (Cited on page 34.)

O. Guyon, R. Angel, C. Bowers, J. Burge, A. Burrows, J. Codona, T. Greene, M. Iye, J. Kasting, H. Martin, D. McCarthy, V. Meadows, M. Meyer, E. Pluzhnik, N. Sleep, A. Spears, M. Tamura, D. Tenerelli, R. Vanderbei, B. Woodgate, R. Woodruff, and N. Woolf. Direct Imaging Of Nearby Exoplanets With A Small Size Space Telescope: Telescope To Observe Planetary System (TOPS). In *American Astronomical Society Meeting Abstracts*, volume 210 of *American Astronomical Society Meeting Abstracts*, pages 33.08–+, may 2007. (Cited on page 34.)

C. Jean and J. Surdej. Extinction law classification and lens redshift estimate by means of the principal component analysis. A&A, 471:807–812, September 2007. doi: 10.1051/0004-6361:20066727. (Cited on page 103.)

C. S. Kochanek, N. D. Morgan, E. E. Falco, B. A. McLeod, J. N. Winn, J. Dembicky, and B. Ketzeback. The Time Delays of Gravitational Lens HE 0435-1223: An Early-Type Galaxy with a Rising Rotation Curve. ApJ, 640:47–61, March 2006. doi: 10.1086/499766. (Cited on pages 74, 84, 85, 86, 87, and 88.)

E. Koptelova, V. L. Oknyanskij, B. P. Artamonov, and O. Burkhonov. Intrinsic quasar variability and time delay determination in the lensed quasar UM673. MNRAS, pages 1853–+, December 2009. doi: 10.1111/j.1365-2966.2009.15872.x. (Cited on page 76.)

E. Koptelova, V. Oknyanskij, B. Artamonov, and W.-P. Chen. Multiwavelengths observations of lensed quasars: interband time

delays. Mem. Soc. Astron. Italiana, 81:138–+, 2010a. (Cited on page 92.)

E. Koptelova, V. L. Oknyanskij, B. P. Artamonov, and O. Burkhonov. Intrinsic quasar variability and time delay determination in the lensed quasar UM673. MNRAS, 401:2805–2815, February 2010b. doi: 10.1111/j.1365-2966.2009.15872.x. (Cited on pages 92, 97, 101, 102, 104, 105, and 106.)

E. A. Koptelova, V. L. Oknyanskij, and E. V. Shimanovskaya. Determining time delay in the gravitationally lensed system QSO2237+0305. A&A, 452:37–46, June 2006. doi: 10.1051/0004-6361:20054050. (Cited on page 75.)

E. A. Koptelova, B. P. Artamonov, V. V. Bruevich, O. A. Burkhonov, and A. V. Sergeev. Variability of the gravitational lens UM 673 in 2003 2005. *Astronomy Reports*, 52:270–277, April 2008. doi: 10.1134/S1063772908040021. (Cited on pages 92 and 102.)

J. H. Krolik and M. C. Begelman. Molecular tori in Seyfert galaxies - Feeding the monster and hiding it. ApJ, 329:702–711, June 1988. doi: 10.1086/166414. (Cited on page 2.)

A. Labeyrie. Resolved imaging of extra-solar planets with future 10-100km optical interferometric arrays. A&AS, 118:517–524, sep 1996. (Cited on page 59.)

A. Labeyrie. Removal of coronagraphy residues with an adaptive hologram for imaging exo-Earths. In C. Aime and R. Soummer, editors, *EAS Publications Series*, volume 12 of *EAS Publications Series*, pages 3–10, 2004. doi: 10.1051/eas:2004019. (Cited on pages 33, 35, and 55.)

A. Labeyrie and H. Le Coroller. Extrasolar planet imaging. In W. A. Traub, editor, *New Frontiers in Stellar Interferometry, Proceedings of SPIE Volume 5491. Edited by Wesley A. Traub. Bellingham, WA: The International Society for Optical Engineering, 2004., p.90*, volume 5491 of *Presented at the Society of Photo-Optical Instrumentation Engineers (SPIE) Conference*, pages 90–+, oct 2004. (Cited on page 40.)

H. Le Coroller, J. Dejonghe, C. Arpesella, D. Vernet, and A. Labeyrie. Tests with a Carlina-type hypertelescope prototype. I. Demonstration of star tracking and fringe acquisition with a balloon-suspended focal camera. A&A, 426:721–728, nov 2004. doi: 10.1051/0004-6361:20041088. (Cited on page 59.)

H. Le Coroller, J. Dejonghe, X. Regal, R. Sottile, D. Mourard, D. Ricci, O. Lardiere, A. Le Vansuu, M. Boer, M. De Becker, J-M. Clausse, C. Guillaume, and J.P. Meunier. Tests with a Carlina-type Diluted Telescope Primary coherencing. A&A *(Accepted)*, December 2011. (Cited on page 155.)

J. Lehár, E. E. Falco, C. S. Kochanek, B. A. McLeod, J. A. Muñoz, C. D. Impey, H.-W. Rix, C. R. Keeton, and C. Y. Peng. Hubble Space Telescope Observations of 10 Two-Image Gravitational Lenses. ApJ, 536:584–605, June 2000. doi: 10.1086/308963. (Cited on page 91.)

J. Lehár, E. E. Falco, C. S. Kochanek, B. A. McLeod, J. A. Muñoz, C. D. Impey, H.-W. Rix, C. R. Keeton, and D. C. Y. Peng. Erratum: "Hubble Space Telescope Observations of 10 Two-Image Gravitational Lenses" (<A href="/abs/2002ApJ...536..584L">ApJ, 536, 584 [2002]</A>). ApJ, 571:1021–1021, June 2002. doi: 10.1086/340071. (Cited on page 92.)

B. Lyot. The study of the solar corona and prominences without eclipses (George Darwin Lecture, 1939). MNRAS, 99:580–+, jun 1939. (Cited on pages 5, 33, and 34.)

P. Magain, F. Courbin, M. Gillon, S. Sohy, G. Letawe, V. Chantry, and Y. Letawe. A deconvolution-based algorithm for crowded field photometry with unknown point spread function. A&A, 461:373–379, January 2007. doi: 10.1051/0004-6361:20042505. (Cited on page 92.)

A. R. Martel, H. C. Ford, H. D. Tran, G. D. Illingworth, J. E. Krist, R. L. White, W. B. Sparks, C. Gronwall, N. J. G. Cross, G. F. Hartig, M. Clampin, D. R. Ardila, F. Bartko, N. Benítez, J. P. Blakeslee, R. J. Bouwens, T. J. Broadhurst, R. A. Brown, C. J. Burrows, E. S. Cheng, P. D. Feldman, M. Franx, D. A. Golimowski, L. Infante, R. A. Kimble, M. P. Lesser, W. J. McCann, F. Menanteau, G. R. Meurer, G. K. Miley, M. Postman, P. Rosati, M. Sirianni, Z. I. Tsvetanov, and W. Zheng. Coronagraphic Imaging of 3C 273 with the Advanced Camera for Surveys. AJ, 125:2964–2974, June 2003. doi: 10.1086/375205. (Cited on page 6.)

D. Mawet, P. Riaud, C. Hanot, D. Vandormael, J. Loicq, J. Baudrand, J. Surdej, and S. Habraken. The annular groove phase mask coronagraph: an achromatic optical vortex. In *SPIE , Proc. SPIE 6693, id. #66931M (2007)*, volume 6693 of *Presented at the Society of Photo-Optical Instrumentation Engineers (SPIE) Conference*, pages 52–+, sep 2007. (Cited on page 34.)

E. Mediavilla, J. A. Muñoz, E. Falco, V. Motta, E. Guerras, H. Canovas, C. Jean, A. Oscoz, and A. M. Mosquera. Microlensing-based Estimate of the Mass Fraction in Compact Objects in Lens Galaxies. ApJ, 706:1451–1462, December 2009. doi: 10.1088/0004-637X/706/2/1451. (Cited on page 74.)

N. Miyake, T. Sumi, S. Dong, R. Street, L. Mancini, A. Gould, D. P. Bennett, Y. Tsapras, J. C. Yee, M. D. Albrow, I. A. Bond, P. Fouqué, P. Browne, C. Han, C. Snodgrass, F. Finet, K. Furusawa, K. Harpsøe, W. Allen, M. Hundertmark, M. Freeman, D. Suzuki, F. Abe, C. S. Botzler, D. Douchin, A. Fukui, F. Hayashi, J. B. Hearnshaw, S. Hosaka, Y. Itow, K. Kamiya, P. M. Kilmartin, A. Korpela, W. Lin, C. H. Ling, S. Makita, K. Masuda, Y. Matsubara, Y. Muraki, T. Nagayama, K. Nishimoto, K. Ohnishi, Y. C. Perrott, N. Rattenbury, T. Saito, L. Skuljan, D. J. Sullivan, W. L. Sweatman, P. J. Tristram, K. Wada, P. C. M. Yock, MOA Collaboration, G. Bolt, M. Bos, G. W. Christie, D. L. DePoy, J. Drummond, A. Gal-Yam, B. S. Gaudi, E. Gorbikov, D. Higgins, K.-H. Hwang, J. Janczak, S. Kaspi, C.-U. Lee, J.-R. Koo, S. Kozłowski, Y. Lee, F. Mallia, A. Maury, D. Maoz, J. McCormick, L. A. G. Monard, D. Moorhouse, J. A. Muñoz, T. Natusch, E. O. Ofek, R. W. Pogge, D. Polishook, R. Santallo, A. Shporer, O. Spector, G. Thornley, µFUN Collaboration, A. Allan, D. M. Bramich, K. Horne, N. Kains, I. Steele, RoboNet Collaboration, V. Bozza, M. J. Burgdorf, S. Calchi Novati, M. Dominik, S. Dreizler, M. Glitrup, F. V. Hessman, T. C. Hinse, U. G. Jørgensen, C. Liebig, G. Maier, M. Mathiasen, S. Rahvar, D. Ricci, G. Scarpetta, J. Skottfelt, J. Southworth, J. Surdej, J. Wambsganss, F. Zimmer, MiNDSTEp Consortium, V. Batista, J. P. Beaulieu, S. Brillant, A. Cassan, A. Cole, E. Corrales, C. Coutures, S. Dieters, J. Greenhill, D. Kubas, J. Menzies, and PLANET Collaboration. A Sub-Saturn Mass Planet, MOA-2009-BLG-319Lb. ApJ, 728:120–+, February 2011. doi: 10.1088/0004-637X/728/2/120. (Cited on pages 127 and 154.)

N. D. Morgan, C. S. Kochanek, O. Pevunova, and P. L. Schechter. The Lens Redshift and Galaxy Environment for HE 0435-1223. AJ, 129:2531–2541, June 2005. doi: 10.1086/430145. (Cited on pages 73, 74, 76, and 89.)

S. L. Morris, R. J. Weymann, A. Dressler, P. J. McCarthy, B. A. Smith, R. J. Terrile, R. Giovanelli, and M. Irwin. The Environment of Lyman- alpha Absorbers in the Sight Line toward 3C 273. ApJ, 419:524–+, December 1993. doi: 10.1086/173505. (Cited on page 5.)

A. M. Mosquera, J. A. Muñoz, and E. Mediavilla. Detection of Chromatic Microlensing in Q 2237 + 0305 A. ApJ, 691:1292–1299, February 2009. doi: 10.1088/0004-637X/691/2/1292. (Cited on page 75.)

A. M. Mosquera, J. A. Muñoz, E. Mediavilla, and C. S. Kochanek. Study of Gravitational Lens Chromaticity from Ground-based Narrow Band Photometry. *ArXiv e-prints*, August 2010. (Cited on page 74.)

J. A. Muñoz, E. E. Falco, C. S. Kochanek, J. Lehár, B. A. McLeod, C. D. Impey, H.-W. Rix, and C. Y. Peng. The Castles Project. Ap&SS, 263:51–54, June 1998. doi: 10.1023/A:1002120921330. (Cited on pages 91 and 97.)

Y. Muraki, C. Han, D. P. Bennett, D. Suzuki, L. A. G. Monard, R. Street, U. G. Jorgensen, P. Kundurthy, J. Skowron, A. C. Becker, M. D. Albrow, P. Fouqué, D. Heyrovský, R. K. Barry, J.-P. Beaulieu, D. D. Wellnitz, I. A. Bond, T. Sumi, S. Dong, B. S. Gaudi, D. M. Bramich, M. Dominik, F. Abe, C. S. Botzler, M. Freeman, A. Fukui, K. Furusawa, F. Hayashi, J. B. Hearnshaw, S. Hosaka, Y. Itow, K. Kamiya, A. V. Korpela, P. M. Kilmartin, W. Lin, C. H. Ling, S. Makita, K. Masuda, Y. Matsubara, N. Miyake, K. Nishimoto, K. Ohnishi, Y. C. Perrott, N. J. Rattenbury, T. Saito, L. Skuljan, D. J. Sullivan, W. L. Sweatman, P. J. Tristram, K. Wada, P. C. M. Yock, (The MOA Collaboration, G. W. Christie, D. L. DePoy, E. Gorbikov, A. Gould, S. Kaspi, C.-U. Lee, F. Mallia, D. Maoz, J. McCormick, D. Moorhouse, T. Natusch, B.-G. Park, R. W. Pogge, D. Polishook, A. Shporer, G. Thornley, J. C. Yee, (The μFUN Collaboration, A. Allan, P. Browne, K. Horne, N. Kains, C. Snodgrass, I. Steele, Y. Tsapras, (The RoboNet Collaboration, V. Batista, C. S. Bennett, S. Brillant, J. A. R. Caldwell, A. Cassan, A. Cole, R. Corrales, C. Coutures, S. Dieters, D. Dominis Prester, J. Donatowicz, J. Greenhill, D. Kubas, J.-B. Marquette, R. Martin, J. Menzies, K. C. Sahu, I. Waldman, A. Williams, M. Zub, (The PLANET Collaboration, H. Bourhrous, Y. Matsuoka, T. Nagayama, N. Oi, Z. Randriamanakoto, (. Observers, V. Bozza, M. J. Burgdorf, S. Calchi Novati, S. Dreizler, F. Finet, M. Glitrup, K. Harpsøe, T. C. Hinse, M. Hundertmark, C. Liebig, G. Maier, L. Mancini, M. Mathiasen, S. Rahvar, D. Ricci, G. Scarpetta, J. Skottfelt, J. Surdej, J. Southworth, J. Wambsganss, F. Zimmer, (. MiNDSTEp Consortium, A. Udalski, R. Poleski, Ł. Wyrzykowski, K. Ulaczyk, M. K. Szymański, M. Kubiak, G. Pietrzyński, I. Soszyński, and (The OGLE Collaboration. Discovery and Mass Measurements

of a Cold, 10 Earth Mass Planet and Its Host Star. ApJ, 741:22–+, November 2011. doi: 10.1088/0004-637X/741/1/22. (Cited on pages 127 and 154.)

T. Nakos, E. O. Ofek, P. Boumis, J. Cuypers, D. Sinachopoulos, E. van Dessel, A. Gal-Yam, and J. Papamastorakis. A catalog of secondary photometric standard stars around gravitational lenses. A&A, 402:1157–1158, May 2003. doi: 10.1051/0004-6361:20030310. (Cited on pages 96 and 97.)

T. Nakos, F. Courbin, J. Poels, C. Libbrecht, P. Magain, J. Surdej, J. Manfroid, I. Burud, J. Hjorth, L. Germany, C. Lidman, G. Meylan, E. Pompei, J. Pritchard, and I. Saviane. Photometric monitoring of the doubly imaged quasar UM 673: possible evidence for chromatic microlensing. A&A, 441:443–450, October 2005. doi: 10.1051/0004-6361:20052877. (Cited on pages 71, 76, 91, 92, 96, 104, 105, and 106.)

J. P. Perez. *Optique: fondements et applications*. Dunod Masson Sciences, 2000. ISBN 2100048902. (Cited on page 40.)

Andrew Carleton Phillips. *Star Formation in Barred Spiral Galaxies*. PhD thesis, University of Washington, 1993. (Cited on page 71.)

S. Poindexter and C. S. Kochanek. The Transverse Peculiar Velocity of the Q2237+0305 Lens Galaxy and the Mean Mass of Its Stars. ApJ, 712:658–667, March 2010a. doi: 10.1088/0004-637X/712/1/658. (Cited on page 76.)

S. Poindexter and C. S. Kochanek. Microlensing Evidence that a Type 1 Quasar is Viewed Face-On. ApJ, 712:668–673, March 2010b. doi: 10.1088/0004-637X/712/1/668. (Cited on page 76.)

William Press, Saul Teukolsky, William Vetterling, and Brian Flannery. *Numerical Recipes in C*. Cambridge University Press, Cambridge, UK, 2nd edition, 1992. (Cited on pages 57 and 69.)

N. Putnam, J. L. Codona, and J. R. P. Angel. Laboratory demonstration of a focal plane coronagraphic interferometer designed for anti-halo apodization of starlight. In *Society of Photo-Optical Instrumentation Engineers (SPIE) Conference Series*, volume 6272 of *Society of Photo-Optical Instrumentation Engineers (SPIE) Conference Series*, jul 2006. doi: 10.1117/12.672723. (Cited on pages 35 and 60.)

S. Refsdal and J. Surdej. Gravitational lenses. *Reports of Progress in Physics*, 57:117–185, 1994. (Cited on pages 11, 12, 23, and 121.)

J. Renn, T. Sauer, and J. Stachel. The origin of gravitational lensing: a postscript to Einstein's 1936 Science paper. *Science*, 275: 184–186, jan 1997. (Cited on pages 4, 10, and 11.)

P. Riaud, A. Boccaletti, D. Rouan, F. Lemarquis, and A. Labeyrie. The Four-Quadrant Phase-Mask Coronagraph. II. Simulations. PASP, 113:1145–1154, sep 2001. (Cited on page 34.)

P. Riaud, A. Boccaletti, J. Baudrand, and D. Rouan. The Four-Quadrant Phase Mask Coronagraph. III. Laboratory Performance. PASP, 115:712–719, jun 2003. (Cited on page 34.)

D. Ricci. Microlensing in binary systems. In *Manchester Microlensing Conference*, 2008. (Cited on page 153.)

D. Ricci, A. Riccardi, and D. Zanotti. Calibration of force actuators on an adaptive secondary prototype. Appl. Opt., 47:3631–+, July 2008. doi: 10.1364/AO.47.003631. (Cited on page 153.)

D. Ricci, H. Le Coroller, and A. Labeyrie. Extreme coronagraphy with an adaptive hologram. Simulations of exo-planet imaging. A&A, 503:301–308, August 2009. doi: 10.1051/0004-6361/200811529. (Cited on pages 33, 36, 40, 45, 48, and 153.)

D. Ricci, H. Le Coroller, A. Labeyrie, and P. Piron. Simulations of coronagraphy with a dynamic hologram for the direct detection of exo-planets. In *Society of Photo-Optical Instrumentation Engineers (SPIE) Conference Series*, volume 7731 of *Society of Photo-Optical Instrumentation Engineers (SPIE) Conference Series*, July 2010a. doi: 10.1117/12.861756. (Cited on pages 36, 45, and 153.)

D. Ricci, H. Le Coroller, and P. Piron. Coronography with a dynamic hologram. In *Proceedings of the conference In the Spirit of Lyot 2010: Direct Detection of Exoplanets and Circumstellar Disks. October 25 - 29, 2010. University of Paris Diderot, Paris, France. Edited by Anthony Boccaletti.*, October 2010b. (Cited on pages 45 and 153.)

D. Ricci, A. Elyiv, F. Finet, T. Anguita, V. Bozza, P. Browne, M. Burgdorf, S. Calchi Novati, M. Dominik, S. Dreizler, M. Glitrup, F. Grundahl, K. Harpsøe, F. Hessman, T. C. Hinse, A. Hornstrup, M. Hundertmark, U. G. Jørgensen, C. Liebig, G. Maier, L. Mancini, G. Masi, M. Mathiasen, S. Rahvar,

G. Scarpetta, J. Skottfelt, C. Snodgrass, J. Southworth, J. Teuber, C. C. Thöne, J. Wambsganß, F. Zimmer, M. Zub, and J. Surdej. Flux and color variations of the doubly imaged quasar UM673. A&A *(Submitted)*, December 2011a. (Cited on pages 91 and 153.)

D. Ricci, J. Poels, A. Elyiv, F. Finet, P. G. Sprimont, T. Anguita, V. Bozza, P. Browne, M. Burgdorf, S. Calchi Novati, M. Dominik, S. Dreizler, M. Glitrup, F. Grundahl, K. Harps, F. Hessman, T. C. Hinse, A. Hornstrup, M. Hundertmark, U. G. Jorgensen, C. Liebig, G. Maier, L. Mancini, G. Masi, M. Mathiasen, S. Rahvar, G. Scarpetta, J. Skottfelt, C. Snodgrass, J. Southworth, J. Teuber, C. C. Thone, J. Wambsganss, F. Zimmer, M. Zub, and J. Surdej. HE 0435-1223 lensed QSO VRi light curves (Ricci+, 2011). *VizieR Online Data Catalog*, 352: 89042–+, January 2011b. (Cited on page 73.)

D. Ricci, J. Poels, A. Elyiv, F. Finet, P. G. Sprimont, T. Anguita, V. Bozza, P. Browne, M. Burgdorf, S. Calchi Novati, M. Dominik, S. Dreizler, M. Glitrup, F. Grundahl, K. Harpsøe, F. Hessman, T. C. Hinse, A. Hornstrup, M. Hundertmark, U. G. Jørgensen, C. Liebig, G. Maier, L. Mancini, G. Masi, M. Mathiasen, S. Rahvar, G. Scarpetta, J. Skottfelt, C. Snodgrass, J. Southworth, J. Teuber, C. C. Thöne, J. Wambsganß, F. Zimmer, M. Zub, and J. Surdej. Flux and color variations of the quadruply imaged quasar HE 0435-1223. A&A, 528: A42+, April 2011c. doi: 10.1051/0004-6361/201016188. (Cited on pages 73, 95, 97, 101, and 153.)

F. Roddier. The effects of atmospheric turbulence in optical astronomy. *Progress in optics. Volume 19. Amsterdam, North-Holland Publishing Co., 1981, p. 281-376.*, 19:281–376, 1981. doi: 10.1016/S0079-6638(08)70204-X. (Cited on page 34.)

F. Roddier and C. Roddier. Stellar Coronograph with Phase Mask. PASP, 109:815–820, jul 1997. (Cited on page 34.)

Y.-H. Ryu, C. Han, K.-H. Hwang, R. Street, A. Udalski, T. Sumi, A. Fukui, J.-P. Beaulieu, A. Gould, M. Dominik, F. Abe, D. P. Bennett, I. A. Bond, C. S. Botzler, K. Furusawa, F. Hayashi, J. B. Hearnshaw, S. Hosaka, Y. Itow, K. Kamiya, P. M. Kilmartin, A. Korpela, W. Lin, C. H. Ling, S. Makita, K. Masuda, Y. Matsubara, N. Miyake, Y. Muraki, K. Nishimoto, K. Ohnishi, Y. C. Perrott, N. Rattenbury, T. Saito, L. Skuljan, D. J. Sullivan, D. Suzuki, W. L. Sweatman, P. J. Tristram, K. Wada, P. C. M. Yock, The MOA Collaboration, M. K. Szymański, M. Kubiak, G. Pietrzyński, R. Poleski, I. Soszyński,

O. Szewczyk, Ł. Wyrzykowski, K. Ulaczyk, The OGLE Collaboration, M. Bos, G. W. Christie, D. L. Depoy, A. Gal-Yam, B. S. Gaudi, S. Kaspi, C.-U. Lee, D. Maoz, J. McCormick, B. Monard, D. Moorhouse, R. W. Pogge, D. Polishook, Y. Shvartzvald, A. Shporer, G. Thornley, J. C. Yee, The μFUN Collaboration, M. D. Albrow, V. Batista, S. Brillant, A. Cassan, A. Cole, E. Corrales, C. Coutures, S. Dieters, P. Fouqué, J. Greenhill, J. Menzies, The PLANET Collaboration, A. Allan, D. M. Bramich, P. Browne, K. Horne, N. Kains, C. Snodgrass, I. Steele, Y. Tsapras, The RoboNet Collaboration, V. Bozza, M. J. Burgdorf, S. Calchi Novati, S. Dreizler, F. Finet, M. Glitrup, F. Grundahl, K. Harpsøe, F. V. Hessman, T. C. Hinse, M. Hundertmark, U. G. Jørgensen, C. Liebig, G. Maier, L. Mancini, M. Mathiasen, S. Rahvar, D. Ricci, G. Scarpetta, J. Skottfelt, J. Surdej, J. Southworth, J. Wambsganss, F. Zimmer, and The MiNDSTEp Collaboration. OGLE-2009-BLG-092/MOA-2009-BLG-137: A Dramatic Repeating Event with the Second Perturbation Predicted by Real-time Analysis. ApJ, 723:81–88, November 2010. doi: 10.1088/0004-637X/723/1/81. (Cited on pages 127 and 154.)

T. Schramm and R. Kayser. A simple imaging procedure for gravitational lenses. A&A, 174:361–364, March 1987. (Cited on page 5.)

I. . Shin, J. . Choi, S. . Park, C. Han, W. Allen, M. Bos, G. W. Christie, D. L. Depoy, S. Dong, J. Drummond, A. Gal-Yam, B. S. Gaudi, A. Gould, L. . Hung, J. Janczak, S. Kaspi, C. . Lee, F. Mallia, D. Maoz, A. Maury, J. McCormick, L. A. G. Monard, D. Moorhouse, J. A. Munoz, T. Natusch, C. Nelson, B. . Park, R. W. Pogge, D. Polishook, Y. Shvartzvald, A. Shporer, G. Thornley, J. C. Yee, F. Abe, D. P. Bennett, I. A. Bond, C. S. Botzler, A. Fukui, K. Furusawa, F. Hayashi, J. B. Hearnshaw, S. Hosaka, Y. Itow, K. Kamiya, P. M. Kilmartin, S. Kobara, A. Korpela, W. Lin, C. H. Ling, S. Makita, K. Masuda, Y. Matsubara, N. Miyake, Y. Muraki, M. Nagaya, K. Nishimoto, K. Ohnishi, T. Okumura, K. Omori, Y. C. Perrott, N. Rattenbury, T. Saito, L. Skuljan, D. J. Sullivan, T. Sumi, D. Suzuki, W. L. Sweatman, P. J. Tristram, K. Wada, P. C. M. Yock, M. K. Szymanski, M. Kubiak, G. Pietrzynski, I. Soszynski, O. Szewczyk, A. Udalski, K. Ulaczyk, L. Wyrzykowski, M. D. Albrow, V. Batista, J. . Beaulieu, S. Brillant, A. Cassan, A. Cole, E. Corrales, C. Coutures, S. Dieters, D. Dominis Prester, J. Donatowicz, P. Fouque, J. Greenhill, S. R. Kane, J. Menzies, K. C. Sahu, J. Wambsganss, A. Williams, M. Zub, A. Allan, D. M. Bramich, P. Browne, M. Dominik, K. Horne, N. Kains, C. Snod-

grass, I. Steele, R. Street, Y. Tsapras, V. Bozza, M. J. Burgdorf, S. Calchi Novati, S. Dreizler, F. Finet, M. Glitrup, F. Grundahl, K. Harpsoe, T. C. Hinse, M. Hundertmark, U. G. Jorgensen, C. Liebig, G. Maier, L. Mancini, M. Mathiasen, S. Rahvar, D. Ricci, G. Scarpetta, J. Skottfelt, J. Surdej, J. Southworth, and F. Zimmer. Microlensing Binaries Discovered through High-Magnification Channel. *ArXiv e-prints*, September 2011. (Cited on pages 127 and 154.)

A. Shishido and T. Ikeda. High-performance rewritable Bragg hologram with high multiplicities. In *Society of Photo-Optical Instrumentation Engineers (SPIE) Conference Series*, volume 6587 of *Society of Photo-Optical Instrumentation Engineers (SPIE) Conference Series*, may 2007. doi: 10.1117/12.722666. (Cited on page 59.)

D. Sinachopoulos, T. Nakos, P. Boumis, E. van Dessel, M. Burger, and P. Rodríguez-Gil. Photometric Variability of the Gravitational Lens 0142-100 (UM 673). AJ, 122:1692–1696, October 2001. doi: 10.1086/323306. (Cited on pages 92 and 96.)

D. Sluse, J. Surdej, J.-F. Claeskens, D. Hutsemékers, C. Jean, F. Courbin, T. Nakos, M. Billeres, and S. V. Khmil. A quadruply imaged quasar with an optical Einstein ring candidate: 1RXS J113155.4-123155. A&A, 406:L43–L46, July 2003. doi: 10.1051/0004-6361:20030904. (Cited on pages 107 and 109.)

D. Sluse, J.-F. Claeskens, B. Altieri, R. A. Cabanac, O. Garcet, D. Hutsemékers, C. Jean, A. Smette, and J. Surdej. Multi-wavelength study of the gravitational lens system RXS J113155.4-123155. I. Multi-epoch optical and near infrared imaging. A&A, 449:539–550, April 2006. doi: 10.1051/0004-6361:20053148. (Cited on pages 107 and 109.)

D. Sluse, J.-F. Claeskens, D. Hutsemékers, and J. Surdej. Multi-wavelength study of the gravitational lens system RXS J1131-1231. III. Long slit spectroscopy: micro-lensing probes the QSO structure. A&A, 468:885–901, June 2007. doi: 10.1051/0004-6361:20066821. (Cited on page 108.)

A. Smette, J. Surdej, P. A. Shaver, C. B. Foltz, F. H. Chaffee, Jr., and P. Magain. Preliminary analysis of high-resolution spectra for UM 673 A & B. In Y. Mellier, B. Fort, & G. Soucail, editor, *Gravitational Lensing*, volume 360 of *Lecture Notes in Physics, Berlin Springer Verlag*, pages 122–+, 1990. doi: 10.1007/BFb0009226. (Cited on page 91.)

A. Smette, J. Surdej, P. A. Shaver, C. B. Foltz, F. H. Chaffee, R. J. Weymann, R. E. Williams, and P. Magain. A spectroscopic study of UM 673 A and B - On the size of Lyman-alpha clouds. ApJ, 389:39–62, April 1992. doi: 10.1086/171187. (Cited on page 91.)

Anton Norup Sørensen. Evaluation of the MAT/EEV 44-82 ser. no. 8171-1-1 "Ringo". Technical report, IJAF, Copenhagen University Observatory, September 2000. (Cited on page 68.)

R. Soummer, C. Aime, and P. E. Falloon. Stellar coronagraphy with prolate apodized circular apertures. A&A, 397:1161–1172, jan 2003. doi: 10.1051/0004-6361:20021573. (Cited on page 34.)

R. Soummer, L. Pueyo, A. Sivaramakrishnan, and R. J. Vanderbei. Fast computation of Lyot-style coronagraph propagation. *Optics Express*, 15:15935–+, 2007. doi: 10.1364/OE.15.015935. (Cited on page 48.)

J. Southworth, T. C. Hinse, M. J. Burgdorf, M. Dominik, A. Hornstrup, U. G. Jørgensen, C. Liebig, D. Ricci, C. C. Thöne, T. Anguita, V. Bozza, S. C. Novati, K. Harpsøe, L. Mancini, G. Masi, M. Mathiasen, S. Rahvar, G. Scarpetta, C. Snodgrass, J. Surdej, and M. Zub. High-precision photometry by telescope defocussing - II. The transiting planetary system WASP-4. MNRAS, 399:287–294, October 2009a. doi: 10.1111/j.1365-2966.2009.15283.x. (Cited on pages 129 and 155.)

J. Southworth, T. C. Hinse, M. J. Burgdorf, M. Dominik, A. Hornstrup, U. G. Jorgensen, C. Liebig, D. Ricci, C. C. Thone, T. Anguita, V. Bozza, S. C. Novati, K. Harpsoe, L. Mancini, G. Masi, M. Mathiasen, S. Rahvar, G. Scarpetta, C. Snodgrass, J. Surdej, and M. Zub. Transiting planetary system WASP-4 (Southworth+, 2009). *VizieR Online Data Catalog*, 739:90287–+, October 2009b. (Cited on page 129.)

J. Southworth, T. C. Hinse, M. Dominik, M. Glitrup, U. G. Jørgensen, C. Liebig, M. Mathiasen, D. R. Anderson, V. Bozza, P. Browne, M. Burgdorf, S. Calchi Novati, S. Dreizler, F. Finet, K. Harpsøe, F. Hessman, M. Hundertmark, G. Maier, L. Mancini, P. F. L. Maxted, S. Rahvar, D. Ricci, G. Scarpetta, J. Skottfelt, C. Snodgrass, J. Surdej, and F. Zimmer. Physical Properties of the 0.94-Day Period Transiting Planetary System WASP-18. ApJ, 707:167–172, December 2009c. doi: 10.1088/0004-637X/707/1/167. (Cited on pages 130 and 155.)

J. Southworth, T. C. Hinse, U. G. Jørgensen, M. Dominik, D. Ricci, M. J. Burgdorf, A. Hornstrup, P. J. Wheatley, T. Anguita,

V. Bozza, S. C. Novati, K. Harpsøe, P. Kjærgaard, C. Liebig, L. Mancini, G. Masi, M. Mathiasen, S. Rahvar, G. Scarpetta, C. Snodgrass, J. Surdej, C. C. Thöne, and M. Zub. High-precision photometry by telescope defocusing - I. The transiting planetary system WASP-5. MNRAS, 396:1023–1031, June 2009d. doi: 10.1111/j.1365-2966.2009.14767.x. (Cited on pages 129 and 155.)

J. Southworth, T. C. Hinse, U. G. Jorgensen, M. Dominik, D. Ricci, M. J. Burgdorf, A. Hornstrup, P. J. Wheatley, T. Anguita, V. Bozza, S. C. Novati, K. Harpsoe, P. Kjaergaard, C. Liebig, L. Mancini, G. Masi, M. Mathiasen, S. Rahvar, G. Scarpetta, C. Snodgrass, J. Surdej, C. C. Thone, and M. Zub. Transiting planetary system WASP-5 (Southworth+, 2009). *VizieR Online Data Catalog*, 739:61023–+, October 2009e. (Cited on page 129.)

J. Southworth, T. C. Hinse, M. Dominik, M. Glitrup, U. G. Jørgensen, C. Liebig, M. Mathiasen, D. R. Anderson, V. Bozza, P. Browne, M. Burgdorf, S. Calchi Novati, S. Dreizler, F. Finet, K. Harpsøe, F. Hessman, M. Hundertmark, G. Maier, L. Mancini, P. F. L. Maxted, S. Rahvar, D. Ricci, G. Scarpetta, J. Skottfelt, C. Snodgrass, J. Surdej, and F. Zimmer. ERRATUM: "Physical Properties of the 0.94 Day Period Transiting Planetary System WASP-18" <A href="/abs/2009ApJ...707..167S">(2009, ApJ, 707, 167)</A>. ApJ, 723:1829–+, November 2010a. doi: 10.1088/0004-637X/723/2/1829. (Cited on page 130.)

J. Southworth, L. Mancini, S. C. Novati, M. Dominik, M. Glitrup, T. C. Hinse, U. G. Jørgensen, M. Mathiasen, D. Ricci, G. Maier, F. Zimmer, V. Bozza, P. Browne, I. Bruni, M. Burgdorf, M. Dall'Ora, F. Finet, K. Harpsøe, M. Hundertmark, C. Liebig, S. Rahvar, G. Scarpetta, J. Skottfelt, B. Smalley, C. Snodgrass, and J. Surdej. High-precision photometry by telescope defocusing - III. The transiting planetary system WASP-2. MNRAS, 408:1680–1688, November 2010b. doi: 10.1111/j.1365-2966.2010.17238.x. (Cited on pages 129 and 155.)

J. Southworth, M. Dominik, U. G. Jørgensen, S. Rahvar, C. Snodgrass, K. Alsubai, V. Bozza, P. Browne, M. Burgdorf, S. Calchi Novati, P. Dodds, S. Dreizler, F. Finet, T. Gerner, S. Hardis, K. Harpsøe, C. Hellier, T. C. Hinse, M. Hundertmark, N. Kains, E. Kerins, C. Liebig, L. Mancini, M. Mathiasen, M. T. Penny, S. Proft, D. Ricci, K. Sahu, G. Scarpetta, S. Schäfer, F. Schönebeck, and J. Surdej. A much lower density for the transiting extrasolar planet WASP-7. A&A, 527:A8+, March

2011a. doi: 10.1051/0004-6361/201016183. (Cited on pages 129 and 155.)

J. Southworth, M. Dominik, U. G. Jorgensen, S. Rahvar, C. Snodgrass, K. Alsubai, V. Bozza, P. Browne, M. Burgdorf, S. Calchi Novati, P. Dodds, S. Dreizler, F. Finet, T. Gerner, S. Hardis, K. Harpsoe, C. Hellier, T. C. Hinse, M. Hundertmark, N. Kains, E. Kerins, C. Liebig, L. Mancini, M. Mathiasen, M. T. Penny, S. Proft, D. Ricci, G. Scarpetta, S. Schaefer, F. Schoenebeck, and J. Surdej. A much lower density for the transiting extrasolar planet WASP-7. *VizieR Online Data Catalog*, 352:79008–+, 2011b. (Cited on page 129.)

J. Southworth, L. Mancini, S. Calchi Novati, M. Dominik, M. Glitrup, T. C. Hinse, U. G. Jorgensen, M. Mathiasen, D. Ricci, G. Maier, F. Zimmer, V. Bozza, P. Browne, I. Bruni, M. Burgdorf, M. Dall'Ora, F. Finet, K. Harpsoe, M. Hundertmark, C. Liebig, S. Rahvar, G. Scarpetta, J. Skottfelt, B. Smalley, C. Snodgrass, and J. Surdej. Transiting planetary system WASP-2 (Southworth+, 2010). *VizieR Online Data Catalog*, 740: 81680–+, January 2011c. (Cited on page 129.)

H. Sugai, A. Kawai, A. Shimono, T. Hattori, G. Kosugi, N. Kashikawa, K. T. Inoue, and M. Chiba. Integral Field Spectroscopy of the Quadruply Lensed Quasar 1RXS J1131-1231: New Light on Lens Substructures. ApJ, 660:1016–1022, May 2007. doi: 10.1086/513731. (Cited on page 108.)

J. Surdej, P. Magain, J.-P. Swings, U. Borgeest, T. J.-L. Courvoisier, R. Kayser, K. I. Kellermann, H. Kuhr, and S. Refsdal. A new case of gravitational lensing. Nature, 329:695–+, October 1987. doi: 10.1038/329695a0. (Cited on page 91.)

J. Surdej, P. Magain, J.-P. Swings, U. Borgeest, T. J.-L. Courvoisier, R. Kayer, K. I. Kellermann, H. Kuhr, and S. Refsdal. Observations of the new gravitational lens system UM 673 = Q 0142-100. A&A, 198:49–60, June 1988. (Cited on pages 91, 103, and 105.)

J. Surdej, J.-F. Claeskens, C. Delacroix, T. Sadibekova, P. Bartczak, P. H. I. Coleman, A. Magette, J. Poels, D. Ricci, and D. Sluse. Gravitational Lensing, Dark Matter and the Optical Gravitational Lens Experiment. In J. Cugon, J.-P. Lansberg, & N. Matagne, editor, *American Institute of Physics Conference Series*, volume 1038 of *American Institute of Physics Conference Series*, pages 173–182, August 2008. doi: 10.1063/1.2987170. (Cited on pages 10, 12, 21, and 155.)

J. Surdej, C. Delacroix, P. Coleman, M. Dominik, S. Habraken, C. Hanot, H. Le Coroller, D. Mawet, H. Quintana, T. Sadibekova, and D. Sluse. The Optimal Gravitational Lens Telescope. AJ, 139:1935–1941, May 2010. doi: 10.1088/0004-6256/139/5/1935. (Cited on pages 5, 13, 23, and 30.)

M. Tallon and I. Tallon-Bosc. The object-image relationship in Michelson stellar interferometry. A&A, 253:641–645, January 1992. (Cited on page 59.)

M. Tamura, H. Suto, Y. Itoh, N. Ebizuka, Y. Doi, K. Murakawa, S. S. Hayashi, Y. Oasa, H. Takami, and N. Kaifu. Coronagraph imager with adaptive optics (CIAO): description and first results. In M. Iye & A. F. Moorwood, editor, *Society of Photo-Optical Instrumentation Engineers (SPIE) Conference Series*, volume 4008 of *Society of Photo-Optical Instrumentation Engineers (SPIE) Conference Series*, pages 1153–1161, August 2000. (Cited on page 6.)

J. R. Trump, C. D. Impey, B. C. Kelly, F. Civano, J. M. Gabor, A. M. Diamond-Stanic, A. Merloni, C. M. Urry, H. Hao, K. Jahnke, T. Nagao, Y. Taniguchi, A. M. Koekemoer, G. Lanzuisi, C. Liu, V. Mainieri, M. Salvato, and N. Z. Scoville. Accretion Rate and the Physical Nature of Unobscured Active Galaxies. ApJ, 733:60–+, May 2011. doi: 10.1088/0004-637X/733/1/60. (Cited on page 2.)

J. A. Tyson, W. A. Baum, and T. Kreidl. Deep CCD images of 3C 273. ApJ, 257:L1–L5, June 1982. doi: 10.1086/183797. (Cited on page 5.)

D. Walsh, R. F. Carswell, and R. J. Weymann. 0957 + 561 A, B - Twin quasistellar objects or gravitational lens. *Nature*, 279:381–384, may 1979. (Cited on pages 4 and 11.)

J. Wambsganss. Part 4: Gravitational microlensing. In G. Meylan, P. Jetzer, P. North, P. Schneider, C. S. Kochanek, & J. Wambsganss, editor, *Saas-Fee Advanced Course 33: Gravitational Lensing: Strong, Weak and Micro*, pages 453–540, 2006. (Cited on page 65.)

L. Wisotzki, N. Christlieb, N. Bade, V. Beckmann, T. Köhler, C. Vanelle, and D. Reimers. The Hamburg/ESO survey for bright QSOs. III. A large flux-limited sample of QSOs. A&A, 358:77–87, June 2000. (Cited on page 73.)

L. Wisotzki, P. L. Schechter, H. V. Bradt, J. Heinmüller, and D. Reimers. HE 0435-1223: A wide separation quadruple

QSO and gravitational lens. A&A, 395:17–23, November 2002. doi: 10.1051/0004-6361:20021213. (Cited on pages 68, 73, 77, and 89.)

L. Wisotzki, T. Becker, L. Christensen, A. Helms, K. Jahnke, A. Kelz, M. M. Roth, and S. F. Sanchez. Integral-field spectrophotometry of the quadruple QSO HE 0435-1223: Evidence for microlensing. A&A, 408:455–463, September 2003. doi: 10.1051/0004-6361:20031004. (Cited on page 73.)

L. Wisotzki, T. Becker, L. Christensen, K. Jahnke, A. Helms, A. Kelz, M. M. Roth, and S. F. Sánchez. Integral field spectrophotometry of gravitationally lensed QSOs with PMAS. *Astronomische Nachrichten*, 325:135–138, February 2004. doi: 10.1002/asna.200310193. (Cited on page 92.)

F. Zwicky. Nebulae as Gravitational Lenses. *Physical Review*, 51: 290–290, feb 1937. doi: 10.1103/PhysRev.51.290. (Cited on page 11.)

Publications

This section contains a list of publications. The standard bibliographic format can be found in the Bibliography (pag. 131).

As first author

Papers in referred journals

- **D. Ricci**, H. Le Coroller, and A. Labeyrie. Extreme coronagraphy with an adaptive hologram. Simulations of exo-planet imaging. A&A, 503:301–308, August 2009. [Ricci et al., 2009]
- **D. Ricci**, J. Poels, A. Elyiv, F. Finet, P. G. Sprimont, ..., and J. Surdej. Flux and color variations of the quadruply imaged quasar HE 0435-1223. A&A, 528:A42+, April 2011c. [Ricci et al., 2011c]
- **D. Ricci**, A. Elyiv, F. Finet, O. Wertz, ..., and J. Surdej. Flux and color variations of the doubly imaged quasar UM673. A&A **(Submitted)**, December 2011a. [Ricci et al., 2011a]
- **D. Ricci**, A. Riccardi, and D. Zanotti. Calibration of force actuators on an adaptive secondary prototype. Appl. Opt., 47:3631–+, July 2008. [Ricci et al., 2008]

Proceedings and posters

- **D. Ricci**, H. Le Coroller, A. Labeyrie, and P. Piron. Simulations of coronagraphy with a dynamic hologram for the direct detection of exo-planets. In *SPIE Conference Series*, volume 7731 of *Society of Photo-Optical Instrumentation Engineers (SPIE) Conference Series*, July 2010a. [Ricci et al., 2010a]
- **D. Ricci**, H. Le Coroller, and P. Piron. Coronography with a dynamic hologram. In *Proceedings of the conference In the Spirit of Lyot 2010: Direct Detection of Exoplanets and Circumstellar Disks. October 25 - 29, 2010. University of Paris Diderot, Paris, France. Edited by Anthony Boccaletti.*, October 2010b. [Ricci et al., 2010b]
- **D. Ricci**. Microlensing in binary systems. In *Manchester Microlensing Conference*, 2008. [Ricci, 2008]

As co-author

Bulge microlenses

- N. Miyake, T. Sumi, . . . , **D. Ricci**, . . . , and PLANET Collaboration. A Sub-Saturn Mass Planet, MOA-2009-BLG-319Lb. ApJ, 728:120–+, February 2011. [Miyake et al., 2011]
- Y. Muraki, C. Han, . . . , **D. Ricci**, . . . , I. Soszyński, and (The OGLE Collaboration. Discovery and Mass Measurements of a Cold, 10 Earth Mass Planet and Its Host Star. ApJ, 741: 22–+, November 2011. [Muraki et al., 2011]
- M. Dominik, U. G. Jørgensen, . . . , **D. Ricci**, . . . , and M. Zub. Realisation of a fully-deterministic microlensing observing strategy for inferring planet populations. *Astronomische Nachrichten*, 331:671–+, July 2010. [Dominik et al., 2010b]
- P. Fouqué, D. Heyrovský, . . . , **D. Ricci**, . . . , and S. Seitz. OGLE 2008-BLG-290: an accurate measurement of the limb darkening of a galactic bulge K Giant spatially resolved by microlensing. A&A, 518:A51+, July 2010. [Fouqué et al., 2010]
- A. Gould, S. Dong, . . . , **D. Ricci**, . . . , J. Surdej, C. C. Thöne, and MiNDSTEp Consortium. Frequency of Solar-like Systems and of Ice and Gas Giants Beyond the Snow Line from High-magnification Microlensing Events in 2005-2008. ApJ, 720:1073–1089, September 2010. [Gould et al., 2010]
- Y.-H. Ryu, C. Han, . . . , **D. Ricci**, . . . , F. Zimmer, and The MiNDSTEp Collaboration. OGLE-2009-BLG-092/ MOA-2009-BLG-137: A Dramatic Repeating Event with the Second Perturbation Predicted by Real-time Analysis. ApJ, 723:81–88, November 2010. [Ryu et al., 2010]
- I. . Shin, J. . Choi, . . . , **D. Ricci**, and F. Zimmer. Microlensing Binaries Discovered through High-Magnification Channel. *ArXiv e-prints*, September 2011. [Shin et al., 2011]
- V. Batista, A. Gould, . . . , **D. Ricci**, . . . G. Scarpetta, J. Southworth, J. Surdej, F. Zimmer, The RoboNet Collaboration, A. Allan, D. M. Bramich, C. Snodgrass, I. A. Steele, and R. A. Street. MOA-2009-BLG-387Lb: a massive planet orbiting an M dwarf. A&A, 529:A102+, May 2011a. [Batista et al., 2011a]

Planetary transits

- J. Southworth, T. C. Hinse, U. G. Jørgensen, M. Dominik, **D. Ricci**, ..., and M. Zub. High-precision photometry by telescope defocusing - I. The transiting planetary system WASP-5. MNRAS, 396:1023–1031, June 2009d. [Southworth et al., 2009d]
- J. Southworth, T. C. Hinse, ..., **D. Ricci**, ...J. Surdej, and M. Zub. High-precision photometry by telescope defocussing - II. The transiting planetary system WASP-4. MNRAS, 399:287–294, October 2009a. [Southworth et al., 2009a]
- J. Southworth, L. Mancini, ..., **D. Ricci**, ...and J. Surdej. High-precision photometry by telescope defocusing - III. The transiting planetary system WASP-2. MNRAS, 408: 1680–1688, November 2010b. [Southworth et al., 2010b]
- J. Southworth, M. Dominik, ..., **D. Ricci**, ...and J. Surdej. A much lower density for the transiting extrasolar planet WASP-7. A&A, 527:A8+, March 2011a. [Southworth et al., 2011a]
- J. Southworth, T. C. Hinse, ..., **D. Ricci**, ..., and F. Zimmer. Physical Properties of the 0.94-Day Period Transiting Planetary System WASP-18. ApJ, 707:167–172, December 2009c. [Southworth et al., 2009c]
- M. L. Bryan, K. A. Alsubai, ..., **D. Ricci**, ...and J. F. Skottfelt. Qatar-2: A K dwarf orbited by a transiting hot Jupiter and a more massive companion in an outer orbit. *ArXiv e-prints*, October 2011. [Bryan et al., 2011]

Other papers and proceedings

- H. Le Coroller, J. Dejonghe, ..., **D. Ricci**, ..., and J.P. Meunier. Tests with a Carlina-type Diluted Telescope Primary coherencing. A&A **(Accepted)**, December 2011. [Le Coroller et al., 2011]
- J. Surdej, J.-F. Claeskens, ..., **D. Ricci**, and D. Sluse. Gravitational Lensing, Dark Matter and the Optical Gravitational Lens Experiment. In J. Cugon, J.-P. Lansberg, & N. Matagne, editor, volume 1038 of *American Institute of Physics Conference Series*, pages 173–182, August 2008. [Surdej et al., 2008]
- C. Adami, A. Mazure, ..., **D. Ricci**, and L. Tresse. The XMM-LSS survey: optical assessment and properties of different X-ray selected cluster classes. A&A, 526:A18+, February 2011. [Adami et al., 2011]

Acknowledgments

Once arrived at the end of this path, it is a special pleasure to thank all the people who supported me during these years spent in the lovely astrophysics department of the *Cité Ardente*.

I would like to start with my PhD supervisor, Prof. Jean Surdej, whose patience in explaining clearly and simply this matter, and his humanity in the daily life, were essential to complete these studies starting every working day with a smile. Another big thank you is for my co-supervisor Hervé Le Coroller, who opened me the doors to many domains of astronomy and astronomic instrumentation, stimulating me to understand new matters and improve my knowledges. Through him I send all my best regards to all the people I know at the Haute Provence Observatory.

Coming back in Liège, there are many colleagues that I would like to thank, as without knowing them I probably wouldn't have even read this far... so I thank François for the math, Olivier for the other math, Charles for the mac, Emilie for the other mac, Ludo for the music, Joël for the other music, Laurent for his kindness, Antho for his kitchen, and Olivier for the *whist*. I hope that Gi goes on swearing in italian when we chat, that Méla resolves hers problems with gnuplot, that Audrey organizes one more dinner with all, and that Eva does not loose her direct link with St Nicolas. A special thank goes to Christian, PG, Yassine and Yves for the programming help and the political discussions. And finally thank you to Andrii, Olga, Chloi, Brajesh, Virginie and Tanià for all the time spent together. I am grateful to Sylvia et Denise for all their help, I would have been really lost without them, flooded by the bureaucracy.

Then I wish to thank all the people I knew here in Liège, starting from the infamous Home, where this story knew its begin: Nino, César, Andrès, Yan, Paco; and then the "people of the center": Beto, Helena, Lorena, Carlo, Simona and Fer; Lorenzo, Silvia and Remy. Thank you to all my friends in Italy: Scogna, Demma, Paul, Memme and Chiara; Flavia and Stè; and those spread around the world: Emi, Katie, Gigi, Daphnee and Julia; and finally all the people that I have forgot to mention!

A special thanks goes to all the players of fc ardente!

Lastly, and most importantly, I wish to thank Marica, who supported me all the time, and my family, without exception, because *senza di voi non sarei mai arrivato fin qui*.

Printed in Italy on January 6, 2012 – Tipografia Raffaello Canessa
Via Villabassa 6, 16038 Santa Margherita Ligure (Genova)